




12-2020

## Processing-Structure-Performance Relationships in Fused Filament Fabricated Fiber Reinforced ABS for Material Qualification

William Howard Ferrell  
*University of Tennessee, Knoxville, wferrel2@vols.utk.edu*

Follow this and additional works at: [https://trace.tennessee.edu/utk\\_graddiss](https://trace.tennessee.edu/utk_graddiss)

 Part of the [Applied Mechanics Commons](#), and the [Polymer and Organic Materials Commons](#)

---

### Recommended Citation

Ferrell, William Howard, "Processing-Structure-Performance Relationships in Fused Filament Fabricated Fiber Reinforced ABS for Material Qualification. " PhD diss., University of Tennessee, 2020.  
[https://trace.tennessee.edu/utk\\_graddiss/6070](https://trace.tennessee.edu/utk_graddiss/6070)

This Dissertation is brought to you for free and open access by the Graduate School at TRACE: Tennessee Research and Creative Exchange. It has been accepted for inclusion in Doctoral Dissertations by an authorized administrator of TRACE: Tennessee Research and Creative Exchange. For more information, please contact [trace@utk.edu](mailto:trace@utk.edu).

To the Graduate Council:

I am submitting herewith a dissertation written by William Howard Ferrell entitled "Processing-Structure-Performance Relationships in Fused Filament Fabricated Fiber Reinforced ABS for Material Qualification." I have examined the final electronic copy of this dissertation for form and content and recommend that it be accepted in partial fulfillment of the requirements for the degree of Doctor of Philosophy, with a major in Materials Science and Engineering.

Stephanie C. TerMaath, Major Professor

We have read this dissertation and recommend its acceptance:

David Keffer, Yanfei Gao, Sudarsanam Babu

Accepted for the Council:

Dixie L. Thompson

Vice Provost and Dean of the Graduate School

(Original signatures are on file with official student records.)

**Processing-Structure-Performance Relationships in Fused  
Filament Fabricated Fiber Reinforced ABS for Material  
Qualification**

**A Dissertation Presented for the  
Doctor of Philosophy  
Degree  
The University of Tennessee, Knoxville**

**William Howard Ferrell  
December 2020**

Copyright © 2020 by William Howard Ferrell  
All rights reserved.

## **DEDICATION**

I dedicate this work to 10-year-old me. You had to tell people you were going to get a PhD and now here I am cleaning up that mess.

## ACKNOWLEDGEMENTS

Thank you to everyone I have met along the way. I know this is as generic and boring of a starting thank you as it can get, but truly I am grateful for so many people. From Robyn Collette getting me to join RunKnox when we started graduate school to now, my life has taken a lot of turns that I never could have predicted. So, here is my attempt to acknowledge some people and groups.

To all of the awesome runners, triathletes, swimmers, gym go-ers, crossfitters, trail runners, cyclists, wilderness men and women, and so many more, thank you for reminding me that having a screw loose isn't a bad thing. Thank you for reminding me that just getting up and doing "the thing" is courageous and impressive and it doesn't matter if you are fast or slow. Thank you for making it normal to have shaved legs part of the year and hairy the rest. Thank you for making short shorts fashionable and slip on sandals customary brunch footwear. These little lessons carried over into grad school and helped provide the confidence needed to make my voice heard.

To all of the graduate students I have worked with, lived with, partied with, laughed with, and bemoaned grad life with, you are all awesome. Some of the smartest people I have met in my life and some of the hardest working individuals out there. Knowing you are not alone is sometimes all that is needed to make really bizarre situations not feel suffocating. Whether you are graduating soon, graduating eventually, or moving on to better times, you are all worth it and sharing intellectual space with you all has been a pleasure.

To all the people who have been a part of my life but maybe aren't as active in it now, thank you for all of the fun times, the hard times, and the lessons along the way. Whether it was just a function of a global pandemic, my tunnel vision towards certain goals, or a decided parting of ways, everything that has happened has helped push me or pull me towards this moment. So, thank you all for being who you are and for helping me on my journey through grad school.

Finally, I want to thank my research group, my advisor, and my parents specifically. I would not be who I am today with the support and the environment provided by my parents that got me to and through graduate school. I would not have the success I have without the continued support and guidance from my colleagues in the lab and from my advisor Dr. TerMaath. Thank you all so much for all of the good times, the bad times, the hard times, and just the plain old times.

The process is what makes you, and I appreciate everyone who has been a part of my process. Thank you.

## ABSTRACT

This dissertation uses the processing-structure-performance relationships to elucidate future needs in qualification of materials manufactured by fused filament fabrication and also introduces a previously unused testing method for the determination of fracture toughness in these materials.

Fused filament fabrication (FFF) is an additive manufacturing technique that utilizes the layering of deposited molten plastic in two dimensional shapes to create three dimensional objects. This technique has gained traction over the past two decades as a disruptive manufacturing technology that promises many benefits. In order for FFF to truly be a staple in manufacturing spaces across the world for the production of end-user parts, standardization of testing procedures for the qualification of FFF specific materials must take place. Adjusting standards for qualification must occur with analysis in ultimate tensile strength, response to environmental conditions, and the fracture behavior of these parts.

In Chapter 1, a comprehensive analysis of the current state of the art in fracture of FFF parts is presented and discussed. Discussed in this section are the rheological specific phenomena that govern the polymer chain physics at interfaces and within deposited beads. This is tied to the fracture strength and the current questions in part behavior. In chapter 2, a commonly used tensile testing standard is explored and tested on fiber reinforced acrylonitrile-butadiene-styrene (ABS). Due to the complex manufacturing process, new naming standards and testing recommendations are made and the influence of part production methodologies and processing parameters on ultimate tensile strength are explored. The response of fiber reinforced and non-reinforced ABS in environmental conditioning is tested and discussed in chapter 3, where specimens were exposed to heat and moisture then tested in tension. Chapter 4 introduces a unique testing specimen to the FFF literature to obtain multiple fracture modes. Through this test specimen, the nature of the material as a laminate or as a porous homogeneous material is also explored and documented.



# TABLE OF CONTENTS

|   |     |
|---|-----|
| CHAPTER I Fracture behavior of fused filament fabricated polymers: A Review .   | 1   |
| Abstract .....  | 2   |
| Introduction .....  | 2   |
| Phenomenological Complexity .....   | 6   |
| Tube Theory .....   | 8   |
| Polymer Melts in FFF conditions.....  | 14  |
| Polymer Diffusion for Bead Contacts .....   | 18  |
| Rheological Phenomena: Slip Springs and Beyond.....   | 21  |
| Fracture Mechanics and FFF .....  | 23  |
| Fracture Mechanics Concepts and Terminology.....  | 23  |
| Linear Elastic Fracture Mechanics for FFF .....   | 26  |
| Elastic-Plastic Fracture Mechanics in FFF .....   | 30  |
| Interlaminar Fracture in FFF .....  | 32  |
| Complexity of fracture in FFF.....  | 37  |
| Scale up of FFF .....   | 41  |
| BAAM Fracture.....  | 46  |
| CONCLUSIONS .....   | 48  |
| REFERENCES.....   | 50  |
| CHAPTER II Uniaxial Tensile Testing Standardization for the Qualification of<br>Fiber Reinforced Plastics for Fused Filament Fabrication..... | 65  |
| Abstract .....  | 66  |
| Introduction .....  | 67  |
| Materials and Methods .....   | 70  |
| Results .....   | 72  |
| Classification.....   | 72  |
| Extrusion.....  | 87  |
| Methodologies .....   | 97  |
| Discussion .....  | 107 |
| Classification.....   | 107 |
| Extrusion.....  | 109 |
| Methodologies .....   | 111 |
| Conclusions.....  | 113 |
| References .....  | 115 |
| CHAPTER III Tensile Strength Dependence of FFF Fiber Reinforced ABS on<br>Environmental Conditioning .....                                    | 123 |
| Abstract .....  | 124 |
| Introduction .....  | 124 |
| Materials and Test Methods .....  | 127 |
| Fabrication.....  | 127 |
| Mechanical Testing.....   | 130 |
| Material Characterization .....   | 132 |
| Experimental Testing Results.....   | 133 |

|  |     |
|--|-----|
| ABS_XY.....  | 133 |
| ABS_YX.....  | 139 |
| CF-ABS_XY.....   | 145 |
| CF-ABS_YX.....   | 150 |
| Moisture Effects Test.....   | 154 |
| Discussion.....  | 156 |
| Temperature Effects.....   | 156 |
| Moisture Effects.....  | 161 |
| Conclusions.....   | 163 |
| References.....  | 164 |
| CHAPTER IV Novel Use of Semi-Circular Bend Specimen for Fracture of BAAM |     |
| Polymers.....  | 168 |
| Abstract.....  | 169 |
| Introduction.....  | 169 |
| Materials and Methods.....   | 171 |
| Materials.....   | 171 |
| Specimen Geometry.....   | 171 |
| Mechanical Testing.....  | 173 |
| Fracture Theory.....   | 174 |
| Results.....   | 177 |
| Mode I Intrabeard Fracture.....  | 177 |
| SCB Specimens from 1.5m Plaque.....                                      | 181 |
| Discussion.....  | 189 |
| Comparison of G and J.....   | 189 |
| Layer Time effect on fracture.....                                       | 190 |
| Interlayer Fracture Toughness.....                                       | 190 |
| Characterization of BAAM Parts.....                                      | 190 |
| Conclusions.....   | 192 |
| References.....  | 193 |
| Chapter V Concluding Remarks and Future Work.....                        | 195 |
| Appendix.....  | 201 |
| List of Publications.....  | 201 |
| VITA.....  | 202 |

## LIST OF TABLES

|  |     |
|--|-----|
| <b>Table 1</b> Test specimen and fracture toughness of PLA by various authors to date with standard deviation (S.D.) provided when available. Not valid shows specimens that exceeded the linear elastic range and therefore K or G do not apply. .... | 39  |
| <b>Table 2</b> Test specimen and fracture toughness of ABS and carbon fiber ABS (CF-ABS) by various authors to date with standard deviation (S.D.) provided when available. ....   | 40  |
| <b>Table 3</b> Baseline print parameters and testing ranges .....  | 71  |
| <b>Table 4</b> One way ANOVA analysis of ultimate tensile stress for the five ASTM Types.....  | 77  |
| <b>Table 5</b> T-Test of type I and type III show difference in means is not conclusively significant.....   | 78  |
| <b>Table 6</b> Statistics for cross-sectional area and ultimate strength for specimens with identical raster angles but different bed orientations. ....   | 87  |
| <b>Table 7</b> Yield stress and ultimate tensile strength for varying nozzle temperature with the standard deviation reported as a percentage of the mean. ....  | 92  |
| <b>Table 8</b> Yield stress and ultimate tensile strength for varying platform temperature with the standard deviation reported as a percentage of the mean.....   | 94  |
| <b>Table 9</b> Yield stress and ultimate tensile strength relative to variation in bead height with the standard deviation reported as a percentage of the mean...   | 97  |
| <b>Table 10</b> The mean and standard deviation reported for all of the samples per set and with all of the outliers removed from each data set. ....  | 103 |
| <b>Table 11</b> Mean and standard deviation of the yield stress and failure stress of specimens fabricated from the various printers. ....   | 107 |
| <b>Table 12</b> <i>Specimen Dimensions, averages, and standard deviations</i> .....  | 129 |
| <b>Table 13</b> <i>ABS_XY average and standard deviation of properties</i> .....   | 133 |
| <b>Table 14</b> <i>ABS_YX average and standard deviation of properties</i> .....   | 139 |
| <b>Table 15</b> <i>CF-ABS_XY average and standard deviation of properties</i> .....  | 146 |
| <b>Table 16</b> <i>CF-ABS_YX average and standard deviation of properties</i> .....  | 151 |
| <b>Table 17</b> <i>Mean and standard deviation of the <math>T_g</math> calculated three ways based on the storage modulus (<math>E'</math>), the loss modulus (<math>E''</math>), and the tan delta.</i> .....   | 156 |
| <b>Table 18</b> Specimen geometry values and fracture toughness calculated, with standard deviation (STD), using the initial crack length $a$ .....  | 182 |
| <b>Table 19</b> Specimen geometry values and fracture toughness calculated, with standard deviation (STD), using the critical crack length $a_c$ .....   | 183 |

## LIST OF FIGURES

|   |    |
|---|----|
| <b>Figure 1</b> Layer and bead overlap is dictated by the printing parameters and affects the three major fracture domains boxed in red.....  | 4  |
| <b>Figure 2</b> Crack deviations caused by raster voids, weak interdiffusion, and internal defects imparted by the manufacturing process dictated by the polymer chain dynamics in FFF.....   | 5  |
| <b>Figure 3</b> Crack propagated to the bead above the crack plane, specified by the arrows, as it followed the path of least resistance.....   | 8  |
| <b>Figure 4</b> Representation of polymer chains within a deposited FFF bead and the associated tube that confines the polymer chains .....   | 10 |
| <b>Figure 5</b> ABS polymer structure (top) where side chain size and type impact the overall polymer behavior and PLA polymer structure (bottom) .....   | 11 |
| <b>Figure 6</b> Print speed dictates the chain conformation and can lead to a more oriented or less oriented chain structure. ....  | 14 |
| <b>Figure 7</b> The lower entropy system on the left relies on fewer polymer chains to resist fracture at the interface due to a lack of long-range diffusion.....  | 20 |
| <b>Figure 8</b> SENB specimen with the two bead orientations and an example printed SENB specimen post testing with varied crack path due to printing orientation.....  | 27 |
| <b>Figure 9</b> CT test specimen with two potential orientations to measure fracture between layers (top) and through the bead (bottom). A combination of these layers is discussed by McLouth et. al. and forms the mesostructure .....                            | 29 |
| <b>Figure 10</b> Example of DCB test specimen loaded in tension for mode I fracture toughness shown on left. Shown on the right is the orientation of the beads longitudinally with the orange arrow showing crack direction. ....                                  | 34 |
| <b>Figure 11</b> Two different stacking patterns used to investigate the interlayer adhesion. ....  | 36 |
| <b>Figure 12</b> A) Filament based desktop scale FFF schematic B) screw-based pellet extruder in BAAM schematic .....   | 43 |
| <b>Figure 13</b> Small scale print evidence of warping as print pulls off the bed during print.....   | 43 |
| <b>Figure 14</b> End Notch Flexure (ENF) test specimen where failure occurred through the beads and not at a layer-layer or bead-bead interface .....   | 48 |
| <b>Figure 15</b> Specimen size difference between type I, type II, type III, type IV, and type V (from left to right respectively) of the ASTM D638-14 standard .....   | 73 |
| <b>Figure 16</b> Ultimate tensile strength results obtained from ASTM D638-14 Type I, II, III, IV, and V specimen types printed individually and directly onto the bed. Mean, standard deviation, and cross-sectional area are reported for each specimen type..... | 75 |
| <b>Figure 17</b> Bead-to-bead interface failure present in orientations where the bead is aligned in the load direction.....  | 80 |

|  |     |
|--|-----|
| <b>Figure 18</b> Comparison of plaque printed specimens and individual specimens, loaded both along the beads (+00+00) and perpendicular to the beads (+90+00) .....   | 83  |
| <b>Figure 19</b> The naming convention is based on the bed orientation in which the part is deposited along a primary axis oriented as $\theta$ and raster orientation $\alpha$ relative to a local axis with x aligned with the principal axis.....                                 | 84  |
| <b>Figure 20</b> Examples of the naming convention for a Z print (left) and an in-plane print (right) .....  | 85  |
| <b>Figure 21</b> Comparison of the Ultimate Tensile Stress for specimens that appear identical but were printed in different orientation on the platform.....  | 86  |
| <b>Figure 22</b> Comparison of the repeatability for specimens that appear identical but were printed in different orientation on the platform. ....   | 86  |
| <b>Figure 23</b> Increasing fan speed decreases the ultimate tensile load and increases the variability because of warping.....  | 89  |
| <b>Figure 24</b> Visual effects of warping and the subsequent effect in the tensile grips. The resulting bending moment in the middle of the gauge length causes significant deviation from uniaxial tension loading conditions creating an invalid test.....                        | 89  |
| <b>Figure 25</b> Stress versus strain curve comparison demonstrating the effect of nozzle temperature on strength .....  | 90  |
| <b>Figure 26</b> Stress versus strain plots of valid tests for specimens fabricated with varying nozzle temperature A) 220°C B) 232°C and C) 245°C.....  | 91  |
| <b>Figure 27</b> The effects of platform temperature on tensile strength.....  | 93  |
| <b>Figure 28</b> Bead height alters the natural reptation of polymer chains between layers, where larger bead heights create a better environment for polymer chains to achieve strong layer mixing. ....  | 96  |
| <b>Figure 29</b> Multiple Z +90+90 specimens printed during a single print with the nozzle depositing one layer for all specimens. When printing 4 specimens, shown on the left, the increased effective layer time for each specimen causes significant reductions in ultimate..... | 99  |
| <b>Figure 30</b> Location of sequential prints on the print bed. Each individual specimen is printed to completion before moving to the next. ....   | 99  |
| <b>Figure 31</b> Sequential prints versus individual prints in the same orientation (+90+90) provide different ultimate strength results.....  | 101 |
| <b>Figure 32</b> Sequential prints demonstrate variability in strength relative to bed location .....  | 101 |
| <b>Figure 33</b> Ultimate tensile loads of specimens cut using two different methods: CNC and Water Jet.....   | 102 |
| <b>Figure 34</b> Ultimate tensile load of each individual specimen fabricated with CNC or waterjet cutting methods.....  | 103 |
| <b>Figure 35</b> The image on the left shows the cross-section at the failure location during tensile testing for a specimen cut by CNC machining and the image on the right shows a corresponding failure location for a specimen cut using waterjet machining.....                 | 104 |

|  |     |
|--|-----|
| <b>Figure 36</b> Comparison data of machine features for Lulzbot Taz Mini (left), Taz 5 (center), and Taz 6 (right) printers. ....   | 105 |
| <b>Figure 37</b> Average stress vs strain computed from valid results using specimens fabricated and tested with different Lulzbot printers.....   | 106 |
| <b>Figure 38</b> Stress strain plots for each valid individual test specimen fabricated with (a) Taz 5, (b) Taz 6, (c) Mini. ....  | 106 |
| <b>Figure 39</b> <i>Layer-to-layer orientation (YX) and along the bead (XY) isolation. Figure dimensions not representative of actual test specimens.....</i>  | 127 |
| <b>Figure 40</b> <i>MTS load frame with laser extensometer and specimen loaded with reflective tape attached for extensometer.....</i>   | 131 |
| <b>Figure 41</b> <i>Stress-Strain curves for ABS specimens printed in the XY orientation. ....</i>   | 134 |
| <b>Figure 42</b> <i>a) typical break of the specimen set. b-c) Demonstrating failure to break but a bow below the fillet region in RT_ABS_XY_2 .....</i>   | 135 |
| <b>Figure 43</b> <i>a) Failure in Z shape pattern within the fillet region. b) Highlighted (black dashed line) Z shape failure pattern.....</i>  | 137 |
| <b>Figure 44</b> <i>a) 90C_ABS_XY-10 undergoing fracture that does not extend through the width of the specimen. b) Black dashed line boxes highlight the double fracture in specimen 90C_ABS_XY_10.....</i> | 138 |
| <b>Figure 45</b> <i>Stress-Strain curves for ABS specimens printed in the YX orientation .....</i>   | 140 |
| <b>Figure 46</b> <i>a) Stepwise break pattern observed in specimens [dashed black line]. b) Left two specimens show typical range of breakage in the gauge, right two specimens were outliers. ....</i>      | 141 |
| <b>Figure 47</b> <i>a) Specimens illustrating different break locations. ....</i>  | 142 |
| <b>Figure 48</b> <i>a) Specimens illustrating different break locations. b) Specimens illustrating different step sizes between 70C and room temperature. ....</i>   | 143 |
| <b>Figure 49</b> <i>Stress-Strain curves for CF-ABS specimens printed in the XY orientation.....</i>   | 146 |
| <b>Figure 50</b> <i>a) Specimens showing the filing, non-filing, and reduced filing. b) Outlier specimens in the test set.....</i>   | 147 |
| <b>Figure 51</b> <i>Typical break location of test set (left), outlier specimen (middle), gauge length break (right).....</i>  | 148 |
| <b>Figure 52</b> <i>a-b) Multi-layered failure exhibited by specimen 90C_CF-ABS_XY_1, dashed white lines illustrate layer separation.....</i>  | 149 |
| <b>Figure 53</b> <i>Stress-Strain curves for CF-ABS specimens printed in the YX orientation.....</i>   | 151 |
| <b>Figure 54</b> <i>a) Different break locations on specimens. b) typical break pattern. ....</i>  | 152 |
| <b>Figure 55</b> <i>Different break locations on specimens. ....</i>   | 153 |
| <b>Figure 56</b> <i>CF_ABS_XY tested under ambient moisture conditions and soaked to capacity and tested.....</i>  | 155 |
| <b>Figure 57</b> <i>Dynamic Mechanical Analysis of ABS and chopped fiber filled ABS</i>  | 155 |
| <b>Figure 58</b> <i>CF-ABS and ABS bead-to-bead interfaces show that carbon fiber reinforcement improves the interfacial mixing.....</i>   | 160 |

|  |     |
|--|-----|
| <b>Figure 59</b> Shape change associated with heating material beyond the $T_g$ where the material expanded in the bead width and contracted in the bead length.<br>.....        | 160 |
| <b>Figure 60</b> TGA analysis of specimens subjected to moisture versus those under ambient atmosphere demonstrating negligible amounts of trapped water. 162                    |     |
| <b>Figure 61</b> SCB specimen geometry where B is width, R is radius, S is span, and a is the crack length <sup>12</sup> .....   | 172 |
| <b>Figure 62</b> Intrabead fracture SCB specimen orientation .....   | 174 |
| <b>Figure 63</b> Fracture surface of the SCB 33.02mm radius specimens printed at 230C.....   | 178 |
| <b>Figure 64</b> Fracture surface of the SCB 33.02mm radius specimens printed at 220C. Due to cutting location, the notch ended at various points within the printed beads ..... | 179 |
| <b>Figure 65</b> Noticeable effects and variations occur when adjusting the width of the specimen based on the cross section of the figures above .....                          | 180 |
| <b>Figure 66</b> load versus displacement for mode I fracture toughness intrabead .  | 181 |
| <b>Figure 67</b> Deviation from linearity example with straight line applied to load versus displacement curve .....   | 181 |
| <b>Figure 68</b> comparison of the load carrying capacities of the $0.3 \cdot R$ and $0.4 \cdot R$ notch lengths. ....   | 184 |
| <b>Figure 69</b> DIC images of crack growth during specimen loading. From top left to bottom right, the crack growth can be seen in the red boxes.....                           | 184 |
| <b>Figure 70</b> J-R curve for intrabead SCB specimen 14, as an example.....   | 186 |
| <b>Figure 71</b> Fracture toughness dependence on initial notch location .....   | 187 |
| <b>Figure 72</b> Interlayer SCB specimen load displacement plot showing very minimal deviation from linearity.....   | 188 |
| <b>Figure 73</b> Craze within the beads but not at the interface demonstrates different material behavior and properties in the various locations .....                          | 191 |

**CHAPTER I**  
**FRACTURE BEHAVIOR OF FUSED FILAMENT FABRICATED**  
**POLYMERS: A REVIEW**



A version of this chapter was originally published by William H. Ferrell and Stephanie C. TerMaath:

William H. Ferrell and Stephanie C. TerMaath. "Fracture Behavior of Fused Filament Fabricated Polymers: A Review" *Additive Manufacturing* (2020): (submitting soon)

I, William Ferrell, was the primary author of this review with assistance from my Advisor, Dr. Stephanie TerMaath.

## **Abstract**

Despite rapid progress throughout the past few decades, standardization of fused filament fabrication (FFF) techniques and comprehensive characterization of the end-use material behavior remains essential for the FFF manufacture of reliable parts for use as primary structure. Due to the complex nature of the FFF process, strength and stiffness-based material qualification processes alone are not adequate to ensure structural reliability considering the complex rheology, microstructure, and macrostructure of FFF parts. Emphasis on developing a deeper understanding of the processing-structure-performance relationships, effects of defects, and fracture mechanics is essential to fully realize the potential of FFF in the manufacturing landscape. This review consolidates these relevant topics from polymer chain physics to material and part characterization as it pertains to the fracture behavior of FFF products with the goals of informing future work and generating a repository of current knowledge.

## **Introduction**

Fused filament fabrication (FFF) is popular worldwide in industry use and makerspaces due to its low cost, availability,<sup>1</sup> and ease for manufacturing specialized on-demand or customized parts.<sup>2</sup> Through the heating, extrusion, and layered deposition of thermoplastic material, a three dimensional object is produced that relies on the mechanical crosslinking of the polymer chains between

beads of material for strength. In the preceding decades, characterization of FFF parts and materials has been performed through numerous studies investigating air voids,<sup>3-5</sup> additives such as fibers and nanocomposites,<sup>6-15</sup> the chemical makeup,<sup>16,17</sup> and the overall mesostructure of the print and part itself.<sup>18-21</sup> Introducing a filler, such as carbon fiber,<sup>9,22-31</sup> glass fiber,<sup>32</sup> or organic materials,<sup>10,33</sup> can result in improved material properties in FFF parts, and as such, reinforced material is readily available. FFF provides scalability of the manufacture of small parts, such as plastic caps produced using desktop printers,<sup>34</sup> to much larger structures, such as a submarine printed through Big Area Additive Manufacturing (BAAM),<sup>35</sup> allowing for this technique to span a wide range of potential applications.

A necessity for the widespread implementation of FFF parts is the development of material qualification standards to ensure structural reliability. Due to the complex nature of standards development and the rapid development in FFF, most research efforts have focused on utilizing numerous ASTM International and International Organization for Standardization (ISO) testing standards to correlate additives, microstructure, chemical makeup, etc. to the strength and stiffness of those materials.<sup>36-41</sup> Other factors, such as material response under environmental conditions<sup>42-44</sup>, that influence part performance have also been investigated to quantify their detrimental effects on strength. When discussing the scope of effort necessary to qualify materials for end-use, fracture mechanics becomes ever more important in FFF parts due to the manufacturing process itself.<sup>45-47</sup> As the nozzle deposits molten material in a set raster pattern, many potential crack initiation sites are formed including voids, defects, and areas of weak adhesion. Therefore, fracture analysis plays an essential role in the prediction of FFF part failure.

There are three dominant regions for fracture to occur in FFF parts: through the bead (intrabead), between layers (interlayer), and between beads in a given layer (interbead), **Figure 1**, creating a complex environment for crack initiation and growth. For example, the size and shape of the voids between beads (Figure 2)

are dependent on the raster pattern (path of bead deposition) and can be a site of crack initiation, cause multiple crack coalescence, or propagate a single crack through the void. Interlayer and interbead domains where the contact area is smaller or where the polymer chains have poor interdiffusion can initiate and propagate delamination between beads. And, additives or imperfections in the material can create voids and defects in the beads prompting cracks to grow intrabead. As seen in **Figure 2**, cracks in FFF parts commonly propagate through varying types of domain, therefore necessitating the need for multiple fracture mechanics principles to define and predict crack growth. When a crack grows interlayer or interbead, the interlaminar fracture toughness standards used in the composites industry are applicable, however if a crack grows completely intrabead, fracture toughness standards for homogeneous material matrices or chopped fiber composites are needed. It is important to note that the current composite standards should be updated to reflect FFF attributes. A primary goal of this review is to provide a consolidated source of the state-of-the-art in fracture characterization and testing to inform the development of testing standards specific to FFF.

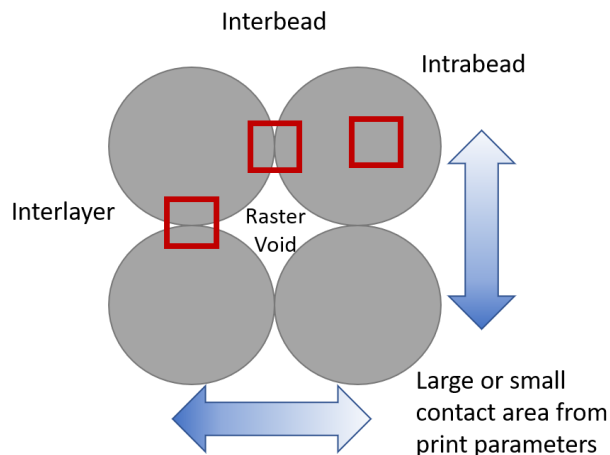


**Figure 1** Layer and bead overlap is dictated by the printing parameters and affects the three major fracture domains boxed in red

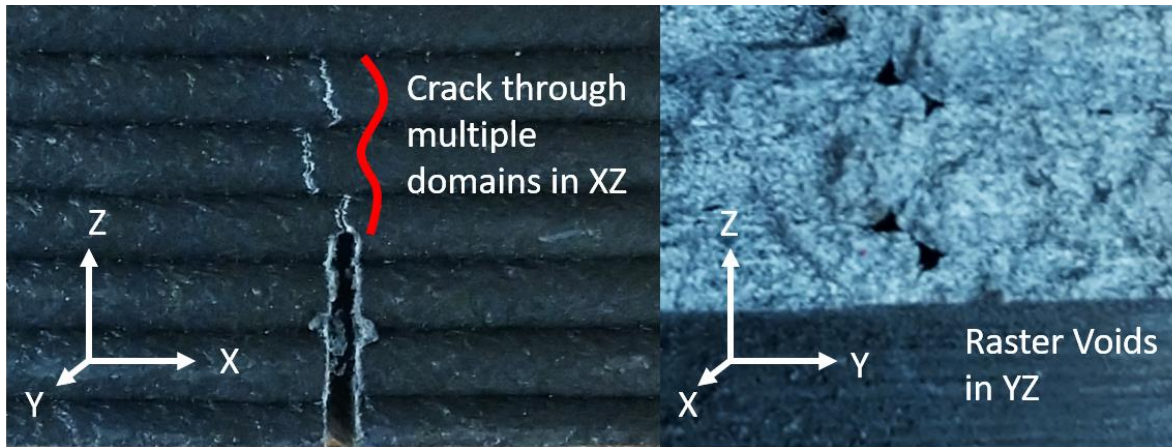


**Figure 2** Crack deviations caused by raster voids, weak interdiffusion, and internal defects imparted by the manufacturing process dictated by the polymer chain dynamics in FFF

With creation of FFF specific fracture testing standards in mind, the processing-structure-performance relationships require continued investigation to expand our knowledge of this critical correlation that directly influences fracture behavior. Fabrication based on the user-specified printing parameters creates cascading effects starting with the part structure itself through the mechanical properties and the material behavior in the various fracture domains. As an example, higher printing temperatures have been shown to improve the interlayer adhesion, however, may simultaneously increase the intrabead void content.<sup>48</sup> Also, printing parameters that lead to poor layer adhesion, such as low printing temperatures, high fan speeds, etc, can cause cracks to grow in the interlayer region.<sup>49</sup> However, optimized printing conditions which are later discussed, have been proven to create a homogeneous or near homogeneous matrix where the FFF part shows little dependency on the layer and bead adhesions.<sup>45</sup>

The printing parameter effects on fracture illuminate the rheological importance of polymer chain behavior in the melt during deposition. Research by

Pascual-González et. al. demonstrates how the consistent use of dynamic mechanical analysis (DMA), thermogravimetric analysis (TGA), and DSC to analyze the factors behind the micromechanical response of FFF parts is important to the testing of FFF parts.<sup>50</sup> This work related the rheological and structural properties in the polymer matrices to strength and stiffness, however it has not been extended to fracture. FFF specific fracture testing standards and qualification procedures need to be developed that account for the multiple fracture domains as well as the complexities of the processing-structure-performance relationships in the FFF parts.

Through an exploration of the rheological phenomena and fracture mechanics concepts as applicable to FFF, a holistic compilation of the state-of-the-art knowledge on the fracture characterization of parts manufactured by FFF is reviewed. Discussion of topics spanning nano and micro-scale polymer chain physics through large scale FFF part production is presented in four sections: Phenomenological Complexity, Fracture and FFF, Small Scale versus Large Scale Fracture Behavior, and Big Area Additive Manufacturing (BAAM) FFF Fracture. Each section provides a brief history of the scientific advancements, assumptions, and limitations of the state-of-the-art in fracture characterization of FFF parts. The objectives of this paper are to guide future standard development of FFF material testing, to inform future research on fracture characterization, and to provide a consolidated review of current knowledge.

## **Phenomenological Complexity**

Thermoplastic polymers are commonly used in FFF, because at elevated temperatures they behave as a fluid allowing for extrusion and then undergo a transition through the rubbery plateau to a glassy, or solid, state during cooling after deposition. An important effect of the extrusion and deposition process on the fracture behavior of the final part is the interdiffusion and amount of contact area

between beads, as interfaces are a known source of FFF part failure.<sup>25,48</sup> Control of the printing process to ensure favorable conditions for mechanical crosslinking at interfaces as well as maximizing infill to reduce the number and size of voids improves fracture performance. The branch of physics that addresses this flow and deformation of matter is rheology, and this section discusses the effects of the printing process on the specific rheological phenomena<sup>51–67</sup> which govern the fracture behavior of the polymer used as the primary print material.

During the FFF deposition process, the molten polymer bead being deposited contributes heat to the adjacent bead and beads of the previous layer, that have already begun cooling, creating the necessary environment at the interfaces between the beads for layer mixing. As previously defined in **Figure 1**, the two types of interfaces are interlayer and interbead, and previous research has quantified differences in the behaviors of these two interfaces due to the variation in thermal conditions during the deposition process.[1] Melt viscosity and chain mobility, which are controlled by the print processing conditions, govern the overall mechanical crosslinking that provides the physical strength and fracture toughness, the materials resistance to crack propagation, of an interface. The melt viscosity determines the overall contact area between deposited beads, and the chain mobility determines the short range and long range interdiffusion. Polymers are held together by a combination of Van der Waals forces and covalent bonds, and for a crack to grow in a polymer matrix both must be overcome and broken. Because a crack propagates along the path(s) of least resistance, **Figure 3**, the contact area and polymer interdiffusion play a significant role in the crack behavior, where raster voids cause crack initiation and deviations and poor interdiffusion reduces the material's resistance to load.

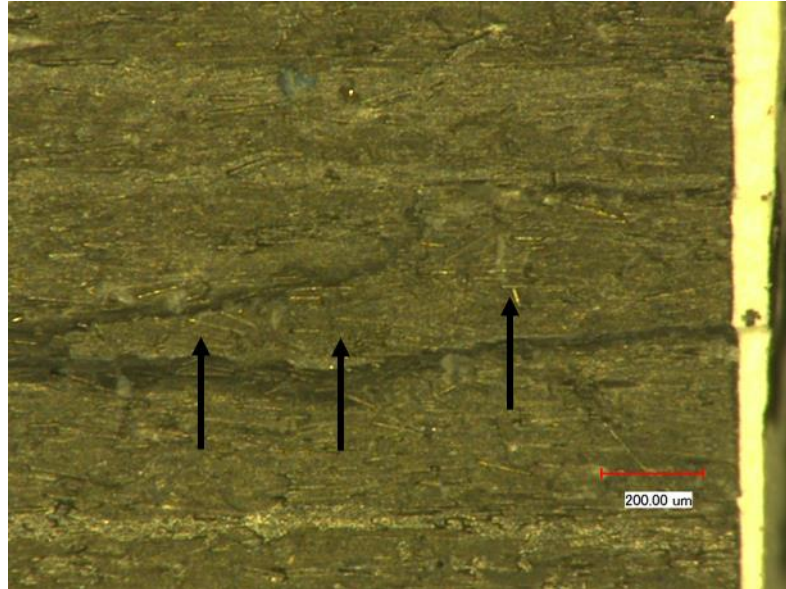


**Figure 3** Crack propagated to the bead above the crack plane, specified by the arrows, as it followed the path of least resistance.

### ***Tube Theory***

It is well established that polymer processing during FFF induces various levels of stress, strains, and strain rates on the polymer chains within the material system.[40] Subsequently, the molecular structure of polymers plays an important role in the material response to various print parameters, such as print speed, extrusion temperature, and print bed temperature. The bulk material property of the printed polymer within the bead, or the intrabead properties, most likely mimic those of non-printed polymers.[68] If confirmed by future research, mechanical properties of a printed bead could be obtained from testing on pre-printed filament with standard values provided by the manufacturer. This relationship would eliminate the need for considering and quantifying the effects of the nearly unlimited combinations of user specified print parameters on printed intrabead

properties. The interfaces on the other hand vary substantially based on the print parameters.[69] During material deposition, a major constraint on the mechanical crosslinking, which dictates the interface strength and fracture toughness, may occur according to the tube concept. The tube concept originated from the inability of two polymer chains to cut through each other in the course of motion, thus dictating a tube-like region that confines each polymer chain. As shown in **Figure 4**, a single bead encompasses many thousands of tubes dictated by the molecular weight of the polymer and the polymer structure. Each region severely restricts the motion of chains orthogonal to the tube and the tube contour.[70,71] The tube diameter is dependent on polymer chain properties such as monomer bulkiness and chain stiffness but not as much on chain length.[62] Thus different polymers will have different inherent monomer bulkiness and chain stiffness which in turn affects the entanglement size ( $N_e$ ) and the statistical segment length ( $b$ ) where the tube diameter ( $a$ ) is equal to  $N_e^{1/2} * b$ . With fracture toughness dependent on the entanglements in the polymer matrix, the polymer chain mobility in the melt dictates the matrix formation at the interfaces in FFF. Because polymer chain mobility depends on the polymer chain properties, the printing parameters, such as speed and temperature, would not have uniform effects across all polymer types used in FFF. Therefore, the relationship between polymer chain mobility and mechanical properties must be uniquely considered for each polymer type.



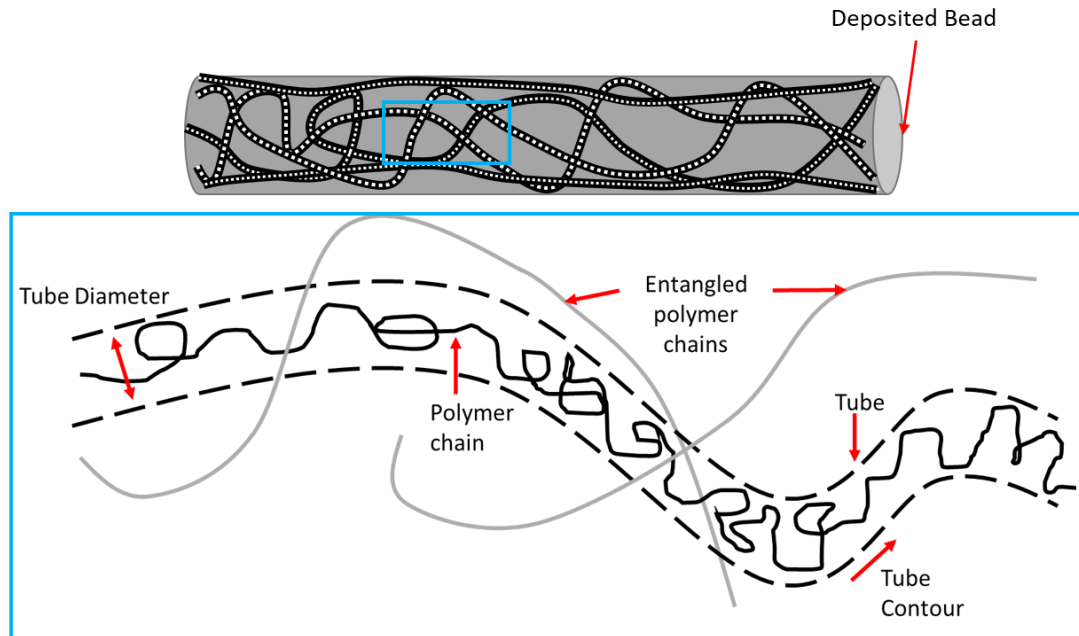


**Figure 4** Representation of polymer chains within a deposited FFF bead and the associated tube that confines the polymer chains

For example, in the case of acrylonitrile-butadiene-styrene (ABS) versus polylactic acid (PLA), two of the most common FFF polymers, the constituent monomers are vastly different in size and mobility. For reference, polystyrene is one of the most common industrial polymers with applications in consumer durable goods, packaging, structural foams, lenses, cable sheathing, etc due to the ease of fabrication and low cost. When copolymerized with acrylonitrile to form styrene-acrylonitrile (SAN) there is an increase in the tensile strength, where the polarity in the acrylonitrile group creates a stronger matrix than pure polystyrene. In the case of ABS, **Figure 5**, the interspersed butadiene provides toughness to the strong SAN matrix due to butadiene's rubbery nature. Each of these structures have different sizes and shapes which impact the tube diameter, where the polystyrene suffers from steric hindrance, or restricted rotation, due to the size of the benzene

rings and thus is the limiting factor in the ABS chain mobility. Compare this with the structure of PLA, **Figure 5**, where there are no bulky pendant groups in the lactic acid monomer or the lactide monomer, where condensation reactions are used to polymerize the lactic acid monomer and lactide is polymerized through ring-opening polymerization. Once again, much like in the butadiene, the side chain bonding and structure provides a more mobile polymer chain in the melt than the styrene in polystyrene or ABS. Each of these FFF plastics have vastly different tube sizes, in part from the polymer chain structure, that dictate the motion of the polymer chains in the melt. Because of the layering of molten plastic in FFF, a new polymer matrix is formed at the interfaces of each bead and layer, which highlights the importance of better understanding the governing polymer chain physics. Due to distinct polymer chain behavior for each print material, standardizing print parameters across all polymers may not be possible and instead must be optimized for each polymer type.

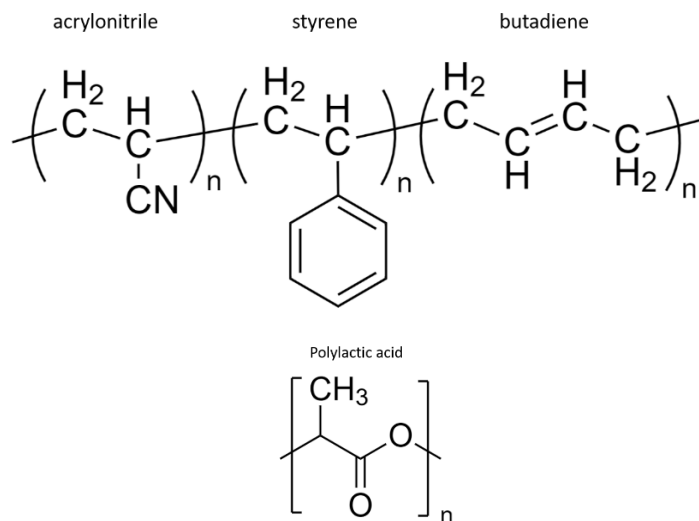


**Figure 5** ABS polymer structure (top) where side chain size and type impact the overall polymer behavior and PLA polymer structure (bottom)

Due to the reliance of fracture toughness on the entanglement density of polymer chains and that the entanglement density is predicated on both the tube diameter and the polymer chain dynamics, better connection of polymer physics to mechanical behavior within FFF printed material is needed. Tube diameter is experimentally obtained by the comparison of measured rheological behavior to the predictions of theoretical models, which requires well entangled polymers on time scales shorter than the stress relaxation time for the polymer chains. Mathematically, several ansatzes, which are initial estimates and assumptions of the solution to a mathematical problem, are available to describe the tube diameter and entanglement behaviors in a number of ways. The most successful of such has been the Lin-Noolandi ansatz, which has had consistent success in describing experimental results for tube diameter in a wide range of polymers.[72–75] The Lin-Noolandi ansatz reveals how  $N_e$  varies with local chain dimensions, where bulkier monomers with a corresponding larger monomer volume, or more flexible chains with a smaller segment length increase the entanglement length. Equations 1 and 2 demonstrate the assertions of the Lin-Noolandi ansatz, where the number of chain segments cohabiting a volume pervaded by an entanglement strand is a universal constant for flexible polymers.[75]

$$\frac{\left(N_e^{1/2}b\right)^3}{N_e\Omega} = C \quad \text{eq 1.}$$

$$N_e = \frac{C^2\Omega^2}{b^6} \quad \text{eq 2.}$$

Where  $N_e^{1/2}b$  is the size of one entanglement strand,  $\Omega$  is the monomer volume, and  $C$  is the universal constant roughly equal to 22.4.[75] Rephrasing these cases by replacing the entanglement size with the tube diameter, the packing length can be related to the monomer volume and the segment length. This packing length is the length which delineates the overfilling of space. By replacing  $N_e$  with  $a = N_e^{1/2}b$  to obtain  $a = C \Omega/b^2$  the packing length  $p \equiv \Omega/b^2$ . The associated size scale of local encounters between neighboring chain segments is the best description of the packing length. If an entanglement chain is not flexible

enough or has bulky monomers, the inability to adopt compact random walk configurations inhibits other chain segments from approaching, necessary for entanglements. Thus, in the Lin-Noolandi ansatz, the tube diameter is proportional to the packing length.[74]

A second ansatz was proposed by Milner,[75] and Rubinstein and Colby in the study of polymer solutions in order to encapsulate the polymer chain behavior observed in said polymer solutions.[76] This ansatz asserts that the volume pervaded by one entanglement strand  $a^3$  contains a constant number of close contacts between chain segments ( $C^3$ ) and has a characteristic volume of a close contact equal to  $p^3$ . A third ansatz was recently introduced by Qin et. al. in the study of oriented and stretched polymer melts, indicative of melts in strong aligning flows. This ansatz asserts a fixed number of close contacts between an entanglement strand and neighboring chains.[62] And, even in highly concentrated polymer solutions, the polymer chain behaviors, including the nonlinear viscoelastic properties, differ from that of polymer melts.[77,78] The difference in polymer chain behavior in solution and in the melt are seen in the difference in prediction for how the tube diameter changes when comparing ansatz II and ansatz III. As pertaining to FFF and fracture, inhibition of the entanglement chains greatly reduces the fracture toughness of the interface between beads and layers. To better understand polymer entanglements in the melt, mathematical ansatz III most closely relates the boundary conditions of the printing process with polymer entanglement. Print speed, print temperature, polymer type, fan speed, and bed temperature all play a part in the polymer chain dynamics in orienting and stretching flow.

## ***Polymer Melts in FFF conditions***

Due to the environment of oriented and stretched polymer melts, created by the FFF process, further discussion of the Qin and Milner ansatz, ansatz III, is discussed in regards to the conceptualizing of polymer entanglements in oriented and stretched polymer melts at the interlayer and interbead interfaces.[62]As the polymer melt is deposited onto the previous layer, the polymer chains are stretched at various intensities depending on the print speed. Higher print speed results in larger shear forces that stretch and orient the polymer chains, **Figure 6**. The effects of this stretching and orienting is discussed, but first, a better understanding of polymer chain level behavior must be established.

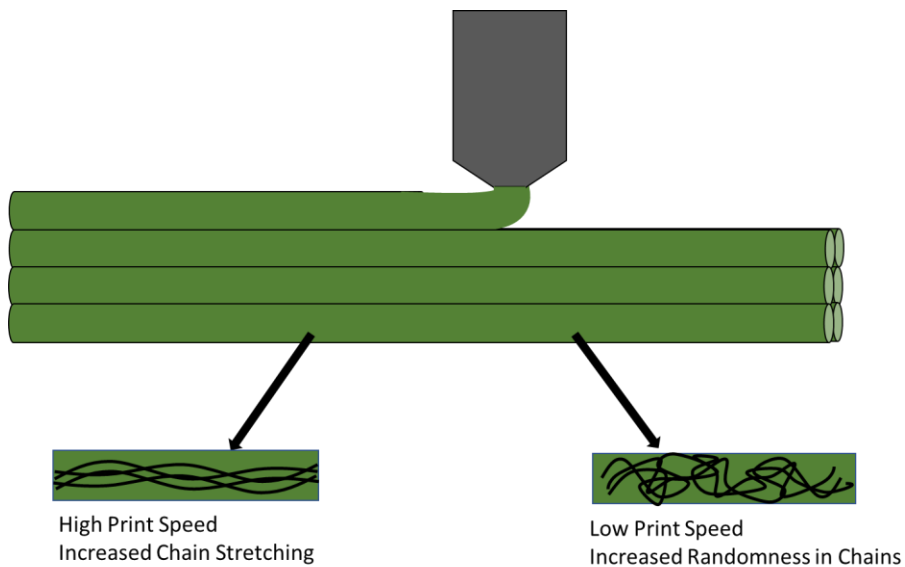


**Figure 6** Print speed dictates the chain conformation and can lead to a more oriented or less oriented chain structure.

In the deposition process of FFF and the subsequent restriction of the motion of the polymer chains in a polymer melt once deposited, the tension applied to a bead creates changes in the molecular motion itself. Polymer chains are commonly modeled as random walks, where the location or movement of the end of the polymer chain moves as a stochastic process. The force extension in the system is most likely not large enough to fully extend the polymer chains and thus be affected by the limit of full extension, where a fully extended chain is restricted in motion. Thus, the polymer chains can be described rheologically by Gaussian random walks, which is the stochastic process based on step sizes that vary according to a normal distribution. This Gaussian random walk can then be used to determine the configuration free energy of a Gaussian chain under uniaxial pulling.[62] The configuration free energy can be written as:

$$\frac{3kTR^2}{2Nb^2} - FR_z \quad \text{eq 3.}$$

Where  $k$  is Boltzmann's constant,  $T$  is temperature,  $R$  is the end to end separation vector,  $N$  is entanglement size,  $b$  the statistical segment length,  $F$  is force, and  $R_z$  is the end to end separation vector along the length of the tube. From this relationship, Qin and Milner demonstrated a force dependence and a crossover tube diameter analysis that is reliant on how close the chains achieve maximum elongation. For isotropic melts, the pervaded volume is estimated as  $a^3$ , but for chains under tension it is estimated using the volume of the cylinder pervaded by a test strand.[62] The extension of ansatz III to a fixed number of contacts per entanglement strand when deformed to an isotropic melt at fixed topological complexity predicts a scaling of tube diameter so long as the force is not large enough to bring the chains to full extension. This application of ansatz III provides consistent results with experimental data without large adjustments of  $N$  away from the Kuhn length.[62] Qualitatively, ansatz III asserts that the chains

stretched out along a direction have a lesser tendency to fill the space around their own monomers and subsequently have more room for entanglement strands from nearby chains and additional contacts. This stretching has a twofold effect on the potential strength and fracture toughness of the part.

The first effect is the increase in the overall number of contacts between polymer chains, which as discussed previously, increases the space available for polymer entanglements. Increased entanglements result in the increased mechanical crosslinking that helps provide the materials resistance to fracture. However, the second effect is in direct opposition to the first, where the increased stretch of the polymer chains also causes a decrease in the tube diameter discussed above. As applied to FFF, for a constant volume of extruded material, increasing the print speed is associated with a decreased melt viscosity of the material, shear thinning, caused by the disentanglement of polymer chains. When sheared, polymer chains begin to disentangle and align which causes the observed viscosity to drop, and the degree of disentanglement is shear rate dependent. While this orienting can create more potential contacts for entanglements between polymer chains, the overall contact area is decreased between the deposited beads and large voids are manufactured into the part.

Qualitatively in ansatz III, there is a decrease in both the tube diameter and  $N_e$  for chains under tension, where there is a lesser tendency of polymers to fill the space around their own monomers. This relationship is also consistent with a binary view of entanglements as binary interactions between chains, which are the result of chain-shrinking algorithms.[79,80] This binary view is also supported by simulation results on primitive path rearrangements that occur as a result of two chain segments crossing over each other in the melt.[81] The topological entropy can be interpreted in such a way as to having these chains approach, interact, and either wrap around or not, then so on and so forth. This environment creates the random dodging and interacting necessary to produce the randomly braided structure that is the entangled polymer melt. However, with the rapid cooling in the

FFF system, there are changes to the boundary conditions allowing for the interactions necessary for those randomly braided structures.

Thermodynamically, each system seeks to maximize entropy, through the reduction of order, and polymer chain entanglements are the result, however when energy is introduced to the system in the form of shear stress, the resulting topological entropy is changed. The orienting of chains creates an environment for short range interdiffusion, where these shallower interactions dominate in the structure. In order to achieve the highest resistance to fracture, a heavier reliance on the covalent bonds of the polymer chains is needed. This means that the ends of polymer chains need to be able to diffuse across layers and deep within adjacent beads. This long-range diffusion is stifled by the orienting and stretching of polymer chains, **Figure 6**. In terms of impact on fracture, this creates a layer-to layer and bead-to-bead contact area with high reliance on the weaker Van der Waals forces that can be more easily deformed and yield at the crack tip, seen as crazing. Pairing this condition with increased void content could potentially lead to a macroscopic brittle behavior, despite the microscopic conditions that contribute to ductile fracture.

Leveraging the polymer rheology of stretched chains in the melt provides the possibility of tailoring areas in a part for a specific property using print parameters and opens up interesting future avenues in predictive computational modeling. In the case of tensile testing performed by Ferrell et. al.[69] there was a phenomenon noticed where higher printing temperatures, which provide better diffusion and theoretically higher strength, led to a slightly lower ultimate tensile strength and a much higher elongation to break with load applied only to the interface between beads. Ultimately as this finding pertains to fracture and future tailoring of parts, the pairing of low print speeds and high nozzle temperature could create areas of higher toughness, and simultaneously pairing standard nozzle temperature and higher print speeds could create areas of higher strength. Future molecular dynamics simulations for the predictions of polymer chain locations with FFF boundary conditions and structural dynamics simulations for testing crack growth



in FFF materials can eliminate this conjecture leading to a bright future for the field of custom part design.

### ***Polymer Diffusion for Bead Contacts***

Polymer diffusion, which is the primary mechanism in which the FFF deposited beads interact with previous beads, is an additional area that demonstrates the impact of entanglements, temperature, and molecular weight.[82] The Doi-Edwards theory has a direct relation with diffusion and temperature.[83] Recent work has investigated and elaborated on polymer architectures effect on polymer dynamics in the melt[84] due to the Rouse model not being generally applicable even in the simple case of unentangled polymers.[85,86] When discussing polymer diffusion and the computations surrounding it, hydrodynamic radius ( $R_h$ ) and radius of gyration ( $R_g$ ) are introduced, and while they are more commonly reserved for polymer solutions, they do appear in polymer melt texts, which could extend to future FFF investigations. These terms are defined as the average distance of a chain element from the center of gravity of the chain and are proportional for a linear chain molecule.[55] These values are required when calculating the diffusion coefficient  $D$ .

The interpretation of the diffusion work and scaling laws as it relates  $D$  to  $R_h$  and  $R_g$  is that, in a coarse grain sense, polymer chains are comparable to tracer particles which “sense” local viscosity differences form the macroscopic viscosity. Diffusion is then predicated on the sizing of those particles and as such the radius size of the particles, when compared to the  $R_h$  and  $R_g$ , must be similar for this hypothesis to hold, which it does according to the data collected by Chremos et. al.[84] The hypothesis of particles in diffusion comparing to the  $R_h$  and  $R_g$  extends to rationalizing the dependence of  $D$  based on the hydrodynamic polymer size by conceptualizing polymers in the melt as soft particles. The conceptual relationship of polymers in the melt as soft particles can then be extended to entangled polymer

systems by assumption of a transition similar to that found in the Stokes-Einstein relation. This transition is observed in dynamically heterogeneous liquids due to the formation of particles clusters, and if such a transition exists on the scale of  $R_g$  to heterogeneous polymer dynamics underlying the entanglement phenomenon, then the power law scaling transition of shear viscosity would occur.[84] Chremos et. al. suggest that the transition between the power law scaling observed for all different polymer architectures can be rationalized as the emergent dynamical heterogeneity that is characteristic of strongly interacting soft particle systems.[87]

It is of note that higher printing temperatures or printing parameters that allow the print to stay hotter longer can counteract the stretching and orienting effects discussed earlier. By keeping the system at a higher temperature, the capacity for the polymer chains to reach more entropically favorable configurations is increased which presents itself as a reduction of the internal stresses imparted by the manufacturing process. The increased capability of the polymer chains to reach more favorable configurations is the concept behind annealing systems, but because the FFF process constantly is adding heat to the system with each deposited layer, an annealing type reaction is expected in the previous layers, depending on how long the polymer chains remain above a temperature that allows high chain mobility. The extent to which the polymer chains can move and anneal is discussed above and is tied to the hydrodynamic radius or the radius of gyration of the polymer chains in question. It is also dictated by whether the polymer can form crystalline domains in which the crystalline versus amorphous domains are impacted by the temperature. The more favorable the entropic conformations, as shown in **Figure 7**, of the polymer chains at the interface are, the more resistant that interface is to crack growth.

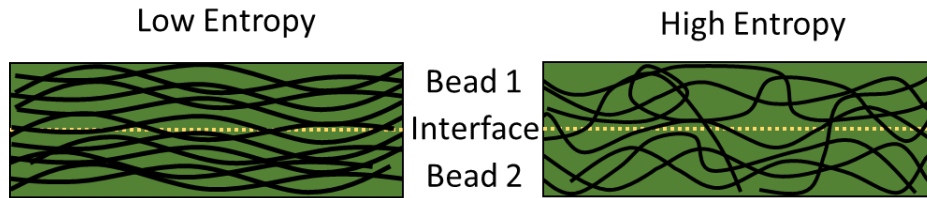


**Figure 7** The lower entropy system on the left relies on fewer polymer chains to resist fracture at the interface due to a lack of long-range diffusion

Keeping the previously discussed annealing in mind, Song. et. al. demonstrated that in a PLA system, the FFF process led to a higher percent crystallinity as compared to the injection molding using differential scanning calorimetry (DSC).[88] This was then associated with an increase in the fracture toughness of the material. However, when the researchers annealed the FFF test specimens, they found no increase in the percent crystallinity but found a decrease in the overall strength. Through the annealing process of PLA, it is expected that there would be an increase in the crystalline domain size or number of crystalline domains, increasing the overall percent crystallinity. The stretching and orienting effect of the polymer during deposition could be the limiting factor for increased crystallinity, where the chains reached a certain topological entropy that was limited. If the highest crystallinity was achieved, the crystalline regions impeded the polymer chains in the amorphous phase during the annealing process. The polymer chain mobility restriction hypothesized by the crystalline domains is an interpretation of the potential causes by the authors and was not further investigated by Song et. al., but that hypothesis does demonstrate an increased need in the research of FFF specific phenomena at the polymer chain level during the FFF process.

## ***Rheological Phenomena: Slip Springs and Beyond***

The modeling and understanding of polymer chain dynamics is ever evolving without a consensus on the molecular basis of polymer rheology itself. Much like the aspirations in other branches of physics, a reductionist truth of fundamental polymer physics has been pursued since the theories introduced by Kuhn, Flory, and de Gennes.[89–91] Advances in the experimental measurement and technology surrounding polymer physics has seen coinciding advances in the rheological theory, and thus it is likely that FFF could provide further testing grounds for modeling and testing. Due to the complex boundary conditions of changing temperature, pressure, orientations, etc, further development of the molecular dynamics simulations of polymer chains provide an interesting proving ground for better understanding polymer chain dynamics.

A competing model to the tube theory[92] and evidence of contradictory behavior of polymer chains under extension[78] are provided by several more recent advancements in polymer rheology that are of importance for future predictive modeling of FFF. One of the competing models for polymer chain dynamics was developed by Likhtman et al that contests the future value of the tube theory due to a lack of definition of the primitive path in terms of chain coordinates.[64,93] This contestation has led to the above discussion on tube theory where certain explanations and ansatz do not hold in different environments such as melts versus solutions. The primary parameter in tube theory is the singular number of entanglements, but if tube theory is not a single parameter theory, then finding this number of entanglements is not pertinent.[64] Likhtman et. al. proposed the slip-spring model which states individual entanglements can potentially be modeled by slip-springs and subsequently defines entanglements as persistent contacts between the mean paths of polymer chains.[64] The slip-springs concept suggests that tube diameter,  $a$ , does not impact the fluctuations of the chain perpendicular to the tube, but only the properties along the contour. The impact of the tube diameter only affecting the properties along the contour

changes the physical meanings of the parameters  $a$  and  $N_e$ , or  $Z$  as listed in the referenced work. Instead, a constructed freely jointed chain with a certain contour length and average square end-to-end distance would have  $Z$  steps of length  $a$  in an equivalent chain. The change of the physical meaning of the parameters  $a$  and  $Z$  separates the number of entanglements from the associated mathematical parameter by changing the interpretation.

Further work exploring the slip-spring model includes expansion into contour length fluctuations and constraint release.[94–96] An important take away from these works is the ability to model various constraint release environments and slow chain versus fast chain behavior. In the case of FFF where the part has varying heat transfer into the system after initial deposition, the overall ability to more readily track and predict chain locations in multiple different constraining environments is important. One of the major advantages of the slip spring model for researchers is the contribution of a model with the equations of motion for chain coordinates clearly specified which is lacking in the aforementioned tube theories. In the expansion and exploration of the constraint release and contour fluctuations, there is preliminary success of applying a tube model description to the results of a slip-spring model. This agreement provides some evidence that these two different approaches can be reconciled and unified in the future.

On a fundamental level, in FFF literature, the reptation of polymer chains between layers dictates the mechanical crosslinking necessary to provide the toughness of the manufactured part. The governing concepts explored above in relation to polymer chain behavior and entanglements still hold, but it is important to note that the way in which we model the behavior of polymer chains can increase the change in how those materials resist fracture, and therefore their calculated fracture toughness. Changes in how polymer entanglements are viewed and therefore modeled need to be included in the adaption of fracture mechanics for FFF. While utilizing the governing rheology and thermodynamics to conceptualize changes in fracture toughness is one aspect, the predictive modeling and

integrated computational materials engineering worlds require accurate polymer chain and rheology models.

## **Fracture Mechanics and FFF**

Before World War II, there was little emphasis placed on material defect or crack propagation in a material. It was thought that these small cracks could not affect the grand structures built of steel during this time. However, after a series of catastrophic failures in the 1940s-1950s, including the hull cracking of the SS Schenectady and the three fatal de Havilland Comet crashes, rapid expansion in the field of fracture mechanics occurred.[97,98] Fracture mechanics is the encompassing field in solid mechanics that addresses the propagation of a crack through the material and the material's ability to resist this failure. During this same time, the damage tolerance approach to engineering design gained traction due to the emphasis it placed on a material's ability to withstand a small enough amount of damage that could be detected during inspection and be repaired prior to failure through a maintenance plan, to design and build safer structures. At the heart of this damage tolerance approach is the ability to predict crack growth through a material using fracture mechanics principles. Given the complexity of modern engineered parts, such as those fabricated with FFF, the need for advanced fracture mechanics testing, modeling, and analysis has never been greater. This section discusses the current state-of-the-art and future needs in fracture mechanics for FFF.

### ***Fracture Mechanics Concepts and Terminology***

In order to better understand the current state of the art in fracture specific to FFF, a brief history and discussion with regards to the different fracture terminology and concepts is provided. Previously discussed intrabead, interbead,

and interlayer regions, **Figure 1**, within an FFF part all have different rheological concerns as outlined above, but also create the need for different fracture terminology and tests to be applied. The establishment of fracture mechanics was based on observations by A. A. Griffith[99] when analyzing the failure of bulk glass, where the stress needed to break bulk glass was about 100x less than the stress needed to break the atomic bonds of glass. To reconcile this difference, Griffith hypothesized the presence of microscopic flaws in the bulk material. To test this hypothesis, Griffith introduced a large surface crack in the material and found that the stress to cause fracture multiplied by the square root of the crack size was almost constant. This finding however, created a conundrum in linear elastic materials where the stress at the tip of a sharp flaw is infinite. A thermodynamic approach was subsequently introduced to explain this relation. As a crack propagates the surface areas on either side of the crack grow, therefore increasing the surface energy. This correlation allowed the stress at fracture ( $\sigma_f$ ) of a specified crack length (a) to be related to the Young's modulus of a material (E) and the surface energy density of the material ( $\gamma$ ).

$$\sigma_f \sqrt{a} = \sqrt{\frac{2E\gamma}{\pi}} \quad \text{eq 4}$$

$$\sigma_f \sqrt{a} = \sqrt{\frac{EG_c}{\pi}} \quad \text{eq 5}$$

The quantity  $2\gamma$  was combined into the Griffith Critical Energy Release Rate,  $G_c$ , directly relating the force of fracture to the bond energy. As the applicability of Griffith's finding was limited to brittle material systems, additional investigation under the direction of G. R. Irwin at the Naval Research Laboratory advanced its relevance to a much larger range of materials which would include metals and then later polymers.

Despite the applicability Griffith's equation to steel, the predicted surface energy was unrealistically high for ductile materials. Irwin et. al. theorized the role of plasticity at the crack tip in affecting the fracture of ductile materials, which includes the polymer material systems currently used in FFF.[100] In a ductile

material, a plastic zone forms in front of the crack tip and grows with increasing stress until the crack propagates and the elastically strained material behind the crack tip is unloaded. Due to a cyclic plastic loading at the crack tip, energy is dissipated in the form of heat and Irwin subsequently introduced a dissipative term,  $G_p$ . Depending on the brittle or ductile nature of the material meant that the surface energy density ( $\gamma$ ) or the dissipative term ( $G_p$ ) respectively dominated in the energy release rate,  $G$ , as shown in equation 6.

$$G = 2\gamma + G_p \quad \text{eq 6}$$

Irwin and his colleagues next introduced the ability to calculate the amount of energy needed for fracture based on the asymptotic stress and displacements around the crack tip in a linear elastic solid, equation 7 where  $\sigma_{ij}$  are the Cauchy stresses,  $r$  is the distance from the crack tip,  $\theta$  is the angle with respect to the plane of the crack and  $f_{ij}$  are functions dependent on geometry. The stress field around the crack was related to the value  $K$ , the stress intensity factor. Beyond the stress field relationship, he proposed that if the plastic zone is small compared to the size of the crack, a purely elastic solution may be used to calculate the energy needed for fracture using  $K$ . The stress intensity factor relationship to the energy release rate is shown in equation 8.

$$\sigma_{ij} = \frac{K_I}{\sqrt{2\pi r}} f_{ij}(\theta) \quad \text{eq 7}$$

$$G = G_I = \begin{cases} \frac{K_I^2}{E} & \text{plane stress} \\ \frac{(1-\nu^2)K_I^2}{E} & \text{plane strain} \end{cases} \quad \text{eq 8}$$

When  $G$  reaches the critical value,  $G_c$ , fracture becomes unstable. The corresponding critical value of  $K$  is called fracture toughness denoted as  $K_{Ic}$  in the plane strain condition for mode I. There are three different modes in fracture mechanics depending on the loading system. Mode I is characterized as crack opening, mode II as in plane-sliding, and mode III as out of plane tearing. Very commonly a material will experience some mixed-mode type loading requiring the determination of mixed mode fracture properties. Fracture properties may be dependent on material orientation. For example, within crystalline polymeric



systems used in FFF, grain boundaries and orientations caused naturally or by the manufacturing process can cause orientation specific material intrabead properties.

In order for a material system to be treated as a linear elastic problem, the fracture must be brittle, but many polymeric systems undergo too much yielding and must be analyzed using elastic plastic fracture mechanics. Both Rice[101] and Cherepanov[102] independently developed a new toughness measure in the case where sufficient deformation at the crack tip occurs. Both showed that an energetic contour integral around the crack was path independent and was named as the J-integral. The  $J_{Ic}$  is the mode I strain energy release rate per unit fracture area for elastic-plastic fracture mechanics (EPFM) and in the J-integral approach, it reduces to the Griffith criteria for linear-elastic fracture mechanics (LEFM).

While the above concepts apply to intrabead fracture, additional consideration is needed for interface damage prediction, because the interfaces between layers appear to have different properties than the bead material. Within FFF parts there are many interfaces between beads that behave similarly to the interfaces between lamina in composite laminates. For example, in the case of a composite laminate, interlaminar fracture toughness testing is used to quantify delamination between the lamina. The distinction is made between fracture tests of homogeneous materials and composite materials in the current ASTM and ISO standards[103], and both types of tests are needed to characterize fracture in FFF parts.

### ***Linear Elastic Fracture Mechanics for FFF***

Several studies on FFF fracture toughness have been performed using the LEFM framework laid by Griffith and Irwin. Song et. al.[88] produced three sets of single edge notch bend (SENB) test specimens, machining these specimens from 0° and 90° FFF polylactic acid (PLA) blocks, **Figure 8**, as well as an injection-

molded PLA block. The SENB test specimen is a standard test for plane-strain fracture toughness of plastic materials.[104] The  $0^\circ$  specimen was designed to test the intrabead fracture toughness and the  $90^\circ$  specimen was designed to test the interlayer fracture toughness. The test set up employed a laser extensometer and a digital image correlation (DIC) system to observe the displacement as these tests. Song et. al. produced an R-curve for the fracture toughness from the test results, where the stress intensity factor  $K$  is plotted as a function of the crack extension. The results demonstrate that the FFF material is tougher than that of the injection molded material and the fracture toughness is higher in the  $0^\circ$  direction when compared to the  $90^\circ$  print direction.

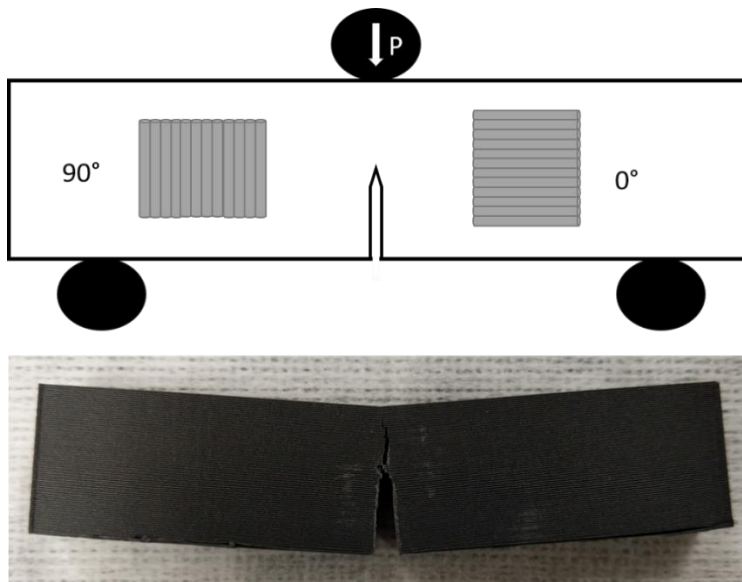


**Figure 8** SENB specimen with the two bead orientations and an example printed SENB specimen post testing with varied crack path due to printing orientation

These results are explained because the ultimate tensile strength in the 0° print direction is higher than that of the 90° print direction, but the higher fracture toughness of the 90° print direction compared to that of the injection molded PLA is unexplained. The 90° print direction specifies loading directly onto the layer and bead interfaces which from tensile testing has shown to have weaker adhesion leading to the explanation of orientation dependence. However, a fully homogeneous part from the molded specimen should theoretically have superior toughness. The authors concluded that there were very different methods of crack propagation at play due to the filamentous nature of the FFF part. For the 0° specimen, the crack advanced in a single plane with an occasional kink by 90° causing delamination between the inter-layers, resulting in dissipation of additional energy. For the 90° specimen, the crack advanced in an irregular fashion where the topology of the fracture surface possessed a higher surface area characterized by a wavy fracture surface. The fracture surface of the injection molded specimen was much smoother than those of the FFF printed parts. This fracture surface suggested a surface boundary layer with different mechanical properties that were consequential with the non-uniform cooling rates in the injection molding process.

Song et. al. concluded that the mechanical response of FFF PLA was anisotropic and asymmetric in nature with a direction-dependent fracture behavior. Also compared to the homogeneous injection molded PLA, the FFF specimens had a higher crystallinity, reducing the ductility of the material and increasing the fracture toughness. This increased toughness is due to the layered and filamentous nature of the 3D printed material and the associated complexity induced in the microscopic mechanisms of fracture.

McLouth et. al. further investigated intrabead fracture by correlating fracture toughness ( $K_{Ic}$ ) variation with mesostructure in FFF parts through the use of compact tension tests.[105] The compact tension (CT) specimens for mode I fracture toughness tests used in this study were printed in multiple orientations containing various raster orientations. The print orientations were labelled XZY, XYZ, and ZXY with XY defining in-plane directions and Z the out-of-plane direction.

Therefore, the material is deposited in the XY plane and then built up with layers in the Z direction. So, these specimens were printed on the bed in three different configurations with two different patterns for the infill of the part. This notation is important to define the orthotropic nature of the parts, but also provides a point of confusion in comparing studies due to varying terminology and experimental controls. With the XZY print orientation, the crack was planar to the XY plane and the two raster orientations were  $0^{\circ}/90^{\circ}$  and  $+45^{\circ}/-45^{\circ}$ . In the XYZ print orientation, the crack was planar to the XZ plane and were printed with the same two raster orientations as the XZY. Finally, the ZXY print was printed with the crack planar to the ZY plane, also with the same raster orientations.

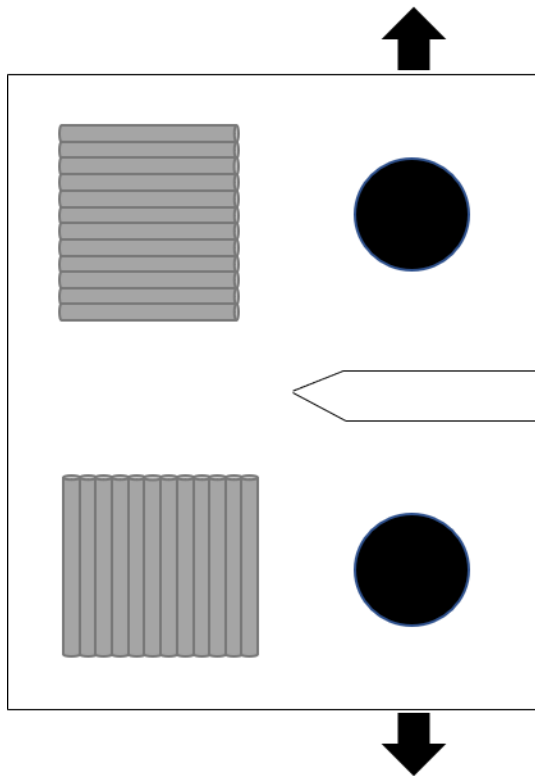


**Figure 9** CT test specimen with two potential orientations to measure fracture between layers (top) and through the bead (bottom). A combination of these layers is discussed by McLouth et. al. and forms the mesostructure

McLouth et. al. found that the print and raster orientation in the CT samples significantly impacted the fracture toughness. It is noted that in the work by McLouth et. al. they found that the specimens exceeded the conditions needed to be reported as true linear-elastic plane-strain fracture toughness requirements. In the two orientations that had half or more of their filaments orthogonal to the crack plane, the fracture toughness was higher due to these filaments being an obstacle to crack propagation. These fracture toughness values were in the middle of reported ranges for bulk ABS with the range of  $K_{Ic}$  being roughly 1.1-4 MPa\*m<sup>1/2</sup>. In the other orientation the fracture toughness was lower due to a reliance on the weak interfilament bonding. The toughness, as reported in Table 2, was on the lower side of the reported toughness values for bulk ABS. It was also reported that when filaments adjacent to the crack tip were loaded along their axis, the plastic zone was larger. The plastic zone size dependence provides a compelling argument of the importance of the mesostructure to the measured fracture toughness in FFF. Additionally, in the +45°/-45° specimens the mesostructure encouraged branching which showed improve toughness, however this deviation to a mixed mode of failure contributes to increased energy dissipation and increased toughness. Mesostructural effects are an important analysis when discussing the qualification of material versus certification of parts, where the material resistance to fracture is impacted heavily by the mesostructure and therefore becomes even more application dependent.

### ***Elastic-Plastic Fracture Mechanics in FFF***

Previous work in the strength and stiffness domains have endeavored to determine fully optimized printing parameters for FFF polymers such as PLA. The goal of these studies was to determine how to fabricate an FFF part without producing a substantial number of voids in the final part due to the raster pattern. A study performed by Arbeiter et. al. examined the fracture properties of PLA produced by FFF in the CT and SENB test configurations for orientations of 0°,

90°, and 0°/90° printed using optimized parameters[45], and several important observations were made. One observation was that for monotonic loading, the LEFM criteria could not be met, therefore the EPFM criteria or the J-integral should be used for fully optimized printing conditions. For these tests the J integral was evaluated according to the following two equations based on the SENB standard[106]:

$$J_0 = \frac{\eta U}{B(W-a_0)} \quad \text{eq 9}$$

$$J = J_0 * \left(1 - \frac{(0.75\eta-1)\Delta a}{W-a_0}\right) \quad \text{eq 10}$$

where, U is the integral of the force-displacement (P- $\delta$ ) curve,  $\delta$  is a geometry dependent factor,  $a_0$  is the initial crack length, and  $\Delta a$  is the incremental crack propagation.[106] Both W and B are geometry values from the test specimen of length and width respectively. This study was performed with the three-point bend test using the SENB test specimen to determine mode I fracture toughness.

The results from this study demonstrated that there were no voids or other processing induced defects for the 0° and 90° specimens, but some small observable defects were seen in the 0°/90° specimen. The 90° specimen had the highest fracture toughness with the 0° and 0°/90° specimens comparable. Upon inspection, Arbeiter et. al. found that there was slightly more area of plastically deformed material, shear lips and ruptured fibrils, on the fracture surface compared to the other orientations. The slight improvement of ductility could be explained by the shorter time between bead depositions in this orientation. Arbeiter et. al. note that for the 0° orientation the beads are deposited over the length of 44 mm, where they were only printed over a length of 10 mm for the 90° specimen. Due to the insulating nature of polymeric material, the high cooling rates of the surface of each deposited bead compared to the middle could be a reason for the difference in fracture toughness and observed ductility. Arbeiter et. al. recommended further exploration using more sophisticated morphology characterizations such as small angle x-ray scattering (SAXS) or wide-angle x-ray scattering (WAXS) to provide further insight into the morphology and fracture-mechanical properties. This

recommendation by Arbeiter et. al. further supports the need for advanced rheological experimentation to pair with the FFF specific processes to elucidate the processing-structure-performance relationships.

### ***Interlaminar Fracture in FFF***

While acknowledging the different layering orientations, the work presented so far did not explicitly state the testing of FFF materials as a laminate and additionally these studies used fracture toughness test specimens that are commonly performed on homogeneous or non-layered materials. Hart et al performed the same SENB test previously mentioned on ABS polymer and described the printed specimens as “laminates”, where each lamina is a layer of material parallel to the print bed with a nominal thickness of the corresponding layer height.[107] Specimens were then designed to examine the orthotropic fracture behavior of this ABS material, where vertically printed SENB samples, horizontally printed SENB samples, and obliquely printed SENB samples were manufactured to encompass the various orientations. The vertically printed SENB specimens were designed to test the inter-laminar fracture toughness, the horizontally oriented SENB samples were designed to test the cross-laminar fracture toughness, and the obliquely oriented SENB samples provided qualitative results corresponding to fracture between and across laminae.

In the vertically printed SENB specimens, Hart et al found that the mode I stress intensity factor  $K_{Ic}$  and the critical elastic-plastic strain energy release rate  $J_{Ic}$  were comparable to brittle solids and not typical of plastically deformable polymers like bulk ABS. The observed brittle fracture was contradicted by the evidence of tearing-type fracture at the interface which is common for ductile materials. However, regions of un-fractured material were observed as a result of the porosity and individual raster lines were also identifiable. As compared to the Song et al study, the processing parameters of the specimens in this study were

not optimized to maximize infill and minimize porosity. Hart et al hypothesized that the fracture behavior in the specimens is strongly influenced by magnitude and regularity of the porosity; where areas of high weld line overlap cause stress to build up and as crack initiation ensues, the crack moves to the fracture plane of least resistance which corresponds to regions of high porosity. In the case of these vertically printed SENB specimens, it is noted in the literature that there is a reduced ultimate tensile strength that is heavily influenced by layer time and build height on small scale printers.[69]

In the case of the horizontally oriented SENB specimens, multiple types of fracture are observed through SEM micrographs. A Power law fit was employed in the J-R curve and deviations were attributed to the high variability in FFF parts, which is well documented.[69] There was significant whitening in the crack propagation region as a result of crazing, indicative of elastic-plastic deformation. Crazing occurs in polymers due to the materials combination of weak Van der Waals forces and strong covalent bonds. For tension loading conditions, local stress overcomes the Van der Waals forces and results in a small crack but it is not enough to break the covalent bonds. This crazing happens in front of the crack front before crack propagation in these testing configurations and is why they are indicative of elastic-plastic deformation. Within the SEM micrographs of the crack propagation region, porosity attributed to the manufacturing process is visible, as well as micro-porosity in the material. This micro-porosity was attributed to the cavitation process during failure provided by the butadiene component.

The measured cross-laminar elastic-plastic  $J_{Ic}$  is comparable to that of injection molded ABS SENB specimens but are slightly lower. This slightly lower value was attributed to the porosity present in the FFF process. Higher porosity decreases the overall material volume and results in increased crack propagation. Interestingly enough in this study, laminae orientation dictated the crack path based on the obliquely oriented tests, and crack path did in fact follow the weaker fracture toughness, the inter-laminar toughness. Hart. et. al found that the



interlaminar fracture toughness was almost an order of magnitude lower than that of the cross-laminar fracture.

Aliheidari et. al. employed the double cantilever beam (DCB) test specimen in order to test the fracture resistance and interlayer adhesion of FFF printed ABS, **Figure 10**, due to the nature of the layered structure and the considerable impact the adhesion between layers has on the mechanical properties.[108] This standard specifies testing for the mode I interlaminar fracture toughness of unidirectional fiber reinforced composites. The DCB test specimen was chosen due to the prevalence of beam-type fracture specimens for fracture characterization of layered materials. This test specimen was printed to the specified dimensions directly onto the bed with all the layers oriented in the longitudinal direction, **Figure 10**. This control of the print direction in this case results in the same interface and print conditions locally in sequential layers where cross hatched layers would have provided additional variability.

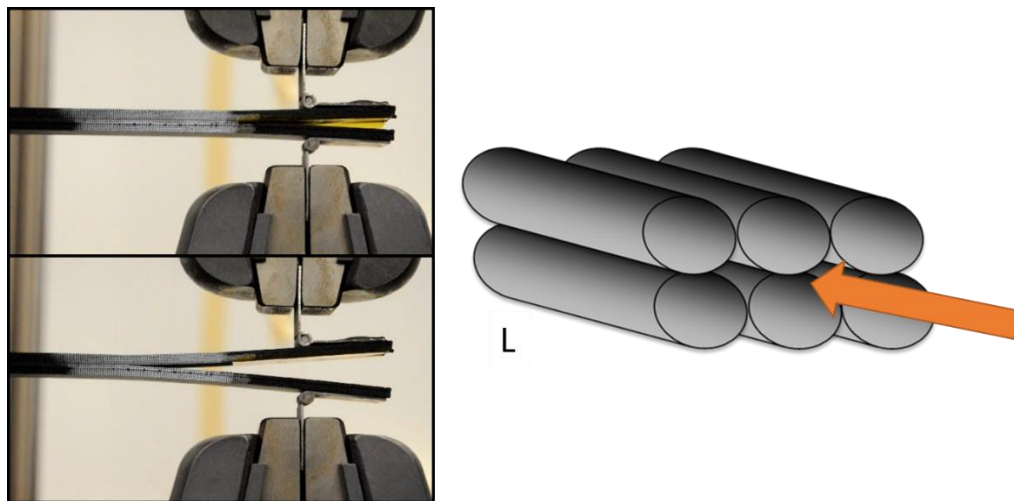


**Figure 10** Example of DCB test specimen loaded in tension for mode I fracture toughness shown on left. Shown on the right is the orientation of the beads longitudinally with the orange arrow showing crack direction.

In the results of this testing the load increased, but at a nonlinear decreasing rate, after crack initiation started and before the onset of an unstable, sudden crack growth. The load increase was attributed to the toughening or the damage zone development ahead of the crack tip. An increase in the load before crack initiation was observed for specimens with a higher nozzle temperature, which is attributed to the better layer adhesion in higher print temperature parts. Additionally, the amount of surface intact was greatly increased with increasing nozzle temperatures. The surface intact ratio specified by Aliheidari et al is the ratio of the actual and nominal fracture surface areas. So, in this case due to the voids imparted by the FFF process, there is not a uniform and completely homogeneous cross section. The higher surface intact ratio is attributed to the viscosity of the polymer melt at different temperatures affecting the surface area contact, as discussed in the previous sections.

The apparent fracture resistances of these specimens, measured using the J-integral method, significantly increased with increased print temperature. The resistance to fracture is a coupled consequence of the interlayer adhesion and the mesostructural features. Aliheidari et. al. decoupled these two by introducing the interlayer fracture resistance calculated by the surface intact ratio. It is noteworthy that even when adjusting for the mesostructural effects, the interlayer  $J_{Ic}$  did not converge to a single value, indicating a stronger mechanical crosslinking present in higher print temperatures. These values were comparable to bulk ABS when printed at 240°C and agrees with the dynamics discussed in previous sections, where increased temperature and increased time at temperature allow for a greater inter-diffusion of polymer chains between layers.

Interlayer fracture toughness was also investigated by Young et. al. using a modified version of the ASTM D5528 DCB specimen.[46] These specimens were compared to the same ABS and carbon fiber reinforced ABS (CF-ABS) material manufactured using hot press molding (HPM) and in the SENB configuration. Young et. al. found a reduction in the fracture toughness compared to the HPM specimens and that the fracture toughness of the CF-ABS was lower than the

unreinforced ABS in both cases. In the case of the DCB tests, both materials demonstrated some nonlinearity prior to macroscopic crack extension, likely due to crack tip plasticity or onset of the crack at the center of the specimen. The amount of fracture toughness reduction imparted by the FFF process of two-fold for ABS and ten-fold for CF-ABS, resulting from the ductile and brittle fracture respectively. The explanation was that the CF-ABS rasters cool much quicker, reaching the glass transition temperature four times quicker than pure ABS. This rapid reduction in temperature results in decreased ability for the polymer chains to reptate between layers. Young et. al. note that the processing parameters were not optimized for fracture toughness and instead were optimized to produce a reproducible test. This distinction is currently an important component of FFF research, where mesostructured versus material properties are hard to discern and often times compound effects.

In the work done by Spoerk et. al. however, the interlayer strength in PLA was evaluated parametrically by analyzing the various effects of layer height and deposition temperatures on two different raster patterns of printed PLA specimens.[109] The interlayer fracture toughness was evaluated using the DCB specimen and the two patterns consisted of layers stacked directly on top of each other and shifted to an extent to where the beads sat on top of the contact area between the beads in the previous layer, **Figure 11**.

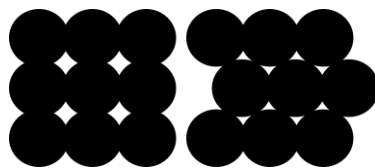


**Figure 11** Two different stacking patterns used to investigate the interlayer adhesion.

Spoerk et. al. found that the shifted layer-design outperformed the stacked layer design for intra-layer loadings, however the stacked layer design provided the best fracture toughness for interlayer loading. They also reported that higher printing temperatures create more plastic deformation during testing and in the highest printing temperature, craze formations and irregular crack paths were observed similar to those that a molded part would exhibit. When the printing parameters were optimized for inter-layer strength, Spoerk et. al. found parts with homogeneous cross-sections, high degrees of diffusion between layers and the aforementioned failure surfaces. They concluded that under the best settings, the DCB test, which is meant to test layered structures, did not provide any insight into the inter-layer cohesion and suggest that under optimal printing conditions, other tests such as the SENB test be used.

### ***Complexity of fracture in FFF***

Fracture mechanics as a field is barely a century old and considerable progress has been made encompassing various material systems, elastic-plastic behavior, inclusions, voids, and other complex behaviors relevant to the damage tolerance of FFF parts. The advancements in fracture mechanics have created a wealth of knowledge but also demonstrate the importance of choosing the appropriate test type for the material and fracture behavior under consideration. Additionally, relating microscopic phenomena to macroscopic response to load is a cornerstone of fracture mechanics and with that comes the need for further evaluation of FFF relative to the material microstructure which is governed in large part by the print parameter settings.

A major observation by Arbeiter et. al. was that the fracture behavior is not highly dependent on the printing orientation when the print parameters are optimized. Arbeiter et. al. found that the 90° orientation demonstrated higher ductility which was attributed to less time between subsequent rasters and therefore good thermodynamic conditions for interdiffusion and crystalline domain

formation. The orientation independent behavior was only observed in the SENB specimens and Arbeiter et. al. attributed that to the specimen shape and symmetry differences between the CT and SENB specimens. This study shows that it is possible to achieve almost homogeneous fracture toughness in FFF test specimens.

The change in the fracture toughness to be independent of orientation suggests that the internal mesostructure is itself a toughening mechanism that can be explored. The two prominent domains are the interlayer and the intrabead with a relatively brittle interlayer and the tougher intrabead. These two domains interact within a part that is printed with multiple directions causing potential toughening through mixed mode fracture.[105] However much like in other polymer based materials there was an increase of toughness with fiber content to a point. Each system and additive creates variance where the returns diminish, but it is common that additives such as fibers can create initiation sites for further crack propagation within the matrix.[110] Increasing the fiber content increases the elastic moduli and adds in voids causing a move towards more brittle fracture. Overall the major contribution to the toughness in the FFF polymer system is the covalent bonding of the polymer chains and the overall mixing obtained, where the near homogeneous fracture surface demonstrated equal or higher fracture toughness in mode I. With the complex nature of the FFF parts in mind, a summary of available data for the fracture toughness of FFF plastics is provided in **Table 1** and **Table 2**.

**Table 1** Test specimen and fracture toughness of PLA by various authors to date with standard deviation (S.D.) provided when available. Not valid shows specimens that exceeded the linear elastic range and therefore K or G do not apply.

|                            |      | PLA           |             |   |      |
|----------------------------|------|---------------|-------------|---|------|
|                            |      | Test Specimen | Orientation | K <sub>IC</sub> (MPa m <sup>1/2</sup> ) | S.D. |
| Song et. al. <sup>88</sup> | SENB |               | 0°          | 5.05                                    | 0.19 |
|                            |      |               | 90°         | 4.06                                    | 0.15 |
|                            |      |               | moulded     | 2.87                                    | 0.51 |

|                                |      | PLA           |             |   |      |                                     |      |
|--------------------------------|------|---------------|-------------|---|------|-------------------------------------|------|
|                                |      | Test Specimen | Orientation | K <sub>IC</sub> (MPa m <sup>1/2</sup> ) | S.D. | J <sub>IC</sub> (J/m <sup>2</sup> ) | S.D. |
| Arbeiter et. al. <sup>45</sup> | CT   |               | 0°          | Not valid                               | -    | -                                   | -    |
|                                |      |               | 90°         | Not valid                               | -    | -                                   | -    |
|                                |      |               | 0°/90°      | Not valid                               | -    | -                                   | -    |
|                                | SENB |               | 0°          | -                                       | -    | 5750                                | -    |
|                                |      |               | 90°         | -                                       | -    | 6790                                | -    |
|                                |      |               | 0°/90°      | -                                       | -    | 5960                                | -    |

|                               |     | PLA           |                |                                     |      |
|-------------------------------|-----|---------------|----------------|-------------------------------------|------|
|                               |     | Test Specimen | Top            | G <sub>IC</sub> (J/m <sup>2</sup> ) | S.D. |
| Spoerk et. al. <sup>109</sup> | DCB |               | 220°C /0.3mm   | 3850                                | 340  |
|                               |     |               | 200°C/0.25mm   | 1300                                | 200  |
|                               |     |               | 250°C/0.25mm   | Not valid                           | high |
|                               |     |               | 210°C/0.25     | 5100                                | 690  |
|                               |     |               | 210°C/0.2      | 2000                                | 600  |
|                               |     |               | <b>Shifted</b> |                                     |      |
|                               |     |               | 220°C/0.3mm    | 1180                                | 150  |

**Table 2 Test specimen and fracture toughness of ABS and carbon fiber ABS (CF-ABS) by various authors to date with standard deviation (S.D.) provided when available.**

| ABS                         |                     |                                  |       |                              |           |    |
|-----------------------------|---------------------|----------------------------------|-------|------------------------------|-----------|----|
| Test Specimen               | Orientation         | $K_{Ic}$ (MPa m <sup>1/2</sup> ) | S.D.  | $J_{Ic}$ (J/m <sup>2</sup> ) | S.D.      |    |
| Hart et. al. <sup>110</sup> | SENB                | 0°                               | -     | 2260                         | -         |    |
|                             |                     | 90°                              | 0.789 | 0.131                        | 256       | 84 |
|                             |                     | 75°                              | -     | -                            | -         | -  |
|                             | SENB from Lu et. al | moulded                          | -     | -                            | 3600-5900 | -  |

| ABS                         |                 |                              | CF-ABS                       |                              |                              |      |
|-----------------------------|-----------------|------------------------------|------------------------------|------------------------------|------------------------------|------|
| Test Specimen               | Print Condition | $G_{Ic}$ (J/m <sup>2</sup> ) | S.D.                         | $G_{Ic}$ (J/m <sup>2</sup> ) | S.D.                         |      |
| Young et. al. <sup>46</sup> | DCB             | 225°C                        | 1800                         | 210                          | 360                          | 60   |
|                             |                 |                              | $G_{Ic}$ (J/m <sup>2</sup> ) | S.D.                         | $G_{Ic}$ (J/m <sup>2</sup> ) | S.D. |
|                             | SENB            | hot press moulded            | 3440                         | 150                          | 3090                         | 380  |

| ABS                               |                    |                                       |         |  |         |        |
|-----------------------------------|--------------------|---------------------------------------|---------|--|---------|--------|
| Test Specimen                     | Nozzle Temperature | $J_{Ic}$ (J/m <sup>2</sup> ) apparent | S.D.    | $J_{Ic}$ (J/m <sup>2</sup> ) corrected | S.D.    |        |
| Aliheidari et. al. <sup>108</sup> | DCB                | 210°C                                 | 953.71  | 29.83                                  | 2167.56 | 67.62  |
|                                   |                    | 230°C                                 | 21720   | 60.77                                  | 3560.65 | 99.62  |
|                                   |                    | 240°C                                 | 2731.87 | 119.94                                 | 3907.55 | 143.13 |

| CF-ABS (BAAM)               |              |          |                              |      |
|-----------------------------|--------------|----------|------------------------------|------|
| Test Specimen               | Initial Temp |          | $G_{Ic}$ (J/m <sup>2</sup> ) | S.D. |
| Nycz et. al. <sup>111</sup> | 50°C         | cold     | 630                          | -    |
|                             |              | hot      | 4230                         | -    |
|                             | 70°C         | cold     | 670                          | -    |
|                             |              | hot      | 3850                         | -    |
|                             | 100°C        | cold     | 1560                         | -    |
|                             |              | hot      | 3420                         | -    |
|                             | 150°C        | cold=hot | 5410                         | -    |

| ABS                            |                   |                    |                               |      |
|--------------------------------|-------------------|--------------------|-------------------------------|------|
| Test Specimen                  | Print Orientation | Raster Orientation | $K_Q$ (MPa m <sup>1/2</sup> ) | S.D. |
| McLouth et. al. <sup>105</sup> | XYZ               | +45°/-45°          | 1.62                          | 6%   |
|                                |                   | 0°/90°             | 1.69                          | 6%   |
|                                | ZXY               | +45°/-45°          | 1.97                          | 3%   |
|                                |                   | 0°/90°             | 1.75                          | 5%   |
|                                | XZY               | +45°/-45°          | 1.28                          | 2%   |
|                                |                   | 0°/90°             | 1.39                          | 5%   |

From the current literature on fracture toughness evaluation there is no consensus on the best approach to fracture testing, given the dissent, on whether or not to characterize FFF part behavior as similar to that of a laminate. Both the behavior of a laminate or of a homogeneous part are observed in FFF parts, depending on the printing parameters, and thus the rheological phenomena at play. The research discussed in this section demonstrates the importance of the print parameters on mesostructure and the subsequent effects on fracture behavior. Further exploration into the laminate versus homogeneous classification of the behavior of FFF parts is needed in order to create the robust standards that are essential to the qualification of materials in FFF applications. While most research to date has focused on mode I, mode II and mixed mode fracture must also be fully characterized to ensure the structural reliability of FFF parts under general loading conditions. Exploration into mode II ( $G_{IIc}$ ) been initially performed but on a limited basis.[49]

### **Scale up of FFF**

One of the interesting evolutions of the FFF landscape is the simultaneous advancement of small scale, desktop style printers and industrial scale, Big Area Additive Manufacturing (BAAM) printers. BAAM systems were originally developed by Oak Ridge National Laboratory (ORNL) in conjunction with Lockheed Martin with the goal of printing large components at high rates with lower-cost material.[113] This original technology was primarily proof-of-concept and later ORNL partnered with Cincinnati Incorporated to develop a BAAM system at the prototype stage which has now become commercially available. This system offered a process that is 10x larger in size and 200x faster than conventional FFF systems.[29] Both desktop printers and BAAM share the overarching print mechanism of layering 2D shapes of molten plastics to create a 3D end part, however the mechanisms and the print strategies used are quite different. Small scale desktop printers utilize filament, which is an extruded wheel of plastic in a set diameter that is then fed into the machine to be melted. In the case of BAAM



printers, plastic pellets are fed into a screw extruder where they are heated, melted, and mixed before extrusion. The schematics of the filament-based and pellet-based nozzles are diagramed in **Figure 12**. The major differences here are the mechanisms to obtain the melt temperature and the requirements of print speed and layer times. Despite both printers fabricating parts using the FFF technique, there are significant phenomenological differences relevant to the fracture behavior between parts printed on a large- and small-scale printer.

The relative volume to surface area substantially changes between large scale and small-scale prints creating different build strategy requirements to create a dimensionally accurate and mechanically sound part. As the molten plastic leaves the nozzle, it instantly begins a cooling process from the localized atmosphere in the area directly surrounding the nozzle and the print. In the case of the larger prints, there is a larger volume of heated material creating a higher temperature in the area directly surrounding the print and near the nozzle. However, contrasting with small scale prints, there is a larger amount of free volume compared to print volume, which drastically cools the surface area of the parts. Taking the common nozzle size of a BAAM printer (7.62mm) and the common nozzle size of a desktop FFF printer (0.4mm) and comparing the volume to surface area ratios of a 10mm long extruded section of filament demonstrates the basis for the difference in how the prints interact with a cooling environment. The volume to surface area ratio of the BAAM section was 1.38 whereas the ratio was 0.098 for the desktop printer. Having a higher volume to surface area ratio in an insulating material means more heat is retained to stay above the glass transition temperature. If we invert the 0.098 ratio to calculate surface area to volume ratio, the surface area is nearly 10x that of the volume, creating surface area that is cooled at a much more rapid rate than with BAAM. In these areas the surface polymer chains contract and are frozen into place, building internal stress and shape deformation, commonly referred to as warping.

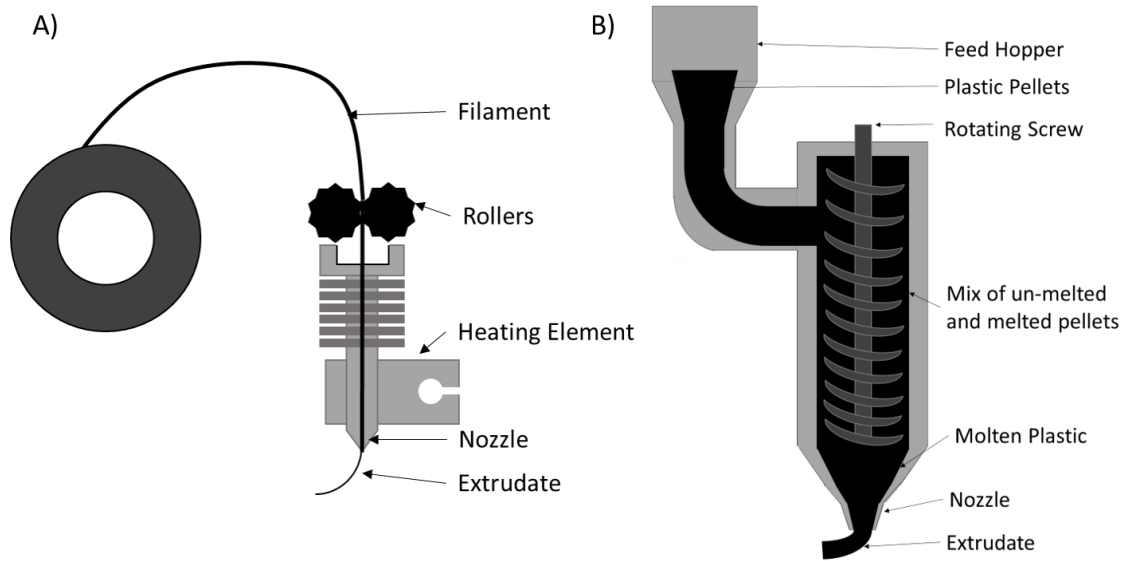


**Figure 12** A) Filament based desktop scale FFF schematic B) screw-based pellet extruder in BAAM schematic



**Figure 13** Small scale print evidence of warping as print pulls off the bed during print

This difference between the large- and small-scale prints creates a different optimization for print temperatures and layer times, where larger prints suffer more from sagging and smaller prints suffer more from warping, **Figure 13**. In order to avoid these undesirable effects, build strategies are changed with regards to cooling and patterning, creating a corresponding variation in the mechanical properties including fracture toughness.

In the case of print speed, the overall ability of the print to retain heat influences the optimal pattern for the desired result. In the case of BAAM, building in down time between prints and creating longer layer times is necessary to avoid the sagging discussed previously, however in the small-scale prints, faster layer times is needed to ensure optimal material mixing at the layers. If the small-scale prints do not experience a certain amount of mixing at the layers, there is a complete lack of adhesion. The restriction imposed on print quality by layer time is extreme in small scale prints, where surface finish, layer adhesion, and dimensional accuracy are all affected by the layer time. There are a few ways to offset this detrimental effect at the small scale, including changing the nozzle temperature, fan speeds, and utilizing enclosures. These strategies differ on the BAAM printers where the extrudate temperature is dictated by the speed and power of the screw in the single screw extruder system. The temperature and melt quality are influenced by multiple zones of mixing and melting along the screw extruder. Due to the multiple zones of melting, this differs from the small scale where there is a single location where the polymer is melted. That difference results in a difficult comparison of “nozzle temperatures” with regards to scaling up of prints and effects.

Previous work on the BAAM system has followed similar paths to that of desktop printers with research providing insight into the strength and stiffness and improving these properties through the addition of short carbon fibers.[9] The addition of carbon fibers reduced the coefficient of thermal expansion (CTE) and the fiber reinforcement acted as an enabling material to help provide more consistent printing conditions.[113] Beyond the carbon fiber additions for better

printing quality, a tamping mechanism was developed by ORNL which provided significantly improved interlaminar strength.[29] Compton et. al. studied the thermal profile of a part during print and from this profile related part distortion to the printing conditions which provided insight into print strategies for these large-scale prints.[114] Compton et. al. concluded that the steady state temperature of the top layer prior to the new layer deposition can be used as an indicator for cracking and warping in thin wall sections.[114] A major takeaway from the aforementioned study was that the ambient temperature in the build chamber had the largest effect on the size of the print that can be printed successfully.[114] In addition to exploring strategies for build optimization, Ajinjeru et. al. studied the rheological behavior of thermoplastic systems with suitability for BAAM printing in mind. This work led to a suggested viscoelastic model to predict the ability to extrude/print materials in question.[115–118] And, much like desktop FFF, fracture mechanics investigations are relatively new to the open literature signaling a shift towards further qualification efforts.

There are numerous similarities between the small scale and BAAM set ups, such as the effects of bed temperature, material quality, fillers, etc that are not discussed here. By pointing out the differences between the set ups, the stage is set for a major distinction moving forward. Despite sharing the same overall concept of layering molten plastic to create a three-dimensional shape, the local area thermodynamics and scale of the two systems greatly impacts layer to layer adhesion. To date, no studies comparing BAAM and desktop fracture toughness of FFF polymers has been published and therefore the printers' effects on fracture toughness at various scales has not been isolated. With the different factors at play, small scale and BAAM printers may need to be categorized and investigated independently, where common approaches to fracture may theoretically make sense across the platforms but do not apply in practice.

## BAAM Fracture

The latest development from ORNL for BAAM systems is substrate temperature control for interlaminar fracture toughness improvement.[119] Kishore et. al. implemented the use of infrared radiation (IR) to preheat the surface of a printed layer to beyond the  $T_g$  prior to the next layer being deposited. In order to test the effectiveness of the IR preheat process for interlaminar strength, Kishore et. al. utilized the DCB test discussed earlier. Kishore et. al. calculated the fracture toughness using the LEFM approach. Through the recording of load versus displacement, the energy release rate  $G$  was calculated by:

$$G = \frac{3P\delta}{2bA_0} \quad \text{eq 11}$$

where  $b$  is the sample thickness,  $P$  is load,  $\delta$  is displacement, and  $A_0$  was the initial crack length. Three different lamp conditions and printing speeds were used. The slowest and intermediate speeds showed improved fracture toughness in the conditions which exposed the print to two 500-watt IR lamps at a set height. A large improvement was observed in the fracture toughness when the IR lamps were positioned as close to the print as possible and printed at the slowest speed. In these conditions, introducing a longer time and more heat to the system created a better environment for interlayer diffusion as demonstrated by increased interlaminar fracture toughness. Condition three at the lowest print speed reduced the overall fracture toughness leading to a degradation of ABS conclusion of the high intensity lamps. With higher extrusion temperatures and larger heating provided by IR there was always a reduction in the interlaminar fracture toughness most likely due to a polymer degradation and introduction of voids within a printed bead.

This research was expanded upon by Nycz et. al. using the same set up of infrared preheating on BAAM printed structures.[112] What Nycz et. al. demonstrated was an experimental set up for in-situ control of the substrate temperature in order to control interlayer mixing. The IR preheating was consistently able to raise the temperature of the previous layer to 150°C and

improve the fracture toughness by over 500%. This work demonstrated that raising the substrate temperature beyond the  $T_g$  is a viable way to improve the polymer chain mobility across the interface and create a better environment for long range mixing.

As of now, investigations of the fracture toughness of BAAM materials in the open literature is limited as the technology is rapidly expanded and improved. Further fracture toughness specific investigations into BAAM materials is necessary to quantify parametric effects on fracture, such as the specified printing parameters and fracture specimen type. Currently for BAAM, only the DCB specimen type has been utilized in investigating mode I fracture, but further testing of mode II and mixed mode fracture and the associated specimen types must also be addressed. A preliminary investigation to determine  $G_{IIC}$  using an End Notch Flexure (ENF) test was unsuccessful when failure occurred through the beads instead of along an interface whether the specimen was oriented for interface failure of sequential layers or bead-bead interface failure within the same layer. A leading cause of inconclusive test results is caused by the inability to achieve crack initiation and propagation along an interface, when the interface is not planar, **Figure 14**. This conclusion is based on a singular set of tests with one material; however, the results indicate the need for a rigorous set of standards for specimen preparation, testing, and results interpretation. While the introduction of new testing standards for strength and stiffness in FFF is already underway, additional research to support fracture standards is needed and the continued investigation of BAAM as a unique FFF subset is important.

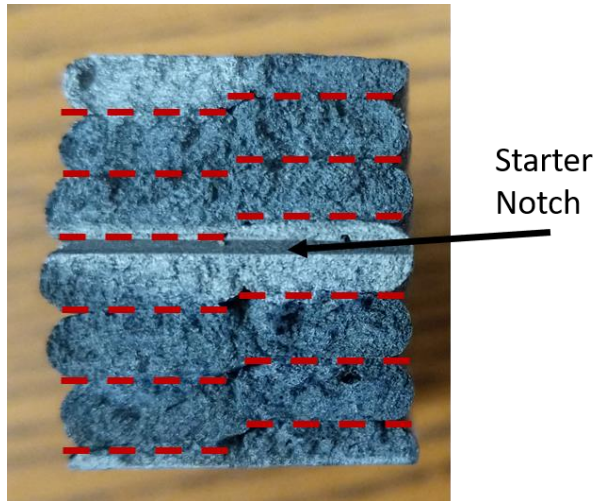


**Figure 14** End Notch Flexure (ENF) test specimen where failure occurred through the beads and not at a layer-layer or bead-bead interface

## CONCLUSIONS

While this review focused on the FFF of polymers, each of the many types of additive manufacturing (AM) technology including stereolithography,[120,121] selective laser sintering,[36,122] and FFF [123–125] spanning many material types provide advantages and disadvantages, offering a range of manufacturing choices to meet the desired purpose of the part or product. The future of the AM landscape requires further investigation of the fracture behavior of AM parts in order to achieve widespread acceptance for fabricating primary structure. Specific topics for future study identified through this review are listed as follows:

- FFF, an industry favorite, has advanced substantially, but in order for more rapid adoption to take place, fracture toughness investigations and evaluations must become more common place in material qualification.
- In the field of fracture mechanics, the experimentally obtained properties of a material are sensitive to the test configuration and dimensions.
- The quest to better understand the physical complexity that governs the diffusion of polymer chains and entanglement phenomena at the interface in FFF is still ongoing and ever complicated.

- The physics and thermodynamics of molecular chain motion, entanglement phenomena, and diffusion is still not clear, but these are the fundamental sciences governing the joining and adhering of polymer melts
- Unification of the testing procedures for fracture tests of FFF parts could provide a major boost to those working on physics based multi-scale modeling efforts, where isolating a certain set of rheological boundary conditions at the layer to layer level reduces the overall variance in validation of models to experiments.
- Standardized testing is also essential for material qualification and part certification given the varying testing procedures and nomenclature throughout the literature.
- As the study of the effects of defects becomes more common place, unified testing standards would provide a clearer picture of individual effects of forced or circumstantial defects.
- In addition, further exploration into the classification of the material as homogeneous or as a laminar is important for the design of fracture tests and standards in the future.
- In the aforementioned AM technology, this similar investigation into fracture mechanics and AM specific standards should take place to further put AM materials on the forefront of the manufacturing landscape.

### **Acknowledgments**

Financial support was provided by the Naval Education Engineering Consortium, grant N00174-16-C0033, under the direction of Dr. Maureen Foley at the Naval Surface Warfare Center Carderock Division.



## REFERENCES

- [1] B. Brenken, E. Barocio, A. Favaloro, V. Kunc, R.B. Pipes, Fused filament fabrication of fiber-reinforced polymers: A review, *Addit. Manuf.* 21 (2018) 1–16. <https://doi.org/10.1016/j.addma.2018.01.002>.
- [2] U. Kalsoom, P.N. Nesterenko, B. Paull, Recent developments in 3D printable composite materials, *RSC Adv.* 6 (2016) 60355–60371. <https://doi.org/10.1039/C6RA11334F>.
- [3] A.K. Sood, R.K. Ohdar, S.S. Mahapatra, Parametric appraisal of mechanical property of fused deposition modelling processed parts, *Mater. Des.* 31 (2010) 287–295. <https://doi.org/10.1016/j.matdes.2009.06.016>.
- [4] S. Ahn, M. Montero, D. Odell, S. Roundy, P.K. Wright, Anisotropic material properties of fused deposition modeling ABS, *Rapid Prototyp. J.* 8 (2002) 248–257. <https://doi.org/10.1108/13552540210441166>.
- [5] A. Kantaros, D. Karalekas, Fiber Bragg grating based investigation of residual strains in ABS parts fabricated by fused deposition modeling process, *Mater. Des.* 50 (2013) 44–50. <https://doi.org/10.1016/j.matdes.2013.02.067>.
- [6] A.R. Torrado, C.M. Shemelya, J.D. English, Y. Lin, R.B. Wicker, D.A. Roberson, Characterizing the effect of additives to ABS on the mechanical property anisotropy of specimens fabricated by material extrusion 3D printing, *Addit. Manuf.* 6 (2015) 16–29. <https://doi.org/10.1016/j.addma.2015.02.001>.
- [7] U. Kalsoom, P.N. Nesterenko, B. Paull, Recent developments in 3D printable composite materials, *RSC Adv.* 6 (2016) 60355–60371. <https://doi.org/10.1039/C6RA11334F>.
- [8] A.C. de Leon, Q. Chen, N.B. Palaganas, J.O. Palaganas, J. Manapat, R.C. Advincula, High performance polymer nanocomposites for additive manufacturing applications, *React. Funct. Polym.* 103 (2016) 141–155. <https://doi.org/10.1016/j.reactfunctpolym.2016.04.010>.
- [9] L.J. Love, V. Kunc, O. Rios, C.E. Duty, A.M. Elliott, B.K. Post, R.J. Smith,

- C.A. Blue, The importance of carbon fiber to polymer additive manufacturing, *J. Mater. Res.* 29 (2014) 1893–1898.  
<https://doi.org/10.1557/jmr.2014.212>.
- [10] R. Matsuzaki, M. Ueda, M. Namiki, T.-K. Jeong, H. Asahara, K. Horiguchi, T. Nakamura, A. Todoroki, Y. Hirano, Three-dimensional printing of continuous-fiber composites by in-nozzle impregnation. Supporting Information, *Sci. Rep.* 6 (2016) 23058. <https://doi.org/10.1038/srep23058>.
- [11] X. Wei, D. Li, W. Jiang, Z. Gu, X. Wang, Z. Zhang, Z. Sun, 3D Printable Graphene Composite, *Sci. Rep.* 5 (2015) 1–7.  
<https://doi.org/10.1038/srep11181>.
- [12] S. Dul, L. Fambri, A. Pegoretti, Fused deposition modelling with ABS-graphene nanocomposites, *Compos. Part A Appl. Sci. Manuf.* 85 (2016) 181–191. <https://doi.org/10.1016/j.compositesa.2016.03.013>.
- [13] G. Postiglione, G. Natale, G. Griffini, M. Levi, S. Turri, Conductive 3D microstructures by direct 3D printing of polymer/carbon nanotube nanocomposites via liquid deposition modeling, *Compos. Part A Appl. Sci. Manuf.* 76 (2015) 110–114.  
<https://doi.org/10.1016/j.compositesa.2015.05.014>.
- [14] B.G. Compton, J.A. Lewis, 3D-printing of lightweight cellular composites, *Adv. Mater.* 26 (2014) 5930–5935.  
<https://doi.org/10.1002/adma.201401804>.
- [15] S. Hwang, E.I. Reyes, K. sik Moon, R.C. Rumpf, N.S. Kim, Thermo-mechanical Characterization of Metal/Polymer Composite Filaments and Printing Parameter Study for Fused Deposition Modeling in the 3D Printing Process, *J. Electron. Mater.* 44 (2015) 771–777.  
<https://doi.org/10.1007/s11664-014-3425-6>.
- [16] D.P. Cole, J.C. Riddick, H.M. Iftekhhar Jaim, K.E. Strawhecker, N.E. Zander, Interfacial mechanical behavior of 3D printed ABS, *J. Appl. Polym. Sci.* 133 (2016) 1–12. <https://doi.org/10.1002/app.43671>.
- [17] Y. Li, H. Shimizu, Improvement in toughness of poly(l-lactide) (PLLA)

- through reactive blending with acrylonitrile-butadiene-styrene copolymer (ABS): Morphology and properties, *Eur. Polym. J.* 45 (2009) 738–746. <https://doi.org/10.1016/j.eurpolymj.2008.12.010>.
- [18] M. Vaezi, H. Seitz, S. Yang, A review on 3D micro-additive manufacturing technologies, *Int. J. Adv. Manuf. Technol.* 67 (2013) 1721–1754. <https://doi.org/10.1007/s00170-012-4605-2>.
- [19] B.N. Turner, R. Strong, S.A. Gold, A review of melt extrusion additive manufacturing processes: I. Process design and modeling, *Rapid Prototyp. J.* 20 (2014) 192–204. <https://doi.org/10.1108/RPJ-01-2013-0012>.
- [20] P.J. Nuñez, A. Rivas, E. García-Plaza, E. Beamud, A. Sanz-Lobera, Dimensional and Surface Texture Characterization in Fused Deposition Modelling (FDM) with ABS plus, *Procedia Eng.* 132 (2015) 856–863. <https://doi.org/10.1016/j.proeng.2015.12.570>.
- [21] J.E. Siegel, M.F. Beemer, S.M. Shepard, Automated non-destructive inspection of Fused Filament Fabrication components using Thermographic Signal Reconstruction, *Addit. Manuf.* 31 (2020) 100923. <https://doi.org/10.1016/j.addma.2019.100923>.
- [22] N.M. DeNardo, Additive manufacturing of carbon-fiber-reinforced thermoplastic composites, 2016. <http://search.proquest.com/docview/1849473099?pq-origsite=gscholar>.
- [23] M. Spoerk, C. Savandaiah, F. Arbeiter, G. Traxler, L. Cardon, C. Holzer, J. Sapkota, Anisotropic properties of oriented short carbon fibre filled polypropylene parts fabricated by extrusion-based additive manufacturing, *Compos. Part A Appl. Sci. Manuf.* 113 (2018) 95–104. <https://doi.org/10.1016/j.compositesa.2018.06.018>.
- [24] H.L. Tekinalp, V. Kunc, G.M. Velez-Garcia, C.E. Duty, L.J. Love, A.K. Naskar, C.A. Blue, S. Ozcan, Highly oriented carbon fiber-polymer composites via additive manufacturing, *Compos. Sci. Technol.* 105 (2014) 144–150. <https://doi.org/10.1016/j.compscitech.2014.10.009>.
- [25] F. Ning, W. Cong, J. Qiu, J. Wei, S. Wang, Additive manufacturing of

- carbon fiber reinforced thermoplastic composites using fused deposition modeling, *Compos. Part B Eng.* 80 (2015) 369–378.  
<https://doi.org/10.1016/j.compositesb.2015.06.013>.
- [26] C.E. Duty, T. Drye, A. Franc, Material Development for Tooling Applications Using Big Area Additive Manufacturing (BAAM), 2015.  
<https://doi.org/10.2172/1209207>.
- [27] A. Kessentini, G.M.S. Ahmed, J. Madiouli, Design optimization and FE analysis of 3D printed carbon PEEK based mono leaf spring, *Micromachines.* 10 (2019). <https://doi.org/10.3390/mi10050279>.
- [28] V. Kunc, Advances and challenges in large scale polymer additive manufacturing, in: 15th SPE Automot. Compos. Conf., 2015.
- [29] C.E. Duty, V. Kunc, B. Compton, B. Post, D. Erdman, R. Smith, R. Lind, P. Lloyd, L. Love, Structure and mechanical behavior of Big Area Additive Manufacturing (BAAM) materials, *Rapid Prototyp. J.* 23 (2017) 181–189.  
<https://doi.org/10.1108/RPJ-12-2015-0183>.
- [30] R.T.L. Ferreira, I.C. Amatte, T.A. Dutra, D. Bürger, Experimental characterization and micrography of 3D printed PLA and PLA reinforced with short carbon fibers, *Compos. Part B Eng.* 124 (2017) 88–100.  
<https://doi.org/10.1016/j.compositesb.2017.05.013>.
- [31] W. Zhang, C. Cotton, J. Sun, D. Heider, B. Gu, B. Sun, T.W. Chou, Interfacial bonding strength of short carbon fiber/acrylonitrile-butadiene-styrene composites fabricated by fused deposition modeling, *Compos. Part B Eng.* 137 (2018) 51–59.  
<https://doi.org/10.1016/j.compositesb.2017.11.018>.
- [32] W. Zhong, F. Li, Z. Zhang, L. Song, Z. Li, Short fiber reinforced composites for fused deposition modeling, *Mater. Sci. Eng. A301.* 301 (2001) 125–130.  
[https://doi.org/10.1016/S0921-5093\(00\)01810-4](https://doi.org/10.1016/S0921-5093(00)01810-4).
- [33] A.R. Torrado Perez, D.A. Roberson, R.B. Wicker, Fracture surface analysis of 3D-printed tensile specimens of novel ABS-based materials, *J. Fail. Anal. Prev.* 14 (2014) 343–353. <https://doi.org/10.1007/s11668-014-9803->

9.

- [34] J. Judson, US Army developing process for using 3D printing at depots and in the field, *Def. News.* (2020).  
<https://www.defensenews.com/land/2020/02/04/us-army-developing-process-for-using-3d-printing-at-depots-and-in-the-field/>.
- [35] T. Jackson, Navy Partnership Goes to New Depths with First 3D-Printed Submersible, *Off. Energy Effic. Renew. Energy.* (2017).  
<https://www.energy.gov/eere/articles/navy-partnership-goes-new-depths-first-3d-printed-submersible>.
- [36] P.K. Jain, P.M. Pandey, P.V.M. Rao, Effect of delay time on part strength in selective laser sintering, *Int. J. Adv. Manuf. Technol.* 43 (2009) 117–126.  
<https://doi.org/10.1007/s00170-008-1682-3>.
- [37] J.T. Cantrell, S. Rohde, D. Damiani, R. Gurnani, L. DiSandro, J. Anton, A. Young, A. Jerez, D. Steinbach, C. Kroese, P.G. Ifju, Experimental characterization of the mechanical properties of 3D-printed ABS and polycarbonate parts, *Rapid Prototyp. J.* 23 (2017) 811–824.  
<https://doi.org/10.1108/RPJ-03-2016-0042>.
- [38] A.R. Torrado, D.A. Roberson, Failure Analysis and Anisotropy Evaluation of 3D-Printed Tensile Test Specimens of Different Geometries and Print Raster Patterns, *J. Fail. Anal. Prev.* 16 (2016) 154–164.  
<https://doi.org/10.1007/s11668-016-0067-4>.
- [39] A.M. Forster, Materials testing standards for additive manufacturing of polymer materials: State of the art and standards applicability, *Addit. Manuf. Mater. Stand. Test. Appl.* (2015).  
<https://doi.org/10.6028/NIST.IR.8059>.
- [40] W.M.H. Verbeeten, M. Lorenzo-Bañuelos, P.J. Arribas-Subiñas, Anisotropic rate-dependent mechanical behavior of Poly(Lactic Acid) processed by Material Extrusion Additive Manufacturing, *Addit. Manuf.* 31 (2020) 100968. <https://doi.org/10.1016/j.addma.2019.100968>.
- [41] M. Mu, C.Y. Ou, J. Wang, Y. Liu, Surface modification of prototypes in

- fused filament fabrication using chemical vapour smoothing, *Addit. Manuf.* 31 (2020). <https://doi.org/10.1016/j.addma.2019.100972>.
- [42] W.H. Ferrell, C.M. Arndt, S. TerMaath, Tensile strength dependence of FFF fiber reinforced ABS on environmental conditioning, *Mech. Adv. Mater. Struct.* 0 (2020). <https://doi.org/10.1080/15376494.2020.1722870>.
- [43] S.N.A.M. Halidi, J. Abdullah, Moisture and humidity effects on the ABS used in Fused Deposition Modeling machine, *Adv. Mater. Res.* 576 (2012) 641–644. <https://doi.org/10.4028/www.scientific.net/AMR.576.641>.
- [44] E. Kim, Y.J. Shin, S.H. Ahn, The effects of moisture and temperature on the mechanical properties of additive manufacturing components: Fused deposition modeling, *Rapid Prototyp. J.* 22 (2016) 887–894. <https://doi.org/10.1108/RPJ-08-2015-0095>.
- [45] F. Arbeiter, M. Spoerk, J. Wiener, A. Gosch, G. Pinter, Fracture mechanical characterization and lifetime estimation of near-homogeneous components produced by fused filament fabrication, *Polym. Test.* 66 (2018) 105–113. <https://doi.org/10.1016/j.polymertesting.2018.01.002>.
- [46] D. Young, N. Wetmore, M. Czabaj, Interlayer fracture toughness of additively manufactured unreinforced and carbon-fiber-reinforced acrylonitrile butadiene styrene, *Addit. Manuf.* 22 (2018) 508–515. <https://doi.org/10.1016/j.addma.2018.02.023>.
- [47] N. van de Werken, H. Tekinalp, P. Khanbolouki, S. Ozcan, A. Williams, M. Tehrani, Additively manufactured carbon fiber-reinforced composites: State of the art and perspective, *Addit. Manuf.* 31 (2020) 100962. <https://doi.org/10.1016/j.addma.2019.100962>.
- [48] F. Ning, W. Cong, Y. Hu, H. Wang, Additive manufacturing of carbon fiber-reinforced plastic composites using fused deposition modeling: Effects of process parameters on tensile properties, *J. Compos. Mater.* 51 (2017) 451–462. <https://doi.org/10.1177/0021998316646169>.
- [49] W.H. Ferrell, S. TerMaath, Print Parameter Effects on the Fracture Properties of Fiber Reinforced ABS Composites Fabricated Through Fused

Deposition Modeling, in: AIAA SciTech 2019 Forum, 2019.

<https://doi.org/10.2514/6.2019-0405>.

- [50] C. Pascual-González, M. Iragi, A. Fernández, J.P. Fernández-Blázquez, L. Aretxabaleta, C.S. Lopes, An approach to analyse the factors behind the micromechanical response of 3D-printed composites, *Compos. Part B Eng.* 186 (2020) 107820. <https://doi.org/10.1016/j.compositesb.2020.107820>.
- [51] M.H. Wagner, V.H. Rolón-Garrido, The interchain pressure effect in shear rheology, *Rheol. Acta.* 49 (2010) 459–471. <https://doi.org/10.1007/s00397-009-0427-z>.
- [52] A.Y. Malkin, A. V. Semakov, V.G. Kulichikhin, Modeling macromolecular movement in polymer melts and its relation to nonlinear rheology, *Rheol. Acta.* 50 (2011) 485–489. <https://doi.org/10.1007/s00397-011-0556-z>.
- [53] H.K. Rasmussen, A constitutive analysis of the extensional flows of nearly monodisperse polyisoprene melts, *Polymer (Guildf).* 104 (2016) 251–257. <https://doi.org/10.1016/j.polymer.2016.05.019>.
- [54] M.H. Wagner, E. Narimissa, Q. Huang, On the origin of brittle fracture of entangled polymer solutions and melts, *J. Rheol. (N. Y. N. Y).* 62 (2018) 221–233. <https://doi.org/10.1122/1.4995497>.
- [55] G. Marrucci, F. Greco, G. Ianniruberto, Rheology of polymer melts and concentrated solutions, *Curr. Opin. Colloid Interface Sci.* 4 (1999) 283–287. [https://doi.org/10.1016/S1359-0294\(99\)90002-X](https://doi.org/10.1016/S1359-0294(99)90002-X).
- [56] H.C. Langelaan, A.D. Gotsis, The relaxation of shear and normal stresses of nematic liquid crystalline polymers in squeezing and shear flows, *J. Rheol. (N. Y. N. Y).* 40 (1996) 107–129. <https://doi.org/10.1122/1.550733>.
- [57] M.F. Herman, Linear Viscoelastic Response in the Lateral Diffusion Model for Linear Chain Polymer Melts, *Macromolecules.* 25 (1992) 4931–4936. <https://doi.org/10.1021/ma00045a018>.
- [58] M.L. Becraft, A.B. Metzner, The rheology, fiber orientation, and processing behavior of fiber-filled fluids, *J. Rheol. (N. Y. N. Y).* 36 (1992) 143–174. <https://doi.org/10.1122/1.550359>.

- [59] S. Commereuc, Basic Rheology of Polymer Melts: An Introductory Polymer Science Experiment, *J. Chem. Educ.* 76 (1999) 1528–1532.  
<https://doi.org/10.1021/ed076p1528>.
- [60] K. Hyun, M. Wilhelm, C.O. Klein, K.S. Cho, J.G. Nam, K.H. Ahn, S.J. Lee, R.H. Ewoldt, G.H. McKinley, A review of nonlinear oscillatory shear tests: Analysis and application of large amplitude oscillatory shear (LAOS), *Prog. Polym. Sci.* 36 (2011) 1697–1753.  
<https://doi.org/10.1016/j.progpolymsci.2011.02.002>.
- [61] V. Sharma, G.H. McKinley, An intriguing empirical rule for computing the first normal stress difference from steady shear viscosity data for concentrated polymer solutions and melts, *Rheol. Acta.* 51 (2012) 487–495. <https://doi.org/10.1007/s00397-011-0612-8>.
- [62] J. Qin, S.T. Milner, Tube diameter of oriented and stretched polymer melts, *Macromolecules.* 46 (2013) 1659–1672.  
<https://doi.org/10.1021/ma302095k>.
- [63] T. Sridhar, M. Acharya, D.A. Nguyen, P.K. Bhattacharjee, On the extensional rheology of polymer melts and concentrated solutions, *Macromolecules.* 47 (2014) 379–386. <https://doi.org/10.1021/ma401213r>.
- [64] A.E. Likhtman, M. Ponmurugan, Microscopic definition of polymer entanglements, *Macromolecules.* 47 (2014) 1470–1481.  
<https://doi.org/10.1021/ma4022532>.
- [65] J. Qin, S.T. Milner, Tubes, topology, and polymer entanglement, *Macromolecules.* 47 (2014) 6077–6085.  
<https://doi.org/10.1021/ma500755p>.
- [66] Q. Huang, L. Hengeller, N.J. Alvarez, O. Hassager, Bridging the Gap between Polymer Melts and Solutions in Extensional Rheology, *Macromolecules.* 48 (2015) 4158–4163.  
<https://doi.org/10.1021/acs.macromol.5b00849>.
- [67] M.H. Wagner, E. Narimissa, V.H. Rolón-Garrido, From melt to solution: Scaling relations for concentrated polystyrene solutions, *J. Rheol. (N. Y. N.*



- Y). 59 (2015) 1113–1130. <https://doi.org/10.1122/1.4922795>.
- [68] C. Casavola, A. Cazzato, V. Moramarco, C. Pappalettere, Orthotropic mechanical properties of fused deposition modelling parts described by classical laminate theory, *Mater. Des.* 90 (2016) 453–458. <https://doi.org/10.1016/j.matdes.2015.11.009>.
- [69] W.H. Ferrell, J. Clement, S. TerMaath, Uniaxial Tensile Testing Standardization for the Qualification of Fiber Reinforced Plastics for Fused Filament Fabrication, *Mech. Adv. Mater. Struct.* (2019).
- [70] P.G. de Gennes, Reptation of a Polymer Chain in the Presence of Fixed Obstacles, *J. Chem. Phys.* 55 (1971) 572–579.
- [71] S. Edwards, The statistical mechanics of polymerized material, *Proc. Phys. Soc.* 92 (1967).
- [72] Y.H. Lin, Number of Entanglement Strands per Cubed Tube Diameter, a Fundamental Aspect of Topological Universality in Polymer Viscoelasticity, *Macromolecules.* 20 (1987) 3080–3083. <https://doi.org/10.1021/ma00178a024>.
- [73] T.A. Kavassalis, J. Noolandi, New View of Entanglements in Dense Polymer Systems, *Phys. Rev. Lett.* 59 (1987) 2674–2677. <https://doi.org/10.1103/PhysRevLett.59.2674>.
- [74] L.J. Fetters, D.J. Lohse, D. Richter, T.A. Witten, A. Zirkel, Connection between Polymer Molecular Weight, Density, Chain Dimensions, and Melt Viscoelastic Properties, *Macromolecules.* 27 (1994) 4639–4647. <https://doi.org/10.1021/ma00095a001>.
- [75] S.T. Milner, Predicting the tube diameter in melts and solutions, *Macromolecules.* 38 (2005) 4929–4939. <https://doi.org/10.1021/ma0355507>.
- [76] R.H. Colby, M. Rubinstein, Two-Parameter Scaling for Polymers in 9 Solvents, *Macromolecules.* 23 (1990) 2753–2757. <https://doi.org/10.1021/ma00212a028>.
- [77] Q. Huang, O. Mednova, H.K. Rasmussen, N.J. Alvarez, A.L. Skov, K.

- Almdal, O. Hassager, Concentrated polymer solutions are different from melts: Role of entanglement molecular weight, *Macromolecules*. 46 (2013) 5026–5035. <https://doi.org/10.1021/ma4008434>.
- [78] D.E. Dunstan, The viscosity-radius relationship for concentrated polymer solutions, *Sci. Rep.* 9 (2019) 1–9. <https://doi.org/10.1038/s41598-018-36596-6>.
- [79] R. Everaers, Topological versus rheological entanglement length in primitive-path analysis protocols, tube models, and slip-link models, *Phys. Rev. E - Stat. Nonlinear, Soft Matter Phys.* 86 (2012) 1–5. <https://doi.org/10.1103/PhysRevE.86.022801>.
- [80] R. Everaers, K. Kremer, in *Model Polymer Networks*, 53 (1996) 4–7.
- [81] J. Cao, J. Qin, S.T. Milner, Simulating constraint release by watching a ring cross itself, *Macromolecules*. 47 (2014) 2479–2486. <https://doi.org/10.1021/ma500325z>.
- [82] C.R. Bartels, B. Crist, W.W. Graessley, Self-Diffusion Coefficient in Melts of Linear Polymers: Chain Length and Temperature Dependence for Hydrogenated Polybutadiene, *Macromolecules*. 17 (1984) 2702–2708. <https://doi.org/10.1021/ma00142a045>.
- [83] M. Doi, S. Edwards, *The Theory of Polymer Dynamics*, Clarendon Press, Oxford, 1987. [https://doi.org/10.1016/0377-0257\(87\)85036-x](https://doi.org/10.1016/0377-0257(87)85036-x).
- [84] A. Chremos, C. Jeong, J.F. Douglas, Influence of polymer architectures on diffusion in unentangled polymer melts, *Soft Matter*. 13 (2017) 5778–5784. <https://doi.org/10.1039/c7sm01018d>.
- [85] W. Paul, G.D. Smith, D.Y. Yoon, Static and dynamic properties of a n-C<sub>100</sub>H<sub>202</sub> melt from molecular dynamics simulations, *Macromolecules*. 30 (1997) 7772–7780. <https://doi.org/10.1021/ma971184d>.
- [86] C. Jeong, J.F. Douglas, Mass dependence of the activation enthalpy and entropy of unentangled linear alkane chains, *J. Chem. Phys.* 143 (2015). <https://doi.org/10.1063/1.4932601>.
- [87] A. Chremos, J.F. Douglas, Particle localization and hyperuniformity of

- polymer-grafted nanoparticle materials, *Ann. Phys.* 529 (2017).  
<https://doi.org/10.1002/andp.201600342>.
- [88] Y. Song, Y. Li, W. Song, K. Yee, K.Y. Lee, V.L. Tagarielli, Measurements of the mechanical response of unidirectional 3D-printed PLA, *Mater. Des.* 123 (2017) 154–164. <https://doi.org/10.1016/j.matdes.2017.03.051>.
- [89] W. Kuhn, Über quantitative Deutung der Viskosität und Strömungsdoppelbrechung von Suspensionen, *Kolloid Zeitschrift.* 62 (1933) 269–285.
- [90] P.J. Flory, *Statistical Mechanics of Chain Molecules*, Hanser Publications, New York, 1988.
- [91] P.G. de Gennes, *Scaling Concepts in Polymer Physics*, Cornell University Press, Ithaca, 1979.
- [92] A.E. Likhtman, Single-chain slip-link model of entangled polymers: Simultaneous description of neutron spin-echo, rheology, and diffusion, *Macromolecules.* 38 (2005) 6128–6139.  
<https://doi.org/10.1021/ma050399h>.
- [93] A.E. Likhtman, The tube axis and entanglements in polymer melts, *Soft Matter.* 10 (2014) 1895–1904. <https://doi.org/10.1039/c3sm52575a>.
- [94] D.J. Read, M.E. Shivokhin, A.E. Likhtman, Contour length fluctuations and constraint release in entangled polymers: Slip-spring simulations and their implications for binary blend rheology, *J. Rheol. (N. Y. N. Y).* 62 (2018) 1017–1036. <https://doi.org/10.1122/1.5031072>.
- [95] M.E. Shivokhin, D.J. Read, D. Kouloumasis, R. Kocen, F. Zhuge, C. Bailly, N. Hadjichristidis, A.E. Likhtman, Understanding Effect of Constraint Release Environment on End-to-End Vector Relaxation of Linear Polymer Chains, *Macromolecules.* 50 (2017) 4501–4523.  
<https://doi.org/10.1021/acs.macromol.6b01947>.
- [96] J. Cao, Z. Wang, A.E. Likhtman, Determining Tube Theory Parameters by Slip-Spring Model Simulations of Entangled Star Polymers in Fixed Networks, *Polymers (Basel).* 11 (2019).

<https://doi.org/10.3390/polym11030496>.

- [97] F.C. Campbell, ed., *Fatigue and Fracture: Understanding the Basics*, ASM International, Materials Park, OH, 2012.
- [98] P.A. Withey, Fatigue Failure of the de Havilland comet I, *Eng. Fail. Anal.* 4 (1997) 147–154. [https://doi.org/10.1016/S1350-6307\(97\)00005-8](https://doi.org/10.1016/S1350-6307(97)00005-8).
- [99] A.A. Griffith, The phenomena of rupture and flow in solids, *Philosophical Trans. R. Soc. London. Ser. A, Contain. Pap. a Math. or Phys. Character.* 221 (1921) 163–198. <https://doi.org/10.1098/rsta.1921.0006>.
- [100] G. Irwin, Analysis of stresses and strains near the end of a crack traversing a plate, *J. Appl. Mech.* 24 (1957) 361–364.
- [101] J.R. Rice, A Path Independent Integral and the Approximate Analysis of Strain Concentration by Notches and Cracks, *J. Appl. Mech.* 35 (1968) 379–386. <https://doi.org/10.1115/1.3601206>.
- [102] G.P. Cherepanov, The propagation of cracks in a continuous medium, *J. Appl. Math. Mech.* 31 (1967) 503–512.
- [103] ASTM International, Standard Test Method for Mode I Interlaminar Fracture Toughness of Unidirectional Fiber-Reinforced Polymer Matrix Composites, *Am. Stand. Test. Methods.* 03 (2014) 1–12. <https://doi.org/10.1520/D5528-13.2>.
- [104] ASTM International, Standard Test Methods for Plane-Strain Fracture Toughness and Strain Energy Release Rate of Plastic Materials, *ASTM J.* 99 (2014) 1–9. <https://doi.org/10.1520/D5045-14.priate>.
- [105] T.D. McLouth, J. V. Severino, P.M. Adams, D.N. Patel, R.J. Zaldivar, The impact of print orientation and raster pattern on fracture toughness in additively manufactured ABS, *Addit. Manuf.* 18 (2017) 103–109. <https://doi.org/10.1016/j.addma.2017.09.003>.
- [106] D.R. Moore, J.G. Williams, A. Pavan, *Fracture Mechanics Testing Methods for Polymers, Adhesives and Composites*, 1st ed., Elsevier, 2001.
- [107] K.R. Hart, E.D. Wetzel, Fracture behavior of additively manufactured acrylonitrile butadiene styrene (ABS) materials, *Eng. Fract. Mech.* 177

- (2017) 1–13. <https://doi.org/10.1016/j.engfracmech.2017.03.028>.
- [108] N. Aliheidari, R. Tripuraneni, A. Ameli, S. Nadimpalli, Fracture resistance measurement of fused deposition modeling 3D printed polymers, *Polym. Test.* 60 (2017) 94–101.  
<https://doi.org/10.1016/j.polymertesting.2017.03.016>.
- [109] M. Spoerk, F. Arbeiter, H. Cajner, J. Sapkota, C. Holzer, Parametric optimization of intra- and inter-layer strengths in parts produced by extrusion-based additive manufacturing of poly(lactic acid), *J. Appl. Polym. Sci.* 134 (2017) 1–15. <https://doi.org/10.1002/app.45401>.
- [110] B.J. Lopes, J.R.M. D’Almeida, Initial development and characterization of carbon fiber reinforced ABS for future Additive Manufacturing applications, *Mater. Today Proc.* 8 (2019) 719–730.  
<https://doi.org/10.1016/j.matpr.2019.02.013>.
- [111] K.R. Hart, E.D. Wetzel, Fracture behavior of additively manufactured acrylonitrile butadiene styrene (ABS) materials, *Eng. Fract. Mech.* 177 (2017) 1–13. <https://doi.org/10.1017/CBO9781107415324.004>.
- [112] A. Nycz, V. Kishore, J. Lindahl, C. Duty, C. Carnal, V. Kunc, Controlling substrate temperature with infrared heating to improve mechanical properties of large-scale printed parts, *Addit. Manuf.* 33 (2020) 101068.  
<https://doi.org/10.1016/j.addma.2020.101068>.
- [113] L.J. Love, C. Duty, Cincinnati Big Area Additive Manufacturing (BAAM), Oak Ridge, TN, 2015.  
<https://info.ornl.gov/sites/publications/files/Pub54708.pdf>.
- [114] B.G. Compton, B.K. Post, C.E. Duty, L. Love, V. Kunc, Thermal analysis of additive manufacturing of large-scale thermoplastic polymer composites, *Addit. Manuf.* 17 (2017) 77–86.  
<https://doi.org/10.1016/j.addma.2017.07.006>.
- [115] C. Ajinjeru, V. Kishore, P. Liu, A.A. Hassen, J. Lindahl, V. Kunc, C. Duty, Rheological evaluation of high temperature polymers to identify successful extrusion parameters, *Proc. 27th Annu. Int. Solid Free. Fabr. Symp. Addit.*

Manuf. Conf. (2017) 485–494.

<http://sffsymposium.engr.utexas.edu/sites/default/files/2017/Manuscripts/RheologicalEvaluationofHighTemperaturePolymer.pdf>.

- [116] V. Kunc, V. Kishore, X. Chen, C. Ajinjeru, C. Duty, A.A. Hassen, High Performance Poly(etherketoneketone) (PEKK) Composite Parts Fabricated using Big Area Additive Manufacturing (BAAM) Processes, 2016. <https://info.ornl.gov/sites/publications/files/Pub72094.pdf>.
- [117] C. Ajinjeru, V. Kishore, P. Liu, J. Lindahl, A.A. Hassen, V. Kunc, B. Post, L. Love, C. Duty, Determination of melt processing conditions for high performance amorphous thermoplastics for large format additive manufacturing, *Addit. Manuf.* 21 (2018) 125–132. <https://doi.org/10.1016/j.addma.2018.03.004>.
- [118] C. Ajinjeru, V. Kishore, X. Chen, J. Lindhal, Z. Sudbury, A. Arabi, A. Hassen, V. Kunc, B. Post, L. Love, The influence of rheology on melt processing conditions of amorphous thermoplastics for Big Area Additive Manufacturing (BAAM), in: 27th Annu. Int. Solid Free. Fabr. Symp., Austin, TX, 2016: pp. 754–762.
- [119] V. Kishore, C. Ajinjeru, A. Nycz, B. Post, J. Lindahl, V. Kunc, C. Duty, Infrared preheating to improve interlayer strength of big area additive manufacturing (BAAM) components, *Addit. Manuf.* 14 (2017) 7–12. <https://doi.org/10.1016/j.addma.2016.11.008>.
- [120] K. Chockalingam, N. Jawahar, U. Chandrasekar, K.N. Ramanathan, Establishment of process model for part strength in stereolithography, *J. Mater. Process. Technol.* 208 (2008) 348–365. <https://doi.org/10.1016/j.jmatprotec.2007.12.144>.
- [121] A. Sakly, S. Kenzari, D. Bonina, S. Corbel, V. Fournée, A novel quasicrystal-resin composite for stereolithography, *Mater. Des.* 56 (2014) 280–285. <https://doi.org/10.1016/j.matdes.2013.11.025>.
- [122] I. Shishkovsky, V. Scherbakov, Y. Morozov, Layerwise laser-assisted sintering and some properties of iron oxide core/PEEK shell magnetic

nanocomposites, *Microelectron. Eng.* 146 (2015) 85–91.

<https://doi.org/10.1016/j.mee.2015.04.030>.

[123] A. Bellini, S. Güçeri, Mechanical characterization of parts fabricated using fused deposition modeling, *Rapid Prototyp. J.* 9 (2003) 252–264.

<https://doi.org/10.1108/13552540310489631>.

[124] O.S. Carneiro, A.F. Silva, R. Gomes, Fused deposition modeling with polypropylene, *Mater. Des.* 83 (2015) 768–776.

<https://doi.org/10.1016/j.matdes.2015.06.053>.

[125] H. Klippstein, A. Diaz De Cerio Sanchez, H. Hassanin, Y. Zweiri, L. Seneviratne, Fused Deposition Modeling for Unmanned Aerial Vehicles (UAVs): A Review, *Adv. Eng. Mater.* 20 (2018) 1–17.

<https://doi.org/10.1002/adem.201700552>.

**CHAPTER II**  
**UNIAXIAL TENSILE TESTING STANDARDIZATION FOR THE**  
**QUALIFICATION OF FIBER REINFORCED PLASTICS FOR**  
**FUSED FILAMENT FABRICATION**



A version of this chapter was originally published by William H. Ferrell, Dr. Jason Clement, and Dr. Stephanie C. TerMaath:

William H. Ferrell, Jason Clement, and Stephanie C. TerMaath. “Uniaxial Tensile Testing Standardization for the Qualification of Fiber Reinforced Plastics for Fused Filament Fabrication” *Mechanics of Advanced Materials and Structures* 0 (2019): 1-20.

I, William Ferrell, was the primary author of this with assistance from my Advisor, Dr. Stephanie TerMaath and Dr. Jason Clement who was a Post-Doc at the time who aided in experimentation and set up.

### **Abstract**

Fused filament fabrication (FFF) is a material deposition technique enabling the rapid production of on-demand, customized parts. To support the widespread implementation of FFF into manufacturing supply chains, the qualification of existing and emerging materials for FFF must be standardized, necessitating new and/or modified classification and testing procedures. Current standards do not account for the entire design space capable of FFF technologies. The objective of this investigation is to provide the knowledge needed for development of new standards and practices as demonstrated using the example of the tensile strength of fiber reinforced plastic parts fabricated through FFF.

## Introduction

Traditionally, the manufacturing of complex parts required either the build-up of components through joining methods or the subtractive removal of material from a larger piece through machining. However, in recent years, the development of additive manufacturing (AM) techniques enabled monolithic part fabrication through the progressive layering of material based on a set tool path generated from a computer aided design (CAD) model. One such AM technique is fused filament fabrication (FFF) which builds parts by depositing molten thermoplastics that rapidly cool and hold their shape after the extrusion process. Custom manufacturing, achievable with FFF, creates shorter and closed supply chains, reduced costs, decreased material waste, increased productivity, and production of on-demand parts across many fields.

FFF initially debuted in rapid prototyping for the cost effective fabrication of plastic prototypes and demonstration pieces on site.<sup>1</sup> However, the true benefit of FFF is realized in the production of consumer end parts<sup>1-3</sup>, and FFF has increased in usage and popularity across many industries. From consumer products, medical devices, transportation and energy, to replacement parts for legacy aircraft no longer in production, FFF has already impacted the manufacturing landscape.<sup>1,4</sup> For example, in the medical field, FFF is being used as a tool to develop geometrically accurate surgical models, as well as to provide surgical guides which are critical to test for alignment and guide optimized positioning for stabilizing screws etc.<sup>5,6</sup> Within the transportation field, FFF creates both end user parts and tools, from use in power steering pump manufacturing<sup>7</sup> to thermoforming molds<sup>8</sup>. Within the aerospace field, parts fabricated using FFF are utilized for applications ranging from small aerial vehicles to large spacecraft<sup>9-12</sup>. Some specific examples include: a camera fairing,<sup>13</sup> commercial aircraft interior parts,<sup>14</sup> various spare parts,<sup>15</sup> fixed wing profiles,<sup>16</sup> embedded electronic and current carrying frames for unmanned aerial vehicles,<sup>17,18</sup> air ducts,<sup>19</sup> wall panels,<sup>20</sup> dashboard interfaces,<sup>21</sup>

as well as the vents, housings, camera mounts, door pods, and a front bumper on NASA vehicles.<sup>12,22</sup>

While AM technologies such as FFF are being increasingly used to create new products, material generation remains on the forefront of FFF research despite unacceptable levels of variability within part performance removing these parts and materials from being used in high value applications. The FAA has created an internal memorandum regarding the handling of metallic AM materials for considerations for certification of parts and a separate notice was issued with regards to provide an introduction and awareness to the use of AM components.<sup>23</sup> The latter notice cites “a lack of industry wide standards for AM” as a major challenge, currently.<sup>23</sup> Additionally, NASA,<sup>24</sup> the FDA,<sup>25,26</sup> and Boeing<sup>27</sup> have all released documents to address quality standards and initial technical considerations for metallic AM technologies. These considerations generally include design for AM, process control, post-processing, part testing, inspection, and material and process qualification.<sup>28</sup> Current efforts from Boeing and other industry partners, through the National Institute for Aviation Research (NIAR) at Wichita State, are spearheading a materials collection and evaluation program which is placing emphasis on geometry and alternative methods that more accurately characterize the polymer-AM materials.<sup>27</sup> Recommendations issued by the various agencies will evolve as more information becomes available, making qualification an important research topic across industries as each industry may have specific material qualification requirements and technical considerations. AM requires a more comprehensive review where the customizability of the AM process creates a larger design space to standardize and test, of particular interest is the FFF process with regards to qualification of materials.

FFF has historically been perceived as a “plug and play” technology, in actuality, the quality of FFF parts is highly dependent on multiple factors spanning extrusion settings, print conditions, and layer orientation in addition to inherent

material variability, all of which contribute to a need to change qualification. In order to organize the many aspects of FFF for qualification, three major umbrella areas are present: classification, extrusion, and methodologies. Classification addresses specimen geometry and size, print orientation, and fabrication techniques for consistency in the collection and evaluation of testing data. Extrusion evaluates the various printing parameters that can be controlled in order to adjust the mechanical properties and specimen printability. The Methodologies discussion provides insight into the sequential printing of multiple specimens, the effects of cutting technique, and machine variability. To maximize the potential of FFF, the effects of each factor on mechanical properties must be quantified and controlled for material qualification, and extrusion conditions must be specified along with mechanical properties. Because many of these factors do not apply to traditional materials, current standards and testing protocols do not account for many facets unique to FFF materials<sup>29</sup> and are therefore not suitable for FFF material qualification without significant alterations.<sup>29</sup> Additionally, the effects of specimen geometry on strength, variability, and repeatable failure in the gauge length are more dominant on tensile test results of FFF materials than for traditional materials.<sup>22,29-33</sup>

To adapt to these more multifaceted qualification requirements, standards development organizations such as ASTM International, the International Organization for Standardization (ISO), and the American Society of Mechanical Engineers (ASME) are generating early stage guidelines and standards for AM, and the objective of this paper is to inform this development. Prior and ongoing efforts to address AM specific procedures include the current standard for ASTM reporting in additive manufacturing, ASTM F2971-13,<sup>34</sup> and naming, ISO/ASTM 52900 (F2792-12), where ASTM F2792-12 has subsequently been withdrawn and ISO 52900 is under review. ASTM F2971-13 is not widely cited in literature, likely due to vague reporting requirements for specimen fabrication and a lack of inclusion of all available orientations and naming achievable through FFF.<sup>35</sup> The

work presented in this paper should inform FFF operators of controllable process parameters needed in reporting, both processing and post processing, and of a unified naming convention capable of providing specimens that could be more readily compared to one another. The focus on classification, extrusion, and methodologies within the tensile testing of FFF materials should guide the industry standardization and facilitate effective qualification procedures for FFF materials.

This paper summarizes some of the important standardization limitations associated with using currently available standards for polymer AM, specifically FFF with a focus on tensile strength. Technical considerations aiming to support future standards development, with a focus on qualification of FFF materials, are discussed based on original testing data and supplemented with literature. These technical considerations are broken down into orientation, extrusion, and methodologies and the major findings are discussed and concluded with research recommendations provided.

## **Materials and Methods**

To supplement knowledge compiled through an extensive literature review, experimental testing of chopped fiber reinforced acrylonitrile-butadiene-styrene (CF-ABS) was performed to collect data to fill in knowledge gaps and to explore classification and testing issues unique to FFF. Testing was conducted as needed using a one factor at a time approach to isolate and evaluate print orientation, specimen geometry, specimen preparation, and extrusion effects on tensile strength. CF-ABS was chosen as a commonly used material due to its thermal resistance, toughness, and rigidity, as provided by the acrylonitrile, the butadiene, and the styrene respectively, resulting in an advantageous material for structural use in engineering design.<sup>36,37</sup> The addition of carbon fiber to the system provides increased heat transfer due to the thermal conductivity of the fibers, as well as mechanical reinforcement for strength.<sup>11</sup>

Dogbone shaped specimens were extruded from 3DXTech ABS filament with 15 wt.% CF on Lulzbot Taz 6 printers (unless as noted for the machine variability study) operating through Repetier Host using the open source slicer, Slic3r. Specimens were printed through a 0.4mm hardened steel nozzle using the set of baseline parameters provided in **Table 3**. These baseline parameters were chosen based on median values for the printer settings and the recommended material extrusion settings of the CF-ABS. Parameter values were varied from the baseline throughout this testing program to evaluate parameter effects, as noted for variability studies. Sets of 10 specimens were tested for each configuration or variable being studied.

Tensile testing was performed using an MTS Criterion 45 load frame with a 10kN load cell in accordance with the ASTM D638-14 testing standard which outlines the tensile testing procedure for obtaining the strength and stiffness of plastic materials.<sup>38</sup> This standard recognizes the variance of tensile properties of plastics and plastic behavior with testing speed. Applicability of this standard is discussed along with testing results.

**Table 3** Baseline print parameters and testing ranges

| <i>Conditions</i>  | <i>Baseline (BSLN)</i> | <i>Settings</i> | <i>Parameter Studies</i> |
|--------------------|------------------------|-----------------|--------------------------|
| Nozzle Temperature | 232°C                  |                 | 220°C, 245°C             |
| Build Temperature  | 110°C                  | Platform        | 100°C, 120°C             |
| Bead Height        | 0.2 mm                 |                 | 0.15 mm, 0.25 mm         |
| Fan Speed          | 75%                    |                 | 0%- 100%                 |

## Results


Results are grouped and discussed in terms of the three qualification requirements categories: Classification, Extrusion, and Methodologies.

### ***Classification***

The objective of detailed classification standards is to ensure testing repeatability and the consistent reporting of mechanical properties relative to the new complexities introduced by the FFF manufacturing process. Specimen configuration (geometry and size), print orientation, and fabrication technique all affect the tensile properties of FFF parts and must be considered in material qualification.

#### *Specimen Configuration*

Specimen configuration describes specimen size and geometry. ASTM D638-14 is the testing standard commonly applied for the determination of the tensile properties for traditionally manufactured reinforced plastic and has been investigated in the literature for applicability to FFF specimens. This standard specifies five different sizes and geometries of dogbone shaped specimens with varying cross-sectional area and gauge length as well as fillet radii and overall size (***Figure 15***).

|               | Gauge Length (mm) | Gauge Width (mm) |  |
|---------------|-------------------|------------------|--|
| ASTM Type I   | 50                | 13               |  |
| ASTM Type II  | 50                | 6                |  |
| ASTM Type III | 50                | 19               |  |
| ASTM Type IV  | 25                | 6                |  |
| ASTM Type V   | 7.62              | 3.18             |  |

**Figure 15** Specimen size difference between type I, type II, type III, type IV, and type V (from left to right respectively) of the ASTM D638-14 standard

Type I and type V specimens aligned with the two primary orientations (along the bead and perpendicular to the bead-to-bead interface) are the most commonly used configurations in the literature for determining tensile properties of FFF materials <sup>11,31,45–47,32,38–44</sup>. A majority of literature studies chose one type and then performed all testing on the selected configuration, and did not performing a comparison of specimen types, particularly when investigating the effects of additives or new materials. Initial comparisons and critiques of specimen type start with Ahn et al. <sup>44</sup> who concluded that type I specimens, fabricated from ABS in a way that orients the beads with the load direction, caused premature failure along the fillet radius due to the raster pattern, outside of the gauge length. Meanwhile, Prater et al. found that testing with type IV specimens, also fabricated using ABS but in a way that orients the beads in a 45° angle, resulted in similar premature failure in the fillet radius.<sup>22</sup> The narrow-gauge section and the more pronounced fillet were given as potential reasons for the failure outside of the gauge length.



Torrado et al.<sup>41</sup> provided one of the more extensive studies in the literature that evaluates the two primary material orientations as well as specimen configuration effects on tensile properties. Their work however did not include the type III specimens due to limitations of printer space, and they chose not to evaluate the type II configuration due to the similar gauge section shape relative to the type IV and type V configurations. There were major differences in the reported strength of the type I, type IV, and type V. However, the type V specimen was tested at a substantially different strain rate which could cause a difference in the obtained ultimate tensile strength. A major conclusion from this work was the benefit of using the type V specimen for large throughput of test specimens and type V also demonstrated similar ultimate tensile strengths between the 3 orientations printed, which was not observed in the other specimens.

Further investigation of specimen geometries has been recommended across literature sources. To contribute additional data to this knowledge base, an exploratory evaluation of the five ASTM specimens was performed to investigate any significant strength and repeatability differences caused by specimen configuration. Because the bead-to-bead interface was consistently identified as the weakest component across a range of reinforced FFF materials<sup>39,42,55,56,45,48-54</sup>, and thus the limiting orientation for tensile strength, ten specimens with beads layered transverse to the load were fabricated for each of the five ASTM types for tensile testing. Specimens were printed individually and directly onto the bed.

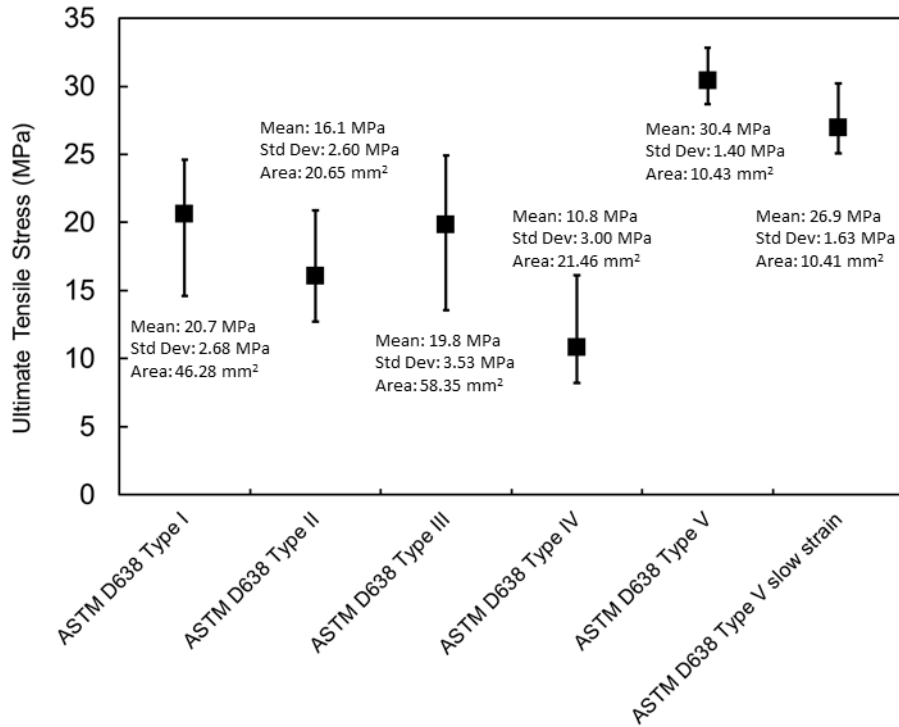


**Figure 16** Ultimate tensile strength results obtained from ASTM D638-14 Type I, II, III, IV, and V specimen types printed individually and directly onto the bed. Mean, standard deviation, and cross-sectional area are reported for each specimen type.

The ultimate tensile strength variation between the five specimen types was quite substantial, (**Figure 16**), further demonstrating the need for standardization of specimen configuration. In terms of repeatability for each specimen type: 9 out of 10 tests failed in the gauge length in the testing of the type I, 10 out of 10 (type II), 10 out of 10 (type III), 8 out of 10 (type IV), and 6 out of 10 (type V). The type IV specimens produced high variability in time to break, raising concerns that the narrow-gauge section and pronounced fillet radius did result in the increase in number of failed tests. While the type II and type IV specimens have vastly different fillet radii and overall length, they have comparable gauge widths; yet the type II specimens did not suffer from the same variability in time to break and specimen

failure outside the gauge length as the type IV specimens, likely due to the more gradual fillet and longer gauge section, minimizing stress concentrations caused by raster effects at the fillet. When taking into consideration the specimen gauge length and width, the smaller type IV and type V specimens produced the highest variability in time to break and the greatest number of invalid test results. Due to the smaller size, any stress concentrations induced by the deposition process have a larger impact on the variability. When qualifying a material based on the minimum allowable load, the consistency of the type I specimen when loading the interface may be useful.

A one-way analysis of variance test (ANOVA) was performed on the means of the ultimate strengths for the five different specimen types to determine if the differences were statistically significant. ANOVA in the most basic form is a statistical test to determine if the means of several population groups are statistically equal.<sup>57</sup> This comparison is determined by computing a number of means and variances, then taking the ratio of two variances and comparing it to a handbook value to determine the statistical significance. An F-test is performed which is the variance between populations divided by the variance within populations. Comparing the calculated F-value to the handbook F-critical value allows the operator to accept ( $F < F_{critical}$ ) or reject ( $F \geq F_{critical}$ ) the null hypothesis.

As shown in **Table 4** One way ANOVA analysis of ultimate tensile stress for the five ASTM Types, the F-value is greater than F-crit which means that the variance in the means is significant. The ANOVA test does not quantify the contribution of each mean to the difference, it only signifies that there is a statistically significant difference. A t-Test is therefore performed between each of the five specimen types in order to test if the means were statistically equal, where equality includes natural variability within the populations. A t-Test is performed by comparing the means of two populations rather than a group of populations, due to the limitation of the ANOVA test to tell which of the populations contributes to the variance. It was determined that the difference in every combination except type I compared to type III, had significantly different mean values.

**Table 4** One way ANOVA analysis of ultimate tensile stress for the five ASTM Types

**SUMMARY**

| <i>Groups</i> | <i>Count</i> | <i>Mean</i> | <i>Variance</i> |
|---------------|--------------|-------------|-----------------|
| Type I        | 10           | 20.65       | 7.20            |
| Type II       | 10           | 16.08       | 6.74            |
| Type III      | 10           | 19.84       | 12.48           |
| Type IV       | 10           | 10.82       | 9.02            |
| Type V        | 10           | 26.61       | 1.93            |

**ANOVA**

| <i>Source of Variation</i> | <i>SS</i> | <i>df</i> | <i>MS</i> | <i>F-value</i> | <i>P-value</i> | <i>F crit</i> |
|----------------------------|-----------|-----------|-----------|----------------|----------------|---------------|
| Between Groups             | 1364.69   | 4         | 341.17    | 45.61          | 2.8E-15        | 2.58          |
| Within Groups              | 336.57    | 45        | 7.47      |                |                |               |
| Total                      | 1701.26   | 49        |           |                |                |               |

Type I and type III T-test demonstrated that the observed difference between the mean ultimate tensile stresses is not conclusive enough to say that the difference is significant, as demonstrated by the t State existing in the range from positive to negative of the t Critical two-tail values in **Table 5**. The type I and type III both have very similar shapes and only truly differ in the overall size of the specimen. The gauge widths are significantly larger than the type II, type IV, and type V specimens and therefore a wider gauge section may be necessary to achieve uniform material properties. The type II, type IV, and type V had a different shape compared as with the type I and type III which also contributed to significantly different mean ultimate tensile strengths for these specimen types.

**Table 5** T-Test of type I and type III show difference in means is not conclusively significant

|                              | <i>Variable</i><br>1 | <i>Variable</i><br>2 |
|------------------------------|----------------------|----------------------|
| Mean                         | 20.65                | 19.84                |
| Variance                     | 7.20                 | 12.48                |
| Observations                 | 10                   | 10                   |
| Pooled Variance              | 9.84                 |                      |
| Hypothesized Mean Difference | 0                    |                      |
| df                           | 18                   |                      |
| <b>t Stat</b>                | <b>0.57</b>          |                      |
| P(T<=t) one-tail             | 0.28                 |                      |
| t Critical one-tail          | 1.73                 |                      |
| P(T<=t) two-tail             | 0.57                 |                      |
| <b>t Critical two-tail</b>   | <b>2.10</b>          |                      |

These testing results do not agree with those obtained by Torrado et. al., potentially due to the differences in strain rates between the two datasets. Further exploration in the testing speed, or strain rate, was therefore performed. The initial tests were performed at an extension rate of 1 mm/min. With smaller test specimens, ASTM type IV and V, the time to break was significantly shorter than for types I-III. The apparent increase in strength associated with the smaller type V specimens and higher likelihood of an invalid test, may be due to an inappropriate test speed for the specimen size. Testing speed was therefore investigated on the type V using a lower 0.2 mm/min test speed on an additional set of 10 specimens, resulting in a decreased mean for ultimate tensile strength more consistent with the values for types I-III seen in **Figure 16**. The variable time to specimen failure in both the type IV and type V specimens and the decrease in ultimate tensile strength when testing at slower speeds provides evidence for an

evaluation of appropriate test speed relative the specimen configuration to modify current standards for FFF material testing.

While also a concern with composite laminate specimens<sup>22</sup>, the designation of fillet radius may prove even more important for the specimen configuration of FFF materials relative to their traditional counterparts, due to the nearly unlimited options of raster patterns available for specimen fabrication. Raster patterns, most influentially at the fillet radius, can create weak points in the specimen causing failure outside of the gauge length, in addition to affecting the volume of air voids and interface area.<sup>30,41,44,51</sup> The raster pattern is specified and controlled before printing and therefore specimen geometry can be designed to maximize repeatability for varying specimen size and orientation.

In all orientations, there are Poisson effects that load the bead to bead interface in tension during the tensile testing. In the case of most homogeneous materials, when a sample is pulled in tension the material extends in the test direction and contracts in the transverse direction. In the case of FFF materials, each bead, in part, acts as a separate material. When undergoing tensile stress, the interface of the beads is loaded as each of the beads across the specimen contract. As the loads distributed to the interface reach the ultimate tensile load of the bead to bead interface, large variations begin to occur in the load-displacement curves, seen in **Figure 17**. When analyzing the fracture surface, bead interface delamination was common in specimens loaded along the beads, demonstrating failure at the interface is still a dominant failure mechanism within FFF parts and test specimens for all orientations.

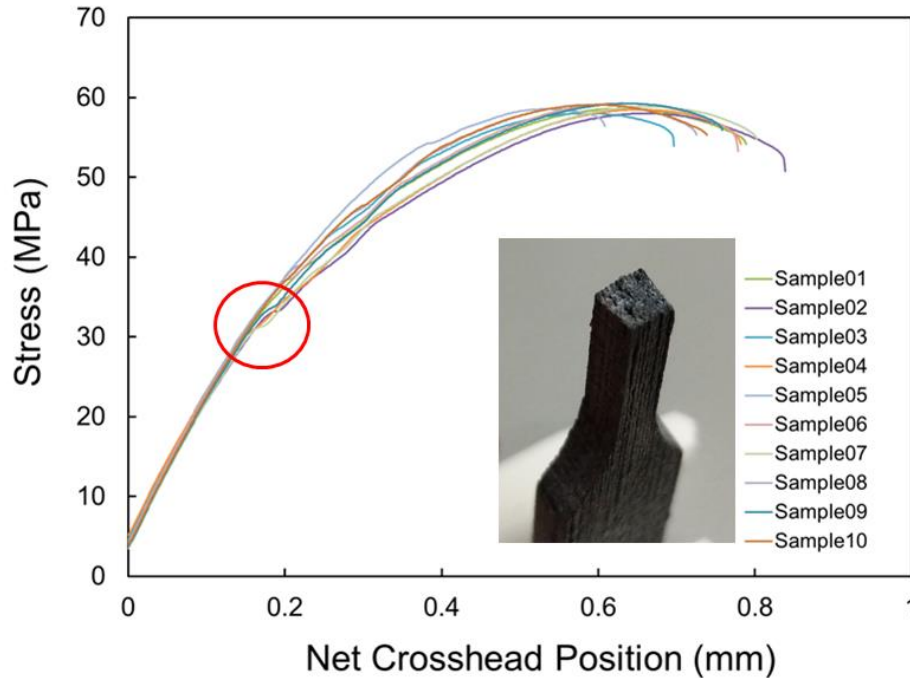


**Figure 17** Bead-to-bead interface failure present in orientations where the bead is aligned in the load direction

### *Orientation*

For traditionally manufactured continuous fiber reinforced plastics, orientation of mechanical properties is typically aligned relative to the reinforcement. Chopped fiber reinforced composites, traditionally manufactured, have high levels of anisotropy that do not exist within the extrudate in FFF, making FFF advantageous with regards to fiber alignment.<sup>58-60</sup> However, with FFF, the control of raster patterns and build direction provides tremendous potential for the manufacture of customized parts but results in many new considerations in defining mechanical property orientation. When a model is uploaded into a printer control software, such as RepetierHost, a slicing software is used to take the stereolithography file (.stl) and create a G-Code, the numerical programming code for automated machine tools that controls build pattern and path. Part placement in the software

and the user selected slicer code affects the raster pattern and build orientation, such that these user choices can result in significant print variations, limiting FFF as a true “plug and play” technology. Both the build direction on the platform and the raster angle affect the mechanical properties of FFF specimens and must be consistently designated along with the corresponding tensile property values.

In addition to consistent designation of specimen orientation, the method of obtaining the specimen must also be considered for classification. Specimens printed individually are fabricated by directly depositing material in the end form shape onto the bed, substantially reducing the time between layers as compared to plaque prints. Due to the improved localized heating within the specimen and the reduced layer times, the strength of the specimen is improved as compared to plaque prints. The farther the nozzle and material deposition locations move from the heated bed, the more the tensile strength is dependent on the layer time and surface area.<sup>61–63</sup> To better simulate actual larger-scale print conditions, the effects of increased layer time must be included in mechanical properties for qualification. Therefore, the specification of specimen fabrication is important for qualification where individual prints should be tested for specific applications, such as small parts, and plaque prints are more appropriate for larger parts to more realistically represent extrusion conditions.

The effects of raster pattern, build path, and the resulting infill on tensile strength have been discussed in the literature.<sup>40,45,64</sup> Raster angle is a controllable process parameter that has been shown to impact both the modulus and strength of the specimen. Numerous studies have used orientations and raster angles of 0° (along the bead and loading the interface in shear), 45°/-45°, 0°/90°, and 90° (perpendicular to the bead and loading the interface in tension) to investigate these effects.<sup>32,44,45,65</sup> Cole et al. [37] determined that specimens built horizontal and on their side with a raster orientation of 0° were the strongest and those at 90° were the weakest. 0°-90° cross hatched specimens demonstrated a mean strength between 0° and 90° on the prints that were printed on their side and horizontally. However, the 0°-90° did not outperform the 45°/45° specimens. Sood et al.<sup>64</sup>



concluded that zero air gap will improve diffusion between adjacent layers but could decrease the heat dissipation as well as total bonding area. They also correlated the raster to stress accumulation, where long rasters increase stress along the direction of deposition and thick rasters result in stress accumulation along the width of the part. Ning et al.<sup>32</sup> concluded that the 0°/90° raster angle produced higher tensile strength, young's modulus, and yield strength, when compared to 45°/-45° raster, contradicting the results of Cole et al.. Additionally, the 45°/-45° raster pattern had the highest toughness and ductility, produced tighter distributions of each of these properties, and exhibited poor interfacial adhesion between the matrix and the carbon fibers, leading to pull out as shown on Scanning Electron Microscope (SEM) images. On the contrary, the carbon fibers took the load in the 0°/90° raster configuration. Es-Said et al.<sup>45</sup> also found that 0° orientation followed by the 45° orientations were the strongest by ultimate and yield strengths for specimens fabricated with a single raster angle.

Rodriguez et al.<sup>66</sup> showed a 11% to 37% reduction in the modulus of ABS materials in FFF when comparing the various raster angles to monofilament tests. They also found that changes in the polymer orientation occurring during the fused deposition manufacturing process affects the mechanical properties and influences the effective moduli. In general, researchers have determined that parts were the strongest when the deposited beads were aligned with the loading direction.<sup>44,67</sup> In this orientation, the maximum stress is applied along the polymer chains rather than at the interface between beads leading to the conclusion that the interbead strength is less than the intrabead strength.

To present a consistent comparison, individual and plaque fabrication specimens were fabricated and tested in orientations along the beads (00+00) and perpendicular to the beads (90+00). The results presented in **Figure 18** confirm the conclusions of other researchers that specimens loaded along the bead are stronger than those loaded perpendicular to the interface. The results also clearly demonstrate the significant variation in the strength and elongation of a specimen cut from a plaque versus an individual print.

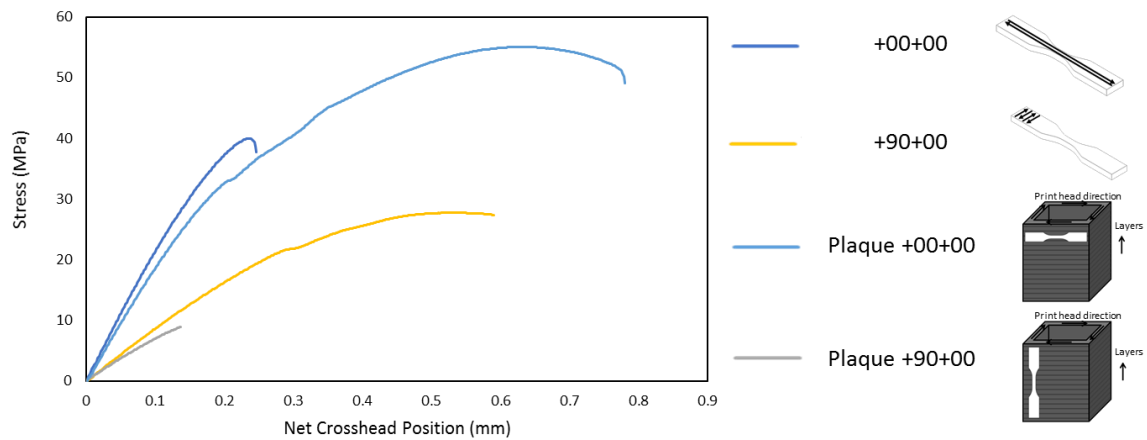


**Figure 18** Comparison of plaque printed specimens and individual specimens, loaded both along the beads (+00+00) and perpendicular to the beads (+90+00)

### *Naming Convention*

As there are multiple ways to obtain a specimen with identical raster angle and that visibly appear the same but vary in the bed orientation, it is essential to uniquely designate orientation according to both raster angle and build path. When defining mechanical property orientation, the current applicable ASTM 52921 standard does not include designation of the raster angle or build path. Furthermore, the inconsistent naming of specimens in the literature <sup>39,55,63,68,69</sup>, typically based on either the raster angle or the build direction with each defined by differing reference planes, prohibits direct comparison of test results. A consistent naming convention that includes both the principal direction of the material deposition path and the raster angle is essential to provide a direct comparison of strength and to designate mechanical properties for qualification and design.

Such a naming convention is shown in **Figure 19** for individual prints (plaque prints would have the designation “plaque” in front of the number as in **Figure 18**). The orientation of the principal axis along the length of a specimen relative to a global coordinate system on the platform (X-Y) is the first component of the name ( $\pm\theta$ ). The raster angle measured relative to the principal axis using a local coordinate system ( $x-y$ ) designated as  $\pm\alpha$  follows. To account for prints with the principal axis in the Z-direction, a “Z” is added before the  $\pm\theta\pm\alpha$  designation. For cases where a Z print is built concentrically, a ZC designation is used followed only by  $\pm\theta$ . For example, the specimen on the left of **Figure 20** is deposited in the Z direction with its principal axis oriented  $+20^\circ$  relative to the platform and has a raster angle of  $+00^\circ$ . Therefore, it is designated as Z+20+00. The specimen on the right is deposited with its principal axis oriented at  $-45^\circ$  relative to the platform and the raster pattern again perpendicular to the length and is named -45+45.

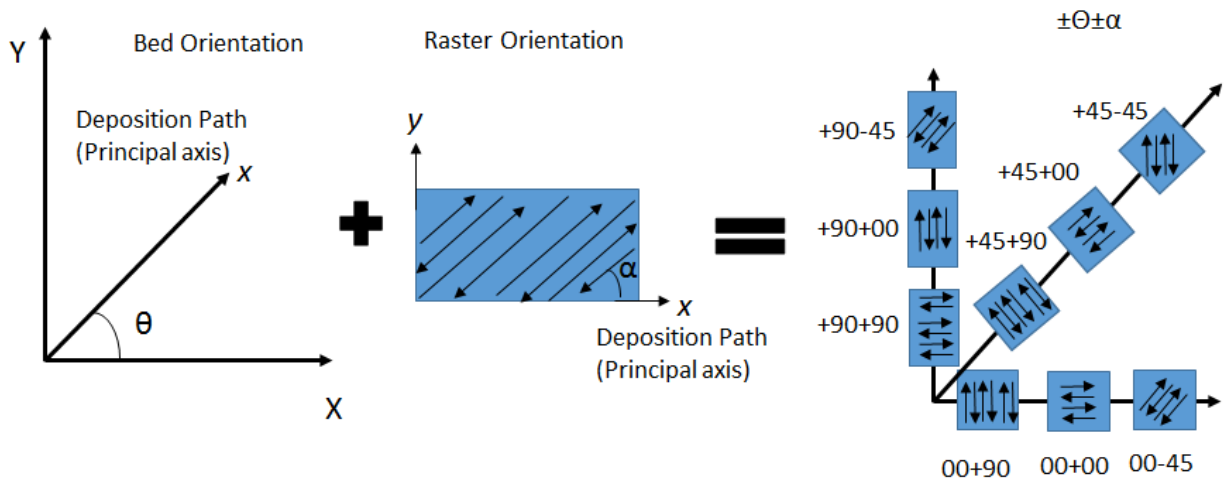


**Figure 19** The naming convention is based on the bed orientation in which the part is deposited along a primary axis oriented as  $\theta$  and raster orientation  $\alpha$  relative to a local axis with  $x$  aligned with the principal axis.

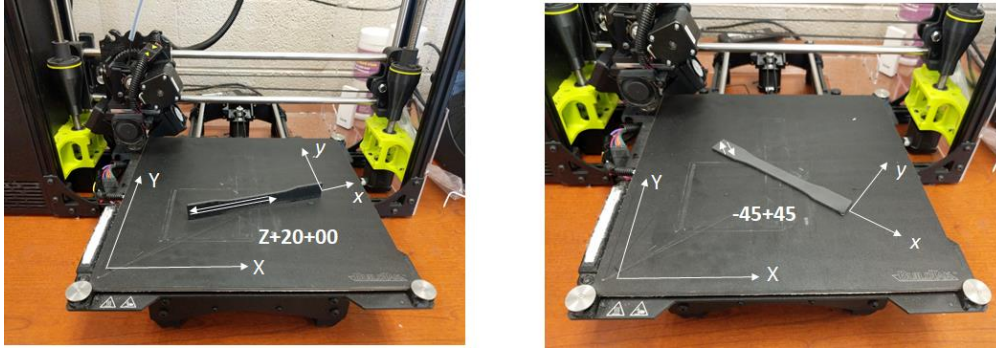


**Figure 20** Examples of the naming convention for a Z print (left) and an in-plane print (right)

To demonstrate the necessity of designating the bed orientation, testing was performed to compare individual prints in the +00+90, +90+90, and +45+90 configurations. All specimens appear identical, but different motors in the printer will be engaged for each, potentially affecting mechanical properties. In addition to the strength differences shown in **Figure 21**, differences in repeatability for a given specimen configuration were also noted (**Figure 22** and **Table 6**). The major takeaway from figure 8, is the demonstration of major repeatability difference, in addition to strength differences. In all subsequent tables, standard deviation will be abbreviated as std dev. The 00+90 specimens consistently failure in the gauge length and all specimens broke completely across the gauge length. The 90+90 were not only the weakest specimens but also had the highest variability in the cross-section dimensions. While these specimens consistently failed in the gauge length, 6 out of the 10 specimens exhibited partial breaks in the gauge section where failure initiated at multiple sites and the ensuing cracks did not link together. The +45+90 showed strength similar to the 00+90 specimens as well as consistent failure in gauge length and only 3 out of the 10 specimens exhibited the partial break patterns seen in the +45+90. These results clearly demonstrate the need to designate both the raster pattern and bed orientation for qualification.

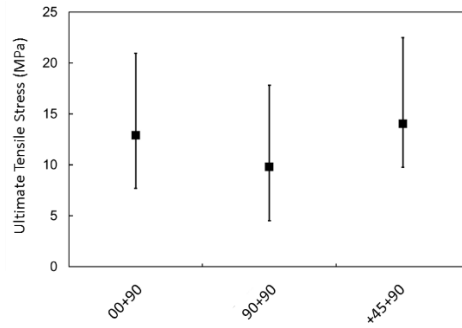


**Figure 21** Comparison of the Ultimate Tensile Stress for specimens that appear identical but were printed in different orientation on the platform.

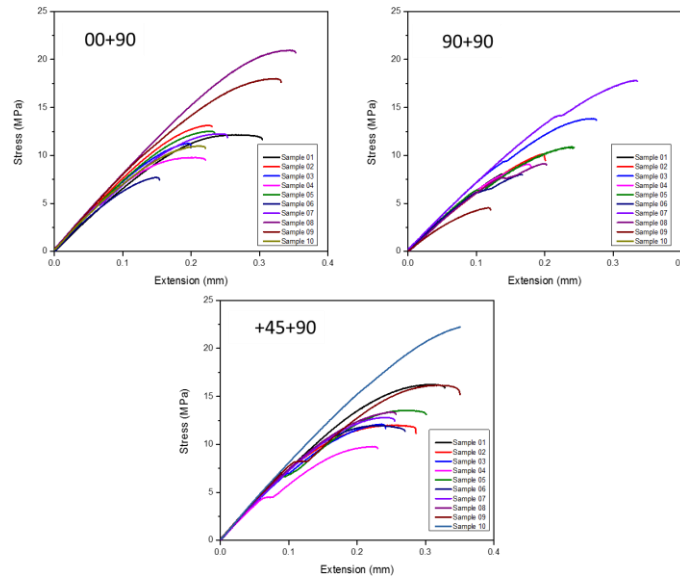


**Figure 22** Comparison of the repeatability for specimens that appear identical but were printed in different orientation on the platform.

**Table 6** Statistics for cross-sectional area and ultimate strength for specimens with identical raster angles but different bed orientations.

| Specimen Orientation | Cross Sectional Area (mm <sup>2</sup> ) |       |        | Ultimate Tensile Strength (MPa) |       |        |
|----------------------|---|-------|--------|---------------------------------|-------|--------|
|                      | 00+90                                   | 90+90 | +45+90 | 00+90                           | 90+90 | +45+90 |
| Mean                 | 11.97                                   | 11.63 | 11.96  | 12.87                           | 9.77  | 14.03  |
| Min                  | 11.73                                   | 10.89 | 11.83  | 7.69                            | 4.53  | 9.76   |
| Max                  | 12.39                                   | 12.35 | 12.18  | 20.95                           | 17.82 | 22.48  |
| Std Dev              | 0.18                                    | 0.53  | 0.12   | 3.88                            | 3.80  | 3.55   |

### ***Extrusion***

In addition to assigning a classification designation to specimens, standardized reporting of print conditions is also essential for qualification due to the significant effects of extrusion control settings on the mechanical properties of the printed product<sup>43,46,63,64,70–72</sup>. Thermal profile variation, dictated by print parameters including, but not limited to, nozzle temperature, print speed, extrusion rate, bed temperature, fan speed, bead height, and bead overlap, impacts the reputation, formation of mechanically crosslinked material, of polymer chains across beads which is a primary contributor to the interfacial strength.<sup>63,73,74</sup> The effects of several of these key parameters (fan speed, nozzle temperature, platform temperature, and bead height) were investigated through experimental testing and compared to results in the literature when available.

### ***Fan Speed***

Depending on the printer make and model, fans are pointed at the nozzle during extrusion to provide material cooling which increases the dimensional accuracy of the printer and results in parts that are more cosmetically appealing. By introducing

rapid cooling, the amount of sagging or expansion of the material is reduced. The test results comparing the ultimate tensile load of specimens fabricated at varying fan speeds are shown in **Figure 23**. Increased fan speed, comparing fans completely turned off 0% to a low speed of 25%, results in a reduction in ultimate tensile stress by 1 MPa and a decrease in the elongation at break (from 0.41 mm to 0.33 mm) due to a reduction in plastic deformation. Negligible amount of variation was observed in yield strength (a difference of 0.12 MPa which is less than 1%).

As fan speed increases beyond 25%, rapid reduction in the ultimate tensile load and the increased onset of brittle failure is evident, suggesting reduced interlayer adhesion. The longer a polymer remains above the  $T_g$ , the more time the polymer chains will have to reptate into a thermodynamically favorable state. Increasing fan speed decreases the amount of time polymer chains spend above the  $T_g$  and thus inhibits the amount of reptation between layers. Additionally, specimens fabricated at increased fan speeds showed significant signs of warping and reduced number of successful prints and tests, as demonstrated in **Figure 24**. Warping is the physical manifestation of uneven cooling rates, where internal cooling rates significantly lag external cooling rates.<sup>70,73</sup> At fan speeds of 50% and above, roughly only a quarter of prints resulted in valid tests with failures in the gauge length. As all specimens fabricated at the higher speeds exhibited some specimen warping, the validity of all results is questionable given the induced bending moments during testing.

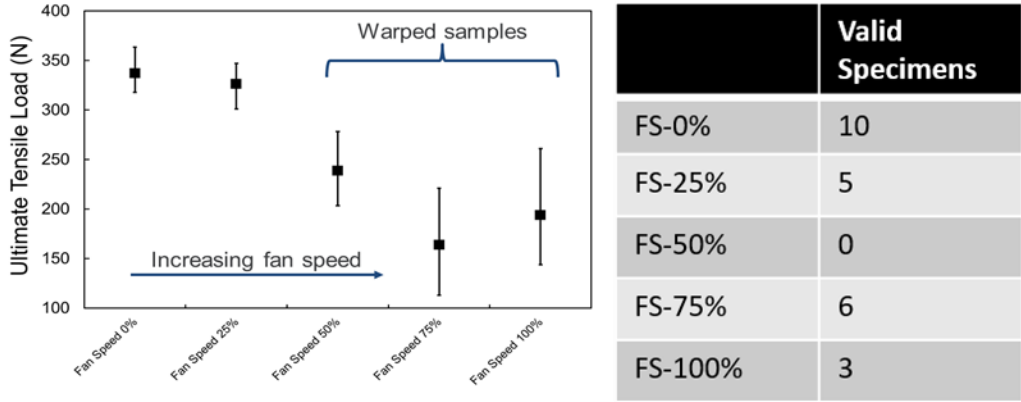


**Figure 23** Increasing fan speed decreases the ultimate tensile load and increases the variability because of warping.

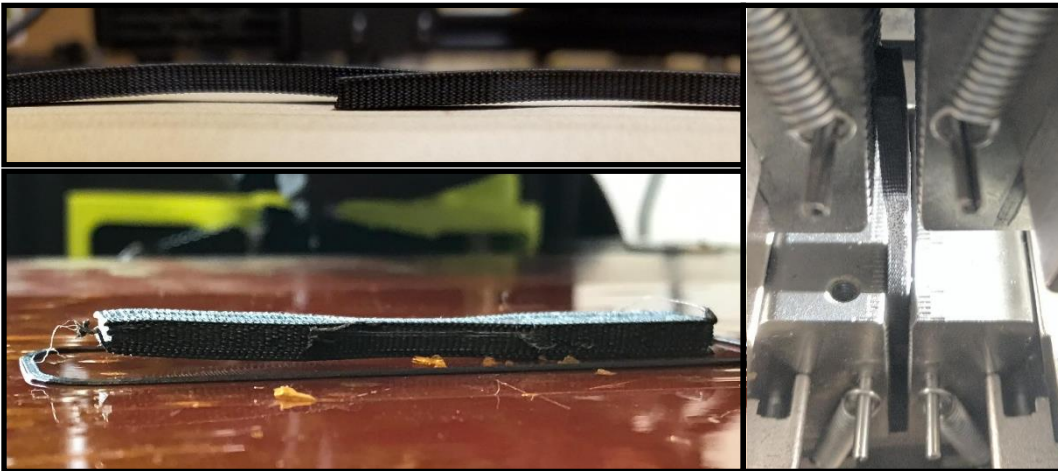


**Figure 24** Visual effects of warping and the subsequent effect in the tensile grips. The resulting bending moment in the middle of the gauge length causes significant deviation from uniaxial tension loading conditions creating an invalid test.



## Nozzle Temperature

The extrusion temperature is dominated by the nozzle temperature setting and directly affects the overall polymer chain dynamics. During the printing of thick specimens, the nozzle temperature becomes the primary contributor to the cyclic thermal loading experienced by each layer as the influence of the platform temperature decreases with increasing distance from the print platform. For thin specimens, the nozzle temperature and the bed temperature both affect the thermal profile. As shown in **Figure 25** for the average curves at each temperature, specimens fabricated with a nozzle temperature of 220°C demonstrated reduced strength and failure at less than half the strain than the specimens fabricated at higher temperatures. A higher nozzle temperature, however, is not proportionally related to larger ultimate tensile stress. With increasing nozzle temperature there is initially an increase in ultimate strength followed by a decrease as temperature continues to increase.

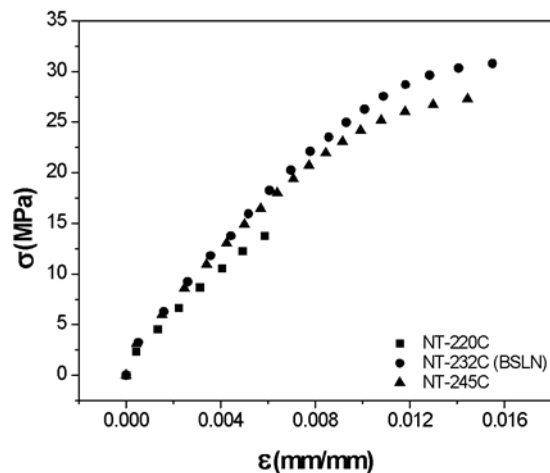


**Figure 25** Stress versus strain curve comparison demonstrating the effect of nozzle temperature on strength

This result is supported in the literature by Ning et. al. for ABS with 5 wt.% CF.<sup>32</sup> They concluded that as nozzle temperature increased, there was an increase in coalescence of the deposited beads. However, there was also a corresponding increase in the porosity of the material, compounding on the increased porosity caused by the addition of the carbon fibers present at all temperatures.<sup>68</sup> The pores within the polymer matrix cause stress concentrations that become crack initiation points under load, counteracting the strength increases due to improved bead coalescence as nozzle temperature increases. As seen in **Figure 26** that shows the stress strain curves for the valid tests, nozzle temperature influences the repeatability of the test results where repeatability is demonstrated as the number of valid test specimens. Despite a lower ultimate tensile strength due to the increased porosity, the uniformity of interlayer mixing produced the most repeatable test results for the highest nozzle temperature of 245°C. Repeatability appears to be dictated predominately by the level of interlayer mixing, or homogeneity, in the gauge length. Therefore, as the nozzle temperature increases, there is an increase in repeatability.

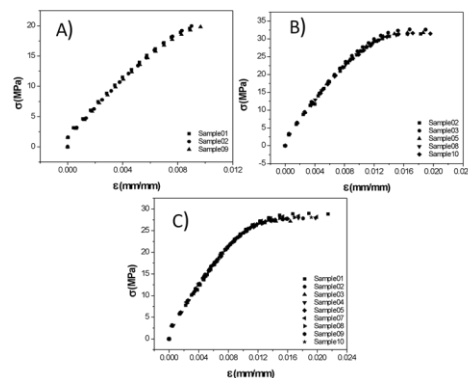


**Figure 26** Stress versus strain plots of valid tests for specimens fabricated with varying nozzle temperature A) 220°C B) 232°C and C) 245°C.

**Table 7** Yield stress and ultimate tensile strength for varying nozzle temperature with the standard deviation reported as a percentage of the mean.

|                         | NT-220°C (N=3) |         | NT-232°C (N=6) |         | NT-245°C (N=9) |         |
|-------------------------|----------------|---------|----------------|---------|----------------|---------|
|                         | Mean           | Std Dev | Mean           | Std Dev | Mean           | Std Dev |
| Yield Stress            | 17.64          | 2.67    | 21.62          | 3.95    | 21.67          | 6.48    |
| Ultimate Tensile Stress | 19.86          | 2.36    | 31.77          | 1.96    | 28.01          | 1.7     |

In **Table 7**, the mean and standard deviation of the yield stress and ultimate tensile stress are presented for the various nozzle temperatures. In addition to higher ultimate strengths, both higher temperatures correlated to a higher yield stress (which was nearly constant between the two higher temperatures). A substantially larger standard deviation of the yield stress was observed for the highest nozzle temperature, while the standard deviation of the ultimate tensile stress slightly decreased as nozzle temperature increased. Reporting of the nozzle temperature is of critical importance to qualification of materials due to its impact on the tensile strength and repeatability.

*Platform Temperature*

The effect of platform temperature on the layer adhesion and mechanical strength was evaluated to quantify the effect of heat permeation through the base layers and into the part. Despite the more favorable environment for layer mixing, the highest bed temperature did not show an increase in strength (**Figure 27**). Thermal cycles, due to the deposition of hot material followed by the rapid cooling in ambient air, create thermal gradients in the extruded material. The reduction in strength due to a higher platform temperature demonstrates that in thin samples,

such as ASTM D638-14 Type V specimen, increased thermal gradients between the bottom layers and top layers creates increased thermal based residual stresses in the material, reducing the tensile strength. <sup>61</sup>

Alternatively, a bed temperature below the  $T_g$  of ABS does not allow for consistent interlaminar adhesion. Maintaining a bed temperature within a few degrees above the  $T_g$  of ABS provides optimal layer adhesion without creating unfavorable thermal gradients in these thin samples. In addition, higher platform temperature resulted in an increase in the variability of both the yield stress and the ultimate tensile stress as shown in **Table 8**.

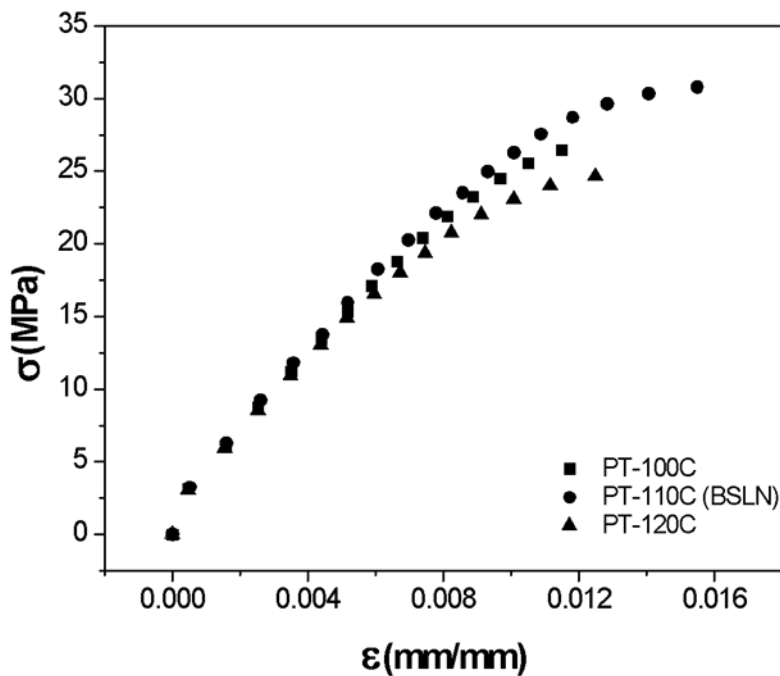


**Figure 27** The effects of platform temperature on tensile strength.

**Table 8** Yield stress and ultimate tensile strength for varying platform temperature with the standard deviation reported as a percentage of the mean.

|                         | <b>PT-100°C (N=8)</b> |         | <b>PT-110°C (BSLN) (N=6)</b> |         | <b>PT-120°C (N=9)</b> |         |
|-------------------------|-----------------------|---------|------------------------------|---------|-----------------------|---------|
|                         | Mean                  | Std Dev | Mean                         | Std Dev | Mean                  | Std Dev |
| Yield Stress            | 21.94                 | 3.92    | 21.62                        | 3.95    | 19.86                 | 6.71    |
| Ultimate Tensile Stress | 27.77                 | 1.35    | 31.77                        | 1.96    | 25.74                 | 5.98    |

The standard deviations for the 100°C and 110°C platform temperatures were comparable for both yield and ultimate tensile stress, however there was a significant increase in ultimate tensile strength for the 110°C (above the 105°C  $T_g$  for ABS). For these thin Type V specimens, the platform temperature below  $T_g$  resulted in a slight decrease in strength as compared to the platform temperature slightly above  $T_g$  that enabled interlayer mixing from the heat provided by the platform. However, for temperatures beyond the  $T_g$ , the first several layers near the platform experience improved interlayer mixing while the upper layers do not benefit from the heat provided by the platform. These variable thermal gradients cause inconsistent mixing, decreasing strength and increasing variability. Providing a platform temperature at approximately the  $T_g$  of the polymer is important for thin specimens, to provide a balance between improved polymer chain dynamics while limiting the thermal gradient effects.

### *Bead Height*

Bead height is defined as the distance between the nozzle and the print surface for the first layer and then between the nozzle and the previously deposited layer for all subsequent layers throughout the duration of the print. This parameter impacts the overall bead shape as well as the forces acting on the material as the

specimen is printed. Smaller bead heights, 0.2mm compared to 0.4 and 0.3 mm, have been shown to increase strength in the crosshatched raster patterns <sup>47</sup>, however in the orientation (layer-to-layer adhesion) that was tested in this study, too small of a bead height, 0.15 mm, reduced the strength (**Figure 28**). Layer-to-layer adhesion is dictated by the natural mixing between layers, where mixing can be limited by the shear stresses associated with the deposition of molten plastic. As the polymer is deposited, it experiences opposing forces from the printer nozzle and the already cooling previous layer. This shear force acts to align the long polymer chains in the direction of deposition, where the applied forces resemble the stretching of the polymer chains, which is known to orient the polymer chains.<sup>75</sup> This phenomena is similar to stretching a rubber band, where the more the rubber band is stretched, the fewer favorable entropic configurations are present. However, in the FFF specimens, the material does not behave like an elastic spring but maintains viscoelastic properties. When the nozzle is sufficiently far away from applying force on the system, the polymer chains do not fully recover and are frozen into a less favorable state by the rapidly decreasing energy from the layer cooling. In the case of bead heights, the smaller bead height results in higher shear stress due to the same volumetric flow being forced into a smaller area. This reduces the overall air void content by pushing more material into the area, but ultimately reduces the number of favorable configurations, therefore decreasing entropy, and ultimately decreasing the layer to layer mixing.

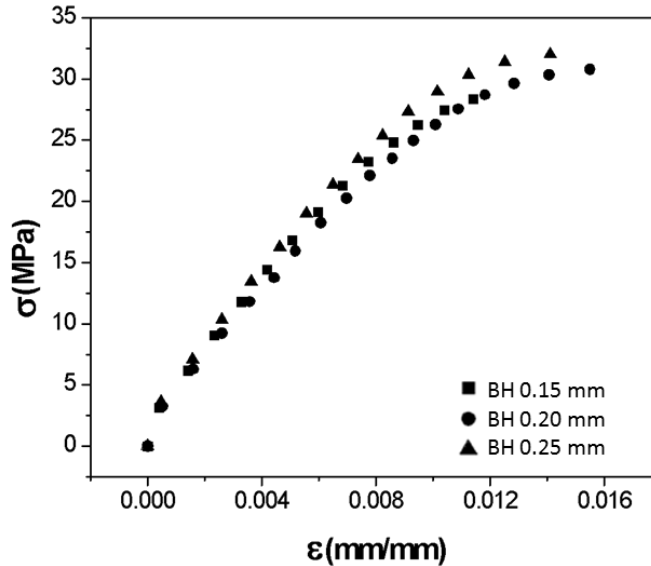


**Figure 28** Bead height alters the natural reptation of polymer chains between layers, where larger bead heights create a better environment for polymer chains to achieve strong layer mixing.

The largest bead height, 0.25mm, produced the highest variability, as a function of standard deviation, for the yield stress (**Table 9**), suggesting that the larger bead height produced a wider range of conditions for the onset of plastic deformation,. However, there was a much lower standard deviation in the ultimate tensile strength compared to the yield stress in the 0.25 mm bead height. This would corroborate the claims of increased natural layer reptation and increased air void content.<sup>32</sup> An increased air void content from bead to bead would increase stresses on the interlayer mixing zones, thus creating a wider range for the onset of plastic deformation, but simultaneously, the increased mixing would provide an increase in the overall strength of these interfaces and reduce the variability.

**Table 9** Yield stress and ultimate tensile strength relative to variation in bead height with the standard deviation reported as a percentage of the mean.

|                         | <b>Bead Height 0.15mm (N=9)</b> |         | <b>Bead Height 0.2mm (BSLN) (N=6)</b> |         | <b>Bead Height 0.25mm (N=8)</b> |         |
|-------------------------|---------------------------------|---------|---------------------------------------|---------|---------------------------------|---------|
|                         | Mean                            | Std Dev | Mean                                  | Std Dev | Mean                            | Std Dev |
| Yield Stress            | 22.83                           | 7.92    | 21.62                                 | 3.95    | 23.7                            | 8.13    |
| Ultimate Tensile Stress | 30.93                           | 3.36    | 31.77                                 | 1.96    | 32.7                            | 2.43    |

### ***Methodologies***

The specific methodologies of sequential printing, cutting technique, and equipment were evaluated to address the variation in mechanical properties due to specimen fabrication methods and the relevance to material qualification.

#### *Sequential Printing*

A larger number of specimens can be printed per unit of time by fabricating multiple specimens on the bed during a single print, referred to as sequential printing. In the case of sequential printing versus printing one specimen at a time (individual printing), the time for heating and cooling the bed, leveling the bed, cleaning the nozzle, or any other set of procedures performed between prints is only required once for the entire set of specimens rather than repeated for each specimen. For example, with the current operational set up of the Lulzbot Taz 6, there is a 7 minute cleaning, auto-leveling, and heating process before the print. Each individual Type V print requires about 8 minutes printing, and another 10 minutes



as the bed cools to reduce the likelihood of bending the hot samples and altering their alignment. Sequential printing eliminates the need to repeat approximately 17 minutes per specimen, saving considerable time when printing a large number of specimens.

While time efficient, the nozzle path during sequential printing can significantly affect tensile strength depending on whether a layer is deposited for all specimens or an entire specimen is completed before moving to the next. When a specimen is printed individually, each layer is deposited immediately upon finishing the previous layer. If a single layer for multiple specimens is deposited, the printer will finish the first layer of the first specimen and then proceed to the first layer of the second specimen, and so on. While the time it takes to print a single layer is unchanged, the time between layer deposition is increased allowing the partially completed specimen to cool and thus limiting the ability for the polymer chains to move about the interface, altering the strength of the layer adhesion. To quantify the reduction in strength with respect to the number of specimens printed sequentially, Z+90+90 specimens were printed sequentially, as well as cut from a plaque, and tested under uniaxial tensile load. As shown in **Figure 29**, this nozzle path for sequential printing resulted in a decrease in strength and an increase in variability. Plaque printing resulted in the lowest strength and highest variability given the longer time between layer depositions.

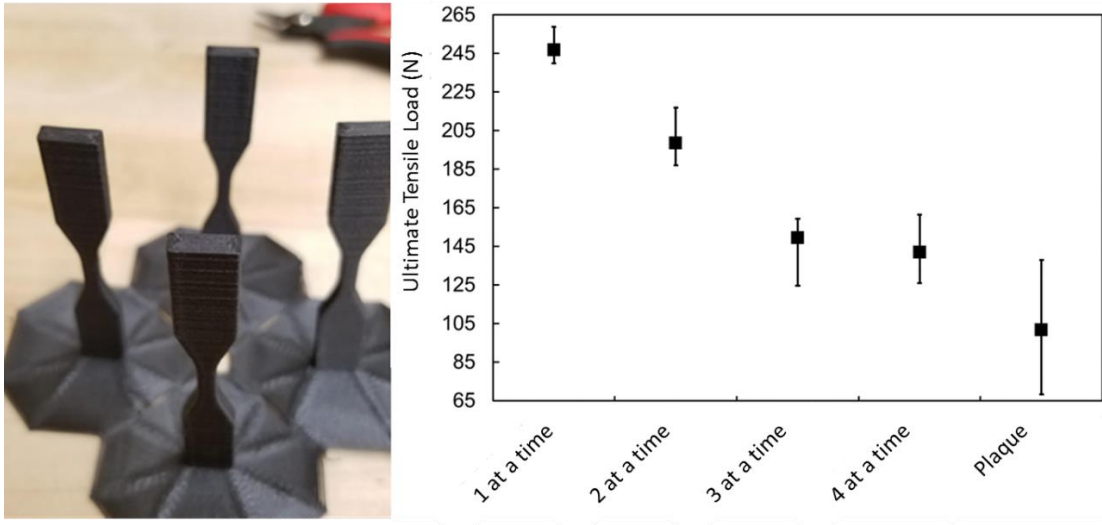


**Figure 29** Multiple Z +90+90 specimens printed during a single print with the nozzle depositing one layer for all specimens. When printing 4 specimens, shown on the left, the increased effective layer time for each specimen causes significant reductions in ultimate

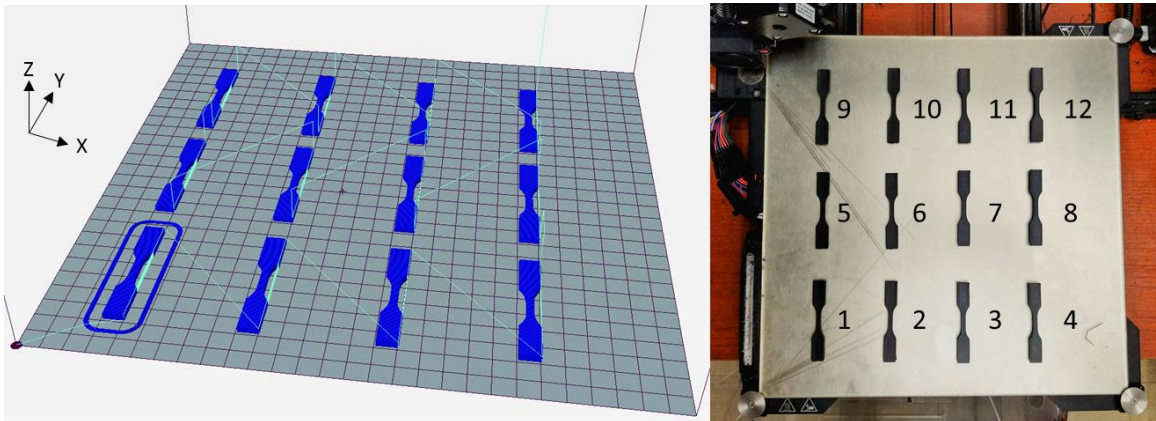


**Figure 30** Location of sequential prints on the print bed. Each individual specimen is printed to completion before moving to the next.

To utilize the available platform space and minimize print time without decreasing strength, the default g-code was modified to set the nozzle path to completely print each specimen before moving to the next, as demonstrated for 12 sequential prints of +90+90 specimens in **Figure 30**. The total printing time was 64 minutes to fabricate all 12 specimens sequentially whereas the print time for one specimen alone is 25 minutes resulting in total print time of 300 minutes needed to print full set of 12 specimens. When printing individually, a skirt or brim is applied to help improve the adhesion to the bed and limit the effects of warping, but when 12 specimens were printed onto the bed sequentially there was no need for a brim or skirt based on observations further reducing print time relative to individual printing.

Despite the modification to the deposition path, a 30% reduction remains in the tensile strength between individually prints and sequential prints (**Figure 31**). However, there was a 100% increase in the number of valid test specimens for the sequential prints. This increase in repeatability and the reduction in time spent printing provides a lower strength but higher return option for low strength and mid to high level production parts. Further investigation into the effects of bed placement on strength is needed to determine the cause of the variability seen in **Figure 32** which shows specimen ultimate tensile strength relative to bed location.

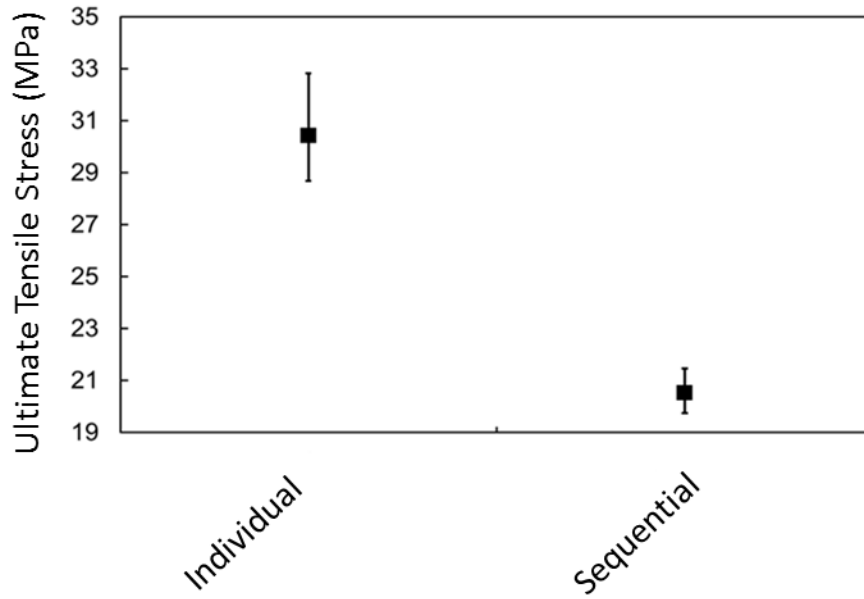


**Figure 31** Sequential prints versus individual prints in the same orientation (+90+90) provide different ultimate strength results.

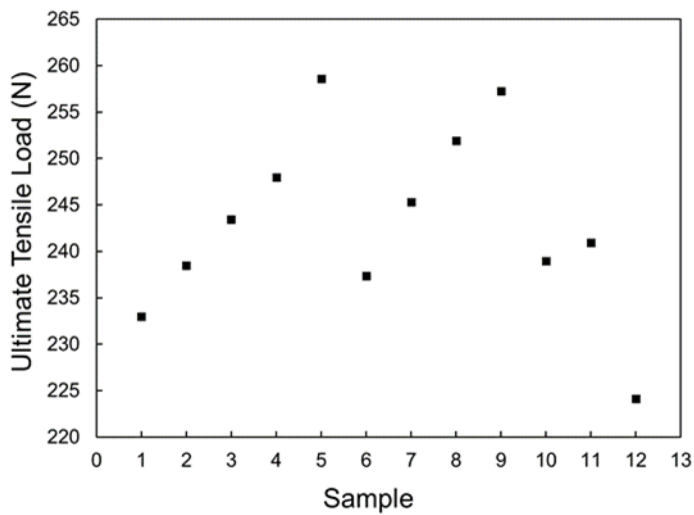


**Figure 32** Sequential prints demonstrate variability in strength relative to bed location

## Cutting Technique

Fabricating specimens from plaques introduces the effects of abrasives or heating that could potentially influence the specimen behavior. Experimental testing was performed to investigate if the method used during the cutting process imparted any noticeable effects on tensile strength, compared to each other. The two techniques studied were waterjet, on an OMAX 2626 JetMachining Center, and Computer Numeric Control (CNC), on a HAAS VF4 CNC Mill. As shown in **Figure 33**, results show limited effects on the average tensile load applied to these specimens. There is increased variability and reduced ultimate tensile strength in plaque prints due to the longer layer times associated with these larger prints, however the effect of the type of cutting process is not an apparent trend in the data as shown in **Figure 34**. The mean and standard deviation are shown in **Table 10** and shown when excluding all outliers. In addition, optical microscopy images (**Figure 35**) displayed minimal differences in the observable bead behavior and no clear effects of re-melting or the injection of abrasive from the cutting processes.

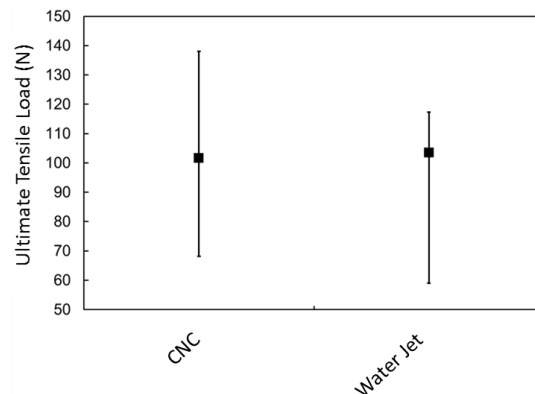


**Figure 33** Ultimate tensile loads of specimens cut using two different methods: CNC and Water Jet.

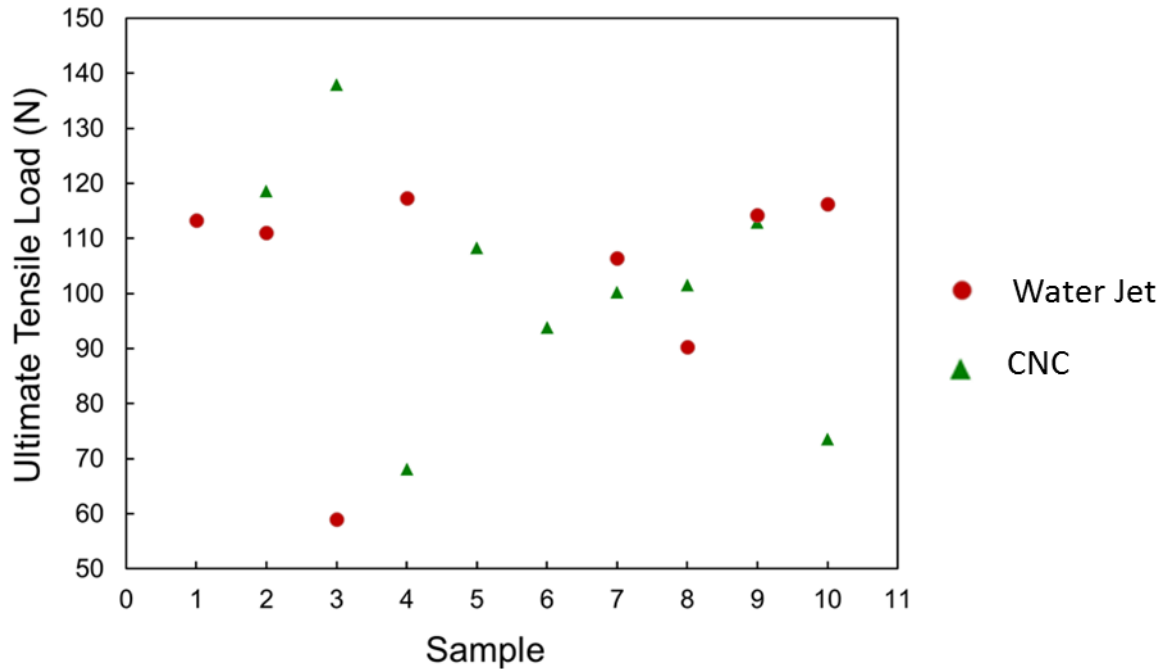


**Figure 34** Ultimate tensile load of each individual specimen fabricated with CNC or waterjet cutting methods.

**Table 10** The mean and standard deviation reported for all of the samples per set and with all of the outliers removed from each data set.

|     | All Samples |         | Outliers Removed |         |
|-----|-------------|---------|------------------|---------|
|     | Mean        | Std Dev | Mean             | Std Dev |
| CNC | 101.70      | 20.45   | 105.94           | 8.34    |
| WJ  | 103.48      | 18.67   | 109.84           | 8.66    |

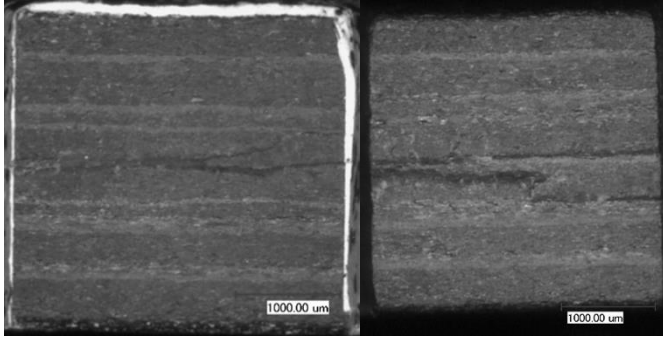


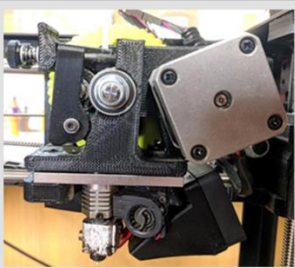
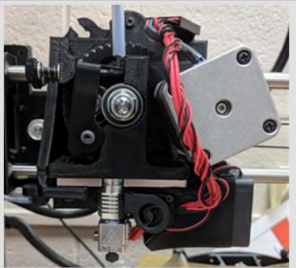
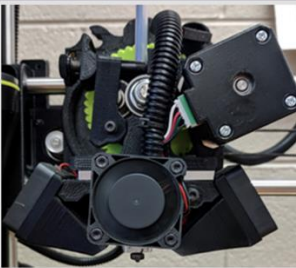
**Figure 35** The image on the left shows the cross-section at the failure location during tensile testing for a specimen cut by CNC machining and the image on the right shows a corresponding failure location for a specimen cut using waterjet machining.

### *Printer Variability*

For production efficiency, manufacturers simultaneously print on different machines to rapidly produce the desired amount of parts, therefore, it is critical to investigate the variability due to the printer itself. Three printers from the manufacturer Lulzbot were investigated to isolate the variability due FFF machine model type. The machine features and differences are provided in **Figure 36** to identify potential sources of variability. All specimens were printed under the baseline conditions previously outlined using the same g-code in order to isolate the effects due to printer type.

**Figure 37** shows the average specimen results for each printer type. The yield stress, failure stress, and behavior in the region of proportionality was quite different for each machine type. With the varying number of fans and structural effects due to bed size and cooling profiles, specimens showed different levels of layer adhesion, manifested as yield strength and strength at failure. The samples

printed on the Taz 6 demonstrated a higher ultimate strength when compared to the other two printers. The Mini demonstrated a significantly increased region of plastic deformation as compared to the other printers. The Taz 5 prints demonstrated the most brittle behavior comparatively. The effects of printhead configuration also affected the repeatability of test results (**Figure 38**). The repeatability of each machine was quantified by the statistical differences in the yield stress and ultimate stress and the number of valid test specimens for each printer (**Table 11**). There was a substantially reduced number of valid tests for Taz 6 specimens when compared to the Taz 5 and the Mini.

| Comparison of Lulzbot Taz Mini, Taz 5, and Taz 6 |  |   |  |
|--|--|---|--|
| Structure  |  |  |  |
| Machine  | Taz Mini   | Taz 5   | Taz 6  |
| Auto-leveling                                    | Yes  | No, Manual Calibration  | Yes  |
| Fan Orientation                                  | Direct on Filament and Hot end with complete control over both                     | Direct on Filament and Hot end with partial control over Hot End                    | Dual-Centered Fan on Filament and single Hot end with partial control                |
| Number of Fans                                   | 1 Major 1 Minor  | 1 Major 1 Minor   | 2 Major 1 Minor  |
| Self Cleaning                                    | Nozzle Wiping  | None  | Nozzle Wiping  |
| Bed Size   | 152mm x 152mm x 158mm  | 290mm x 275mm x 250mm   | 280mm x 280mm x 250mm  |
| Hot Ends   | Hexagon Hot End  | Hexagon Hot End   | V2 Hexagon Hot End   |

**Figure 36** Comparison data of machine features for Lulzbot Taz Mini (left), Taz 5 (center), and Taz 6 (right) printers.



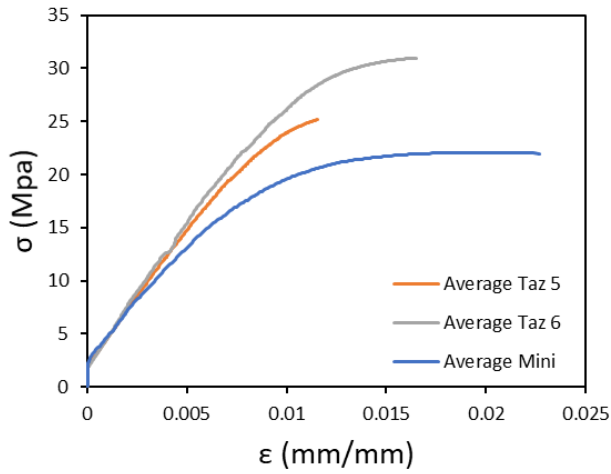


**Figure 37** Average stress vs strain computed from valid results using specimens fabricated and tested with different Lulzbot printers.

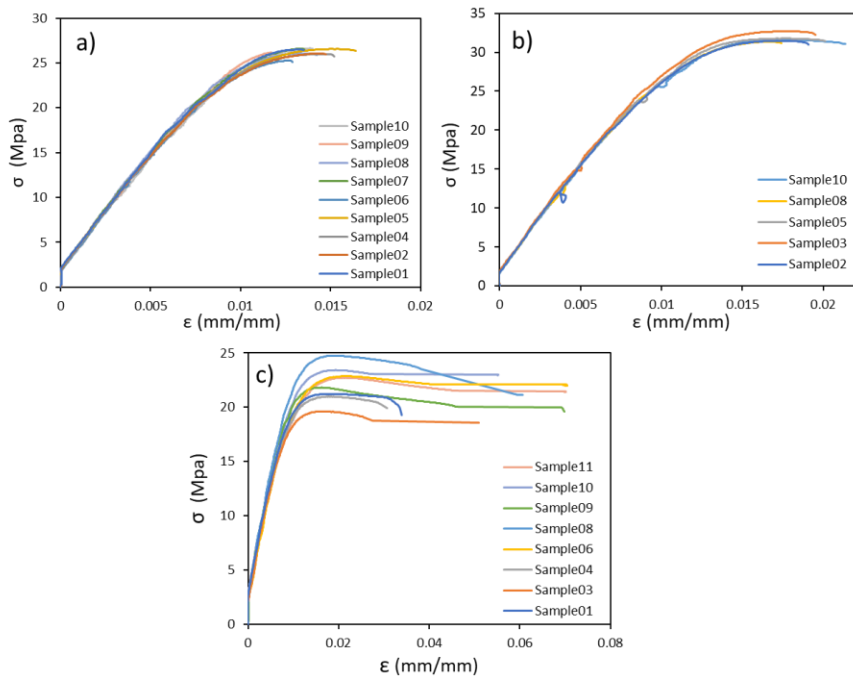


**Figure 38** Stress strain plots for each valid individual test specimen fabricated with (a) Taz 5, (b) Taz 6, (c) Mini.

**Table 11** Mean and standard deviation of the yield stress and failure stress of specimens fabricated from the various printers.

|                | Taz 6 (N=5) |      | Taz 5 (N=9) |      | Mini (N=8) |      |
|----------------|-------------|------|-------------|------|------------|------|
|                | Mean        | S.D. | Mean        | S.D. | Mean       | S.D. |
| Yield Stress   | 21.61       | 0.85 | 21.01       | 1.48 | 17.99      | 1.79 |
| Failure Stress | 31.37       | 0.47 | 26.10       | 0.44 | 20.88      | 1.73 |

## Discussion

The difference in testing results throughout the literature and reported through this test program suggests that on a material by material basis, current testing standards are not capable of producing repeatable and comparable results for FFF specimens. The results of this investigation indicate that not only must testing standards be modified for FFF materials, but consistent reporting nomenclature and designation of control settings and fabrication techniques must accompany test results. Discussion of significant results from this investigation is provided for each category.

## Classification

A primary goal of this paper is to provide original data to supplement and fill in knowledge gaps in the mechanical testing of FFF parts, particularly that of strength testing. Based on the current bulk of literature and the provided data, it is evident that the tensile strength of FFF specimens is dependent on specimen size as well as geometry, along with other unique considerations for FFF materials. The print

orientation imparts large effects on the strength values which creates a more elaborate need to isolate the weakest available configuration for testing in order to provide a relevant factor of safety. The interfacial bonding is the weakest where the mechanically crosslinked sections of polymers are providing the strength of the material. When the beads are oriented in such a way to align the beads with the pull direction, the actual polymer chains are loaded creating a much stronger part. Of particular interest in qualification is a unification of naming to encapsulate all available print orientations to create a standard method to isolate the lowest strength for qualification purposes.

Specimen sizing is also of major importance for future qualification standards where layer times and part size completely change the polymer chain dynamics at the interface. Larger prints have an increased amount of time to print corresponding to intensified cooling and reheating cycles. Increasing the overall time to print, as well as the time to print each individual layer, results in altered chain dynamics, impacting the overall tensile strength. This dependency is relevant to material qualification in that specimens should reflect the print conditions and geometry of the part. Larger specimens should be tested to represent larger parts with a high number of layers to realistically capture cooling effects, and smaller specimens should be tested to represent smaller parts to capture the heating effects of the bed in order to obtain appropriate strength values for design.

Therefore, current standards, such as ASTM D638-14, must be modified for the determination of the tensile properties of fiber reinforced FFF plastic specimens. Additional configuration considerations that must be addressed include: the thermal profile during extrusion when selecting a specimen size, the raster pattern in addition to the fillet radius, and the number of beads and layers in the cross-section. Rather than specifying dimensions, it may be more applicable to specify the number of beads required in the cross-section and the number of layers that are required through the length when selecting an appropriately sized

specimen to achieve the true mechanical property for a set of prescribed extrusion conditions. Given the variation in mechanical properties due to the number of bead interfaces, the weakest local areas in a volume of FFF material, it is necessary to evaluate the required cross-sectional area and gauge length necessary to determine statistically relevant mechanical properties. Larger scale and small-scale printing are used for significantly different part production and further research should be done to compare specimen configuration requirements in order to create appropriate standards for the scale up process.<sup>62</sup>

### ***Extrusion***

Each print parameter can significantly affect the strength and stiffness of FFF specimens. As the material is deposited, during the FFF process, cooling begins to happen immediately and temperature-based solidification happens. Both conductive and radiative heat losses dictate the thermal profile of the print and subsequently impact the transition of the material from viscous fluid to viscoelastic solid. Due to the insulating properties of the thermoplastic material, internal and external cooling rates differ, resulting in the buildup of surface or internal stresses and strains which can result in part deformation such as warping or sagging. The addition of carbon fibers alters the coefficient of thermal expansion and increases the conductivity, also influencing the polymer chain dynamics. The complexity of the physical phenomena happening at the interface of each layer underlines the incredible challenge in qualification where any printing parameter that changes contact area, material deposition, temperature, and cooling can positively or negatively impact the part.

For this paper, fan speed, nozzle temperature, platform temperature, and bead height were investigated as the most critical in controlling the temperature

profile of the specimen for layer adhesion, where in the bead-to-bead loading configuration, tensile strength is dependent on the layer adhesion. It was determined that higher temperature does not always lead to increased strength, but it does impact the reptation of polymer chains between layers and the repeatability of test results. This reptation is dependent on the printing parameters, where the material needs to remain above the glass transition temperature in order to move into an entropically favorable conformation and impacts the microstructure of intrabead and interbead interactions causing variation in the mechanical performance of the material. The effects of bed temperature demonstrate that higher temperature also does not lead to increased strength, where in the case of small dog-bone specimens the thermal gradient could create a build up of internal stresses and decrease the tensile strength. In the case of bead height, too small of a height introduces shear effects and too tall of a height introduces large air gaps in the material. Each of these provides a basis for increased strength, where small bead height decreases the size of raster imparted voids and large bead heights increase the polymer mixing between layers, but each create a negative that offsets any increased strength. This is an important consideration in the mechanical testing and qualification standards where highly specific reporting is necessary due to the complicated physics at the layer-to-layer interface.

Evaluation of material microstructure is performed routinely through SEM, and further understanding the processing-structure-performance relationship is essential for FFF material qualification relative to standardization of print parameters. Due to the variety of challenges associated with the complex physical phenomena, printing parameters dictating extrusion must be further investigated, necessitating computational models and simulations capable of capturing the complex physics.

## ***Methodologies***

This study focused on material qualification for small parts printed on desktop machines, and scale up to meet quantity and size requirements must also be addressed within the qualification standards. As FFF is employed to create end-user parts, methods to increase the output will be implemented. Each method, whether it be sequential printing, post-processing through cutting, or utilizing multiple printers, will need to be designated, tested, and controlled for qualification.

The increased number of prints on the bed reduced the strength but increased the repeatability of specimens prompting further investigation into the effects of multiple prints on the print surface effecting the thermal profiles. Printing multiple specimens on the print surface sequentially provides an increased number of radiative bodies that could impact the flow of ambient air around the specimens. In the case of small prints that remain close to the print surface, a large number of layers are kept warmer than air temperature and therefore could be impacting the overall thermal profile of the prints. This change in thermal profile, remaining at an elevated temperature longer, would create an environment similar to annealing, where the polymer chains are allowed to reach a more favorable conformation, decreasing the overall tensile strength but increasing the repeatability of the interfacial mixing. Further studies isolating the effects of multiple specimens on the thermal profiles should be performed to inform future qualification efforts, especially in fields where scale up is desirable and inevitable.

Initial exploratory investigation of cutting technique did not provide conclusive evidence for the need to specify the cutting technique. The provided data fails to demonstrate any significant impact on ultimate tensile strength of the material however the possibility of re-melt or impregnation of abrasive, from water jet cutting, is possible and is important to consider. In the case of specimen remelting based on post-processing, this would create a slightly altered test

specimen that would not be able to be compared to individually printed specimens. Further comprehensive investigations should be performed that encompass all common and emerging methods of specimen processing.

The use of multiple printers prompts concerns of machine to machine variability, where testing done in this study demonstrated vast mechanical performance variation between printers from the same manufacturer. Investigation of print machine variability requires more comprehensive evaluation with a focus on the effects of extruder head configuration on the localized heating and cooling of the specimens as well peripheral features unique to a make and model. In the case of the presented data, the major differences existed in the number of fans designated for the hot end and nozzle, as well as the overall print surface area. Much like printing multiple specimens on the bed at the same time, alterations in the overall size of the print surface in relation to walls and the printer controls themselves, could result in a different local environment surrounding the print providing the difference in mechanical properties obtained. In addition, the variation in the number of fans controlling the extrusion temperature could result in the large variability prompting the qualification of nozzle design and printers as well as the classification and extrusion parameters.

Qualification of methodologies must be addressed for holistic designation and standardization of mechanical properties reporting. In order to better prepare manufacturers for the increase in part production through FFF printers, qualification needs to encompass the post processing and the machines themselves in order to save time and money at a later date, where the presented data provides significant evidence towards to variability beyond specimen configuration and extrusion conditions.

## Conclusions

Despite the revolutionary impact of AM technologies, the lack of repeatable testing standards that encompass the complexities unique to printed AM materials has slowed market uptake and limited the overall scope of applicability. New AM standards would provide engineers, scientists, and user/operators the ability to globally compare test results for design and manufacturing, further allowing localized and distributed manufacturing infrastructure to emerge. The ability to account for the anisotropic nature of the part as well as the effects of additives and material blends on the strength and stiffness obtained through tensile testing is needed before widespread adoption of FFF parts for primary load-carrying structure is achieved. In order to create these qualification standards, investigations and reports of processing parameters, orientations, scale-up, and many other complexities are needed while accounting for interacting effects. The interaction of part geometry, orientation, and processing parameters has not been well documented and is necessary to create a standard procedure for testing and production. The primary conclusions of this study are:

- Specimen size and geometry significantly affects strength and repeatability of tensile specimens and a standard FFF specimen configuration must be developed through a comprehensive evaluation. Rather than standardizing dimensions, it may be more applicable to specify the number of beads that are required in the cross-section to achieve geometry independent material properties.
- Continued development and unification of naming and fabrication techniques are needed to compare testing results from disparate sources.



- Controlling layer times and printing processes can lead to both stronger prints and more time efficient fabrication, and extrusion control setting information must accompany test results.
- Printer to printer variability exists, even when fabricating specimens on identical makes and models, and designation of equipment must be considered in the qualification process.

### **Acknowledgments**

Financial support was provided by the Naval Education Engineering Consortium, grant N00174-16-C0033, under the direction of Dr. Maureen Foley at the Naval Surface Warfare Center Carderock Division.

## References

1. Ford, S. & Despeisse, M. Additive manufacturing and sustainability: an exploratory study of the advantages and challenges. *J. Clean. Prod.* 137, 1573–1587 (2016).
2. Neely, A. Exploring the financial consequences of the servitization of manufacturing. *Oper. Manag. Res.* 1, 103–118 (2008).
3. Kalsoom, U., Nesterenko, P. N. & Paull, B. Recent developments in 3D printable composite materials. *RSC Adv.* 6, 60355–60371 (2016).
4. Thomas, D. Costs, Benefits, and Adoption of Additive Manufacturing: A Supply Chain Perspective. *Int J Adv Manuf Technol* 85, (2016).
5. El-katatny, I., Masood, S. H. & Morsi, Y. S. Error analysis of FDM fabricated medical replicas. (2010). doi:10.1108/13552541011011695
6. Kusumoto, N. & Wakabayashi, K. CAD / CAM fabrication and clinical application of surgical template and bone model in oral implant surgery. 87–93 (2009). doi:10.1111/j.1600-0501.2008.01588.x
7. Klebe, T. Client Story: KRC Power Steering. *TriMech Blog* (2017).
8. Bedsole, R. & Riha, D. BIG AREA ADDITIVE MANUFACTURING ( BAAM ) MATERIALS DEVELOPMENT AND Authors : (2018).
9. Uriondo, A., Esperon-Miguez, M. & Perinpanayagam, S. The present and future of additive manufacturing in the aerospace sector: A review of important aspects. *Proc. Inst. Mech. Eng. Part G J. Aerosp. Eng.* 229, 2132–2147 (2015).
10. Tian, X., Liu, T., Yang, C., Wang, Q. & Li, D. Interface and performance of 3D printed continuous carbon fiber reinforced PLA composites. *Compos. Part A Appl. Sci. Manuf.* 88, 198–205 (2016).
11. Love, L. J. et al. The importance of carbon fiber to polymer additive manufacturing. *J. Mater. Res.* 29, 1893–1898 (2014).

12. Klippstein, H., Diaz De Cerio Sanchez, A., Hassanin, H., Zweiri, Y. & Seneviratne, L. Fused Deposition Modeling for Unmanned Aerial Vehicles (UAVs): A Review. *Adv. Eng. Mater.* 20, 1–17 (2018).
13. Wimpenny, D. I., Pandey, P. M. & Kumar, L. J. *Advances in 3D Printing & Additive Manufacturing Technologies.* (Springer US, 2016).
14. Strataysys. Produce Certified Aircraft Interiors with 3D Printing. *Aviation Week* (2018). Available at: <http://aviationweek.com/connected-aerospace/produce-certified-aircraft-interiors-3d-printing>. (Accessed: 5th December 2018)
15. Vialva, T. U.S. Navy Engineers Use 3D Printing to Repair Combat Equipment. *3D Printing Industry* (2018). Available at: <https://3dprintingindustry.com/news/u-s-navy-engineers-use-3d-printing-to-repair-combat-equipment-139708/>. (Accessed: 12th October 2018)
16. Kujawa, M. Assessment of 3D printing as a manufacturing technology for drones' wings. in *Interdyscyplinarność badań naukowych* 66–71 (2017).
17. Coxworth, B. Tough 3D-printed drone features embedded electronics. *New Atlas* (2016).
18. Norfolk, M., Moreau, C., Crease, A. & Fried, S. What's the Role of 3D Printing in Embedded Systems. *Circuit Cellar* (2018).
19. Wyman, C. Additive Manufacturing for Aerospace: FAA-Approved Air Duct for 'Flying Eye Hospital' Produced in Just Days. *Stataysys* (2015). Available at: <http://blog.strataysys.com/2015/03/05/3d-printed-air-duct-flying-eye-hospital/>. (Accessed: 8th April 2017)
20. Busta, H. This Architect-Designed Wall System Has a 3D-Printed Core. *Architect Magazine* (2015).
21. Artley, B. Automotive 3D Printing Applications. *3D Hubs*
22. Prater, T. J. et al. Summary Report on Phase I Results From the 3D Printing in Zero-G Technology Demonstration Mission, Volume I. I, (2016).

23. Barbagallo, J. Additive Manufacturing in Maintenance, Preventive Maintenance, and Alteration of Aircraft, Aircraft Engines, Propellers, and Appliances. (2016).
24. NASA. Standard for Additively Manufactured Spaceflight Hardware by Laser Powder Bed Fusion in Metals. (2017).
25. U.S. FDA. Technical Considerations for Additive Manufactured Medical Devices. (2017).
26. Di Prima, M. et al. Additively manufactured medical products – the FDA perspective. *3D Print. Med.* 2, 4–9 (2016).
27. Week, I. ASTM, Boeing, Setting Additive Manufacturing Standard for Plastics. *Industry Week* (2019).
28. Seifi, M. et al. Progress Towards Metal Additive Manufacturing Standardization to Support Qualification and Certification. *Jom* 69, 439–455 (2017).
29. Forster, A. M. Materials Testing Standards for Additive Manufacturing of Polymer Materials : Nist.Ir.8059 (2015).  
doi:<http://dx.doi.org/10.6028/NIST.IR.8059>
30. Wu, W. et al. Influence of layer thickness and raster angle on the mechanical properties of 3D-printed PEEK and a comparative mechanical study between PEEK and ABS. *Materials (Basel)*. 8, 5834–5846 (2015).
31. Tekinalp, H. L. et al. Highly oriented carbon fiber-polymer composites via additive manufacturing. *Compos. Sci. Technol.* 105, 144–150 (2014).
32. Ning, F., Cong, W., Hu, Y. & Wang, H. Additive manufacturing of carbon fiber-reinforced plastic composites using fused deposition modeling: Effects of process parameters on tensile properties. *J. Compos. Mater.* 51, 451–462 (2017).
33. Turner, B. N., Strong, R. & Gold, S. A. A review of melt extrusion additive manufacturing processes: I. Process design and modeling. *Rapid Prototyp. J.* 20, 192–204 (2014).

34. International, A. Standard Practice for Reporting Data for Test Specimens Prepared by Additive Manufacturing. ASTM Stand. (2013).  
doi:10.1520/F2971-13
35. ASTM International. ISO / ASTM52900-15, Standard Terminology for Additive Manufacturing – General Principles – Terminology. ASTM Stand. (2015). doi:10.1520/ISOASTM52900-15
36. Dasari, A., Yu, Z. Z., Cai, G. P. & Mai, Y. W. Recent developments in the fire retardancy of polymeric materials. *Prog. Polym. Sci.* 38, 1357–1387 (2013).
37. Li, Y. & Shimizu, H. Improvement in toughness of poly(l-lactide) (PLLA) through reactive blending with acrylonitrile-butadiene-styrene copolymer (ABS): Morphology and properties. *Eur. Polym. J.* 45, 738–746 (2009).
38. ASTM Norma. Standard Test Method for Tensile Properties of Plastics. Annu. B. ASTM Stand. 1–15 (2004). doi:10.1520/D0638-14.1
39. Weng, Z., Wang, J., Senthil, T. & Wu, L. Mechanical and thermal properties of ABS/montmorillonite nanocomposites for fused deposition modeling 3D printing. *Mater. Des.* 102, 276–283 (2016).
40. Cole, D. P., Riddick, J. C., Iftekhhar Jaim, H. M., Strawhecker, K. E. & Zander, N. E. Interfacial mechanical behavior of 3D printed ABS. *J. Appl. Polym. Sci.* 133, 1–12 (2016).
41. Torrado, A. R. & Roberson, D. A. Failure Analysis and Anisotropy Evaluation of 3D-Printed Tensile Test Specimens of Different Geometries and Print Raster Patterns. *J. Fail. Anal. Prev.* 16, 154–164 (2016).
42. Shofner, M. L., Lozano, K., Rodríguez-Macías, F. J. & Barrera, E. V. Nanofiber-reinforced polymers prepared by fused deposition modeling. *J. Appl. Polym. Sci.* 89, 3081–3090 (2003).
43. Jain, P. K., Pandey, P. M. & Rao, P. V. M. Effect of delay time on part strength in selective laser sintering. *Int. J. Adv. Manuf. Technol.* 43, 117–126 (2009).

44. Ahn, S., Montero, M., Odell, D., Roundy, S. & Wright, P. K. Anisotropic material properties of fused deposition modeling ABS. *Rapid Prototyp. J.* 8, 248–257 (2002).
45. Es-Said, O. S. et al. Effect of Layer Orientation on Mechanical Properties of Rapid Prototyped Samples. *Mater. Manuf. Process.* 15, 107–122 (2000).
46. Hwang, S., Reyes, E. I., Moon, K. sik, Rumpf, R. C. & Kim, N. S. Thermo-mechanical Characterization of Metal/Polymer Composite Filaments and Printing Parameter Study for Fused Deposition Modeling in the 3D Printing Process. *J. Electron. Mater.* 44, 771–777 (2015).
47. Tymrak, B. M., Kreiger, M. & Pearce, J. M. Mechanical properties of components fabricated with open-source 3-D printers under realistic environmental conditions. *Mater. Des.* 58, 242–246 (2014).
48. Masood, S. H. & Song, W. Q. Development of new metal/polymer materials for rapid tooling using Fused deposition modelling. *Mater. Des.* 25, 587–594 (2004).
49. Goh, G. D. et al. Characterization of mechanical properties and fracture mode of additively manufactured carbon fiber and glass fiber reinforced thermoplastics. *Mater. Des.* 137, 79–89 (2018).
50. Kalsoom, U., Nesterenko, P. N. & Paull, B. Recent developments in 3D printable composite materials. *RSC Adv.* 6, 60355–60371 (2016).
51. Cantrell, J. T. et al. Experimental characterization of the mechanical properties of 3D-printed ABS and polycarbonate parts. *Rapid Prototyp. J.* 23, 811–824 (2017).
52. Gray, R. W., Baird, D. G. & Helge Bøhn, J. Effects of processing conditions on short TLCP fiber reinforced FDM parts. *Rapid Prototyp. J.* 4, 14–25 (1998).
53. Matsuzaki, R. et al. Three-dimensional printing of continuous-fiber composites by in-nozzle impregnation. *Sci. Rep.* 6, 23058 (2016).

54. de Leon, A. C. et al. High performance polymer nanocomposites for additive manufacturing applications. *React. Funct. Polym.* 103, 141–155 (2016).
55. Brenken, B., Barocio, E., Favaloro, A., Kunc, V. & Pipes, R. B. Fused filament fabrication of fiber-reinforced polymers: A review. *Addit. Manuf.* 21, 1–16 (2018).
56. Stansbury, J. W. & Idacavage, M. J. 3D printing with polymers: Challenges among expanding options and opportunities. *Dent. Mater.* 32, 54–64 (2016).
57. Green, P. E., Winer, B. J., Brown, D. R. & Michels, K. M. *Statistical Principles in Experimental Design*. *Journal of Marketing Research* 29, (McGraw-Hill Humanities/Social Sciences/Languages, 1992).
58. Heller, B., Smith, D. E. & Jack, D. A. The effects of extrudate swell, nozzle shape, and the nozzle convergence zone on fiber orientation in fused deposition modeling nozzle flow. in *American Society for Composites Proceedings* 1220–1236 (2015).
59. Heller, B. P., Smith, D. E. & Jack, D. A. Effects of extrudate swell and nozzle geometry on fiber orientation in Fused Filament Fabrication nozzle flow. *Addit. Manuf.* 12, 252–264 (2016).
60. Heller, B. P., Smith, D. E. & Jack, D. A. Computing mechanical properties from orientation tensor for fiber filled polymers in axisymmetric flow and planar deposition flow. in *SPE ACCE* (2016).
61. Kousiatza, C., Chatzidai, N. & Karalekas, D. Temperature mapping of 3D printed polymer plates: Experimental and numerical study. *Sensors (Switzerland)* 17, (2017).
62. Dinwiddie, R. B. et al. Infrared imaging of the polymer 3D-printing process. *Proc. SPIE - Int. Soc. Opt. Eng.* 9105, 910502 (2014).
63. Sun, Q., Rizvi, G. M., Bellehumeur, C. T. & Gu, P. Effect of processing conditions on the bonding quality of FDM polymer filaments. *Rapid Prototyp. J.* 14, 72–80 (2008).

64. Sood, A. K., Ohdar, R. K. & Mahapatra, S. S. Parametric appraisal of mechanical property of fused deposition modelling processed parts. *Mater. Des.* 31, 287–295 (2010).
65. Rodríguez, J. F., Thomas, J. P. & Renaud, J. E. Mechanical behavior of acrylonitrile butadiene styrene fused deposition materials modeling. *Rapid Prototyp. J.* 9, 219–230 (2003).
66. Rodríguez, J. F., Thomas, J. P., Renaud, J. E., Thomas, J. P. & Renaud, J. E. Mechanical behavior of acrylonitrile butadiene styrene ( ABS ) fused deposition materials . Experimental investigation. *Rapid Prototyp. J.* 7, 148–158 (2001).
67. Riddick, J. et al. Effect of Manufacturing Parameters on Failure in Acrylonitrile-Butadiene-Styrene Fabricated by Fused Deposition Modeling. in *Collection of Technical Papers - AIAA/ASME/ASCE/AHS/ASC Structures, Structural Dynamics and Materials Conference* (2012).
68. Ning, F., Cong, W., Qiu, J., Wei, J. & Wang, S. Additive manufacturing of carbon fiber reinforced thermoplastic composites using fused deposition modeling. *Compos. Part B Eng.* 80, 369–378 (2015).
69. Zhong, W., Li, F., Zhang, Z., Song, L. & Li, Z. Short fiber reinforced composites for fused deposition modeling. *Mater. Sci. Eng. A301* 301, 125–130 (2001).
70. Kantaros, A. & Karalekas, D. Fiber Bragg grating based investigation of residual strains in ABS parts fabricated by fused deposition modeling process. *Mater. Des.* 50, 44–50 (2013).
71. Dul, S., Fambri, L. & Pegoretti, A. Fused deposition modelling with ABS-graphene nanocomposites. *Compos. Part A Appl. Sci. Manuf.* 85, 181–191 (2016).
72. Chockalingam, K., Jawahar, N., Chandrasekar, U. & Ramanathan, K. N. Establishment of process model for part strength in stereolithography. *J. Mater. Process. Technol.* 208, 348–365 (2008).



73. Turner, B. N. & Gold, S. A. A review of melt extrusion additive manufacturing processes: II. Materials, dimensional accuracy, and surface roughness. *Rapid Prototyp. J.* 21, 250–261 (2015).
74. Rosenzweig, N. & Narkis, M. Observation and analysis technique for studying sintering of polymeric particles. *J. Appl. Polym. Sci.* 26, 2787–2789 (1981).
75. Varma. Properties and Kinetics of Thermally Crystallized Oriented Poly(Ethylene Terephthalate) (PET). I: Kinetics of Crystallization. *Polym. Eng. Sci.* 38, 245–253 (1998).

**CHAPTER III**  
**TENSILE STRENGTH DEPENDENCE OF FFF FIBER**  
**REINFORCED ABS ON ENVIRONMENTAL CONDITIONING**

A version of this chapter was originally published by William H. Ferrell, Corey Arndt, and Stephanie C. TerMaath:

William H. Ferrell. Corey M. Arndty and Stephanie C. TerMaath. "Tensile Strength Dependence of FFF Fiber Reinforced ABS on Environmental Conditioning" *Mechanics of Advanced Materials and Structures*. 0 (2020): 1-14.

I, William Ferrell, was the primary author of this review with assistance of Corey Arndt and from my Advisor, Dr. Stephanie TerMaath. Mr. Arndt assisted in testing and the writing of the results section of this paper.

## **Abstract**

Evaluation of environmental durability is essential for the qualification of polymeric materials used in Fused Filament Fabrication and certification of the manufactured parts. Polymer chain motion at temperatures approaching the glass transition temperature and water ingress into voids impact the response of these materials to load. To investigate these effects, uniaxial tension testing was performed after conditioning specimens under heat or moisture. Results showed that conditioning temperature substantially influences the failure strain in multiple orientations. Both heat, beyond 50°C, and moisture create increased variability of the specimen response to load, both in ultimate tensile strength and elongation to break.

## **Introduction**

Additive manufacturing (AM) is a disruptive technology offering several advantages over conventional manufacturing approaches, including complex geometry fabrication, reduced waste material, lower part counts, and an accelerated timeline from design to final part.<sup>1-5</sup> Due to these enabling benefits,

this manufacturing technique is impacting part fabrication across industries, including marine, aerospace, and automotive, with part scales ranging from millimeter (mm) to Big Area Additive Manufacturing (BAAM) for full scale structures.<sup>6-12</sup> Despite the advantages of AM and widespread interest in continued implementation of this technology to an increasing range of applications, a greater understanding of the in-situ performance of AM parts is essential to develop design guidelines, inspection methods and timelines, and structural reliability criteria. For example, in the case of marine applications, high humidity and high temperatures are expected on ships, off-shore platforms, and other structure in marine environments,<sup>13</sup> and quantification of the effects of these conditions on AM parts is lacking.

Understanding the effects of heat and moisture on polymers used for Fused Filament Fabrication (FFF) is particularly important. FFF is a low cost, readily available and industry favorite technique.<sup>5</sup> A majority of feedstocks used in the FFF method are thermoplastics, for which the material becomes pliable above a specific temperature and then solidifies below that temperature.<sup>11,14-19</sup> This threshold is defined as the glass transition temperature ( $T_g$ ), and is specific to an individual polymer based on its structure. The  $T_g$  of a material characterizes the range of temperatures that define the onset of the change in physical properties from an elastic solid, or glassy state, into a viscoelastic, or rubbery, state. While heating filament above the  $T_g$  for extrusion enables the 3D printing of these materials, exposure to temperatures near or above the  $T_g$  during part use can be problematic. Additionally, the FFF process creates voids along the bead to bead adhesion points,<sup>20-22</sup> leaving the parts susceptible to increased absorption of water from the environment. This water ingress can potentially cause material degradation and lead to increased variability in the performance of these parts. Therefore, to define in-situ temperature ranges and moisture content limitations for structural reliability of FFF composite parts, characterization of the environmental effects on strength and repeatability is required.

Currently very few available studies investigated the effects of environmental conditioning on FFF parts. In one study, acrylonitrile-butadiene-styrene (ABS) material was tested by fabrication under ambient conditions and in a desiccant chamber.<sup>23</sup> Another study investigated the effect of moisture and heat on pure ABS.<sup>24</sup> This previous research provided significant evidence that moisture and heat played an important role in printing and structural performance. However, the temperature limit at which tensile strength begins to decrease is not clear, and the material behavior of FFF parts at temperatures close to the  $T_g$  remains unexplored. In addition, the effect of heat or moisture on the layer to layer interface and along the bead has yet to be fully differentiated. A targeted understanding of environmental durability is needed to quantify the structural reliability of composite parts manufactured using FFF.

To begin to develop this essential knowledge, the objective of this paper is to explore and quantify the effects of environmental conditioning on the tensile properties of unreinforced ABS and chopped fiber reinforced ABS (CF-ABS). ABS and CF-ABS were chosen as commonly used materials for structural use and engineering design, due to thermal resistance, toughness, and rigidity, as provided by the acrylonitrile, the butadiene, and the styrene, respectively.<sup>25-27</sup> The material behavior in both of the major orientations, layer to layer and along the bead, were investigated under heat or moisture to bound the environmental effects, close to the  $T_g$  and fully soaked in water. The results of tensile testing under environmental conditions were supplemented with dynamic mechanical analysis (DMA) and scanning electron microscopy (SEM) to elucidate structure-performance relationships. Differential scanning calorimetry/thermogravimetric analysis (DSC/TGA) was performed to probe the moisture content of samples after exposure to water submersion and then at ambient atmosphere. It will be shown that correlation between environmental conditioning and the performance of ABS

and CF-ABS material under tensile load demonstrates the need to adjust material qualification standards based on in-situ environmental conditions.

## Materials and Test Methods

### *Fabrication*

Tables 3DXTech ABS with 15 wt.% chopped carbon fiber (CF-ABS) and 3DXTech ABS without carbon fiber specimens were printed on a Lulzbot Taz 6 printer operating through the printer control software Repetier Host using the open source slicer Slic3r. Tensile specimens were printed in the dimensions provided by the ASTM D638-14 Type I standard, due to consistent response to load and a larger material volume for more control over testing temperature.<sup>27,28</sup> The printing conditions utilized a nozzle temperature of 232 °C, a bed temperature of 110 °C, a layer height of 0.2 mm, and were printed in the center of the bed with fan speed set to 0%. These values were chosen as the midpoint of the recommended printing conditions provided by the filament manufacturer and demonstrated consistent mechanical properties in previous studies.<sup>27</sup>

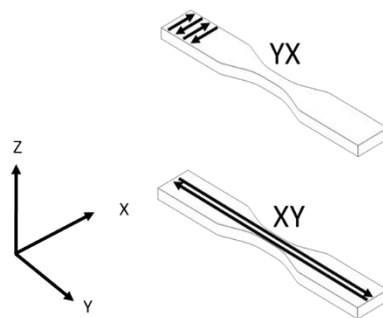


**Figure 39** Layer-to-layer orientation (YX) and along the bead (XY) isolation. Figure dimensions not representative of actual test specimens

The test specimens were printed in two orientations to isolate the layer-to-layer strength (YX) and the strength along the bead (XY), defined in **Figure 39**, to better understand the effect of heat and moisture on these properties. Specimens were tested at the range of temperatures shown in **Table 12**. The naming of the specimens follows the convention of the material type (ABS or CF\_ABS) followed by the orientation in which they were printed (XY or YX). The  $T_g$  of ABS is 105 °C, therefore temperatures chosen encompassed a range from room temperature, 25 °C, to a temperature slightly lower than the  $T_g$ , 90 °C. The initial test plan included testing at the  $T_g$ , however excessive shape distortions were encountered during conditioning as discussed later in this paper. Ten specimens for each material, configuration, and conditioning temperature combination were tested to provide statistically relevant results. Due to the inherent variability in AM printing, there were slight differences in the specimen's gauge width and thickness as demonstrated in **Table 12**.

An evaluation of the effects of smoothing the fillet region was performed on the room temperature CF\_ABS\_XY specimens. The fillet region (tapered section below the grip that ends at the constant width of the gauge section) was smoothed through sanding to reduce the likelihood of stress concentrations that cause specimen failure outside the gauge length. To investigate the effectiveness of this procedure, several specimens were sanded and compared to as-printed specimens to determine the effect of smoothing on the specimen strength and location of failure. No discernable differences were detected between the smoothed and as-printed specimens in this study, so the remainder of testing was performed using as-printed specimens.

**Table 12 Specimen Dimensions, averages, and standard deviations**

| Specimen Dimensions |             |             |                   |                          |
|---------------------|-------------|-------------|-------------------|--------------------------|
| Material            | Orientation | Temperature | Gauge Width<br>mm | Gauge<br>Thickness<br>mm |
| ABS                 | XY          | Room Temp.  | 12.89 ± 0.20      | 3.26 ± 0.09              |
|                     |             | 50°C        | 12.91 ± 0.17      | 3.19 ± 0.04              |
|                     |             | 70°C        | 13.06 ± 0.18      | 3.27 ± 0.08              |
|                     |             | 90°C        | 12.97 ± 0.19      | 3.21 ± 0.06              |
|                     | YX          | Room Temp.  | 12.39 ± 0.20      | 3.36 ± 0.17              |
|                     |             | 50°C        | 13.42 ± 0.16      | 3.26 ± 0.09              |
|                     |             | 70°C        | 13.35 ± 0.15      | 3.31 ± 0.08              |
|                     |             | 90°C        | 13.15 ± 0.34      | 3.30 ± 0.15              |
| CF-ABS              | XY          | Room Temp.  | 12.66 ± 0.26      | 3.14 ± 0.12              |
|                     |             | 50°C        | 12.92 ± 0.15      | 3.14 ± 0.10              |
|                     |             | 70°C        | 13.03 ± 0.15      | 3.14 ± 0.05              |
|                     |             | 90°C        | 13.06 ± 0.18      | 3.22 ± 0.14              |
|                     | YX          | Room Temp.  | 12.97 ± 0.19      | 3.21 ± 0.06              |
|                     |             | 50°C        | 13.42 ± 0.11      | 3.65 ± 0.14              |
|                     |             | 70°C        | 13.43 ± 0.09      | 3.59 ± 0.13              |
|                     |             | 90°C        | 13.15 ± 0.34      | 3.30 ± 0.15              |



For the specimens designated for testing under wet conditions, plaques were printed using CF-ABS, and ASTM D638-14 Type V specimens were extracted in both XY and YX orientation using a waterjet cutting machine. This specimen fabrication method was selected to provide a realistic water uptake scenario for potential parts and to limit raster effects, where specimens are dabbed dry and the surface roughness at the edges could trap surface water. Type V specimens were chosen due to the smaller overall mass of the specimens with regards to available water uptake. Only CF-ABS was included in the current study as previous work has analyzed the diffusion of water into FFF ABS and demonstrated the significant effect of moisture on this hygroscopic material.<sup>24</sup>

### ***Mechanical Testing***

Tensile testing of the specimens was performed according to the ASTM D638-14 standard using an MTS Criterion Model 45 load frame with a 10 kN load cell. The tests were displacement controlled and performed at 1.0 mm/min. All specimens tested at a designated temperature were simultaneously placed in the oven and exposed at temperature for 180 minutes prior to testing. Environmental conditioning followed the procedures for insertion of composite materials as specified by the Naval Sea Systems Command (NAVSEA).<sup>13</sup> Displacement was recorded by means of a laser extensometer paired with the MTS data acquisition software (**Figure 40**). This process was accomplished by attaching two pieces of reflective tape within the gauge of the specimens, and the laser then tracked their displacements during loading.



**Figure 40** *MTS load frame with laser extensometer and specimen loaded with reflective tape attached for extensometer*

Tensile testing of water treated specimens was also performed in conjunction with the laser extensometer. Five specimens of the CF\_ABS\_XY and CF\_ABS\_YX each were tested without submersion. Another five specimens of the CF\_ABS\_XY and CF\_ABS\_YX each were weighed and then soaked in water for 2 hours. Maximum absorption was verified by weighing the specimens every 15 minutes during the soaking in order to monitor the overall weight change until sequential weight measurements were equivalent within a three decimal place threshold. Test specimens were then removed from the water and tested per the procedure outlined by NAVSEA.<sup>13</sup>

## ***Material Characterization***

DMA was performed in flexural oscillation mode to study the viscoelastic properties of the printed material. A small rectangular strip, 25.4 mm x 12.7 mm, was placed in the DMA machine and oscillated at a frequency of 1 Hz.<sup>29</sup> During this oscillation the temperature was ramped at a rate of 5 °C/min. Temperature sweeping under constant oscillation in flexure provides the  $T_g$  of the material and the change in the storage and loss modulus of the material. There are several ways to obtain  $T_g$  based on the DMA test: rapid loss of storage modulus, the maximum of the loss modulus, and the maximum of the tan delta. The  $T_g$  based on the rapid decrease in the storage modulus is pinpointed by plotting the slope of the line before and after the loss, and the intersection of these two slopes is the DMA  $T_g$ . Each of these methods corresponds to a different mechanism or onset of material behavior, where the rapid loss of storage modulus ( $E'$ ) is associated with mechanical failure, the maximum of the loss modulus ( $E''$ ) is associated with the onset of segmental motion and the physical changes in the material, and the tan delta maximum is associated with the midpoint behavior between glassy and rubbery behavior.

TGA was utilized to analyze the chemical degradation of the material to determine the amount of trapped water within the specimen. As the temperature is ramped during the test, the mass is recorded and any decrease in the mass, at specific temperatures, is associated with the burn off of a particular element or compound. The amount of mass drop at 100 °C was monitored in order to determine the amount of trapped water within the system. SEM was performed on select specimens using a Zeiss EVO system in order to observe any difference in the layer adhesion and carbon fiber effects.

## Experimental Testing Results

Testing results for a specimen were considered valid if the failure location was within the gauge length. Any specimens that exhibited distinguishing break patterns or locations are presented.

### ABS\_XY

The averages and standard deviations of the tensile test results for the ABS\_XY specimens are displayed in **Table 13**, with the stress versus strain curves for each conditioning temperature in **Figure 41**. This specimen print orientation, that was loaded along the beads, displayed a slight decrease in the ultimate tensile strength (UTS) for temperatures exceeding 50 °C. The UTS dropped by 6% for 70 °C and by 8.9% for the 90 °C. The 50 °C, 70 °C, and 90 °C specimens showed an increase of Young's modulus (E) by 12.0%, 7.5%, and 8.2% respectively. The 0.2% offset yield stress ( $\sigma_y$ ) for 50 °C decreased by 7.2%. While the 70 °C and 90 °C increased by 7.5% and 11.9% respectively.

**Table 13** ABS\_XY average and standard deviation of properties.

| ABS_XY Specimen Properties |              |             |                  |
|----------------------------|--------------|-------------|------------------|
| Testing Temperature (MPa)  | UTS (MPa)    | E (GPa)     | $\sigma_y$ (MPa) |
| Room Temp.                 | 39.32 ± 1.87 | 2.08 ± 0.27 | 26.66 ± 6.77     |
| 50°C                       | 39.61 ± 0.85 | 2.33 ± 0.14 | 24.75 ± 5.34     |
| 70°C                       | 36.96 ± 1.63 | 2.24 ± 0.31 | 28.67 ± 5.89     |
| 90°C                       | 35.82 ± 1.22 | 2.25 ± 0.17 | 29.84 ± 6.00     |

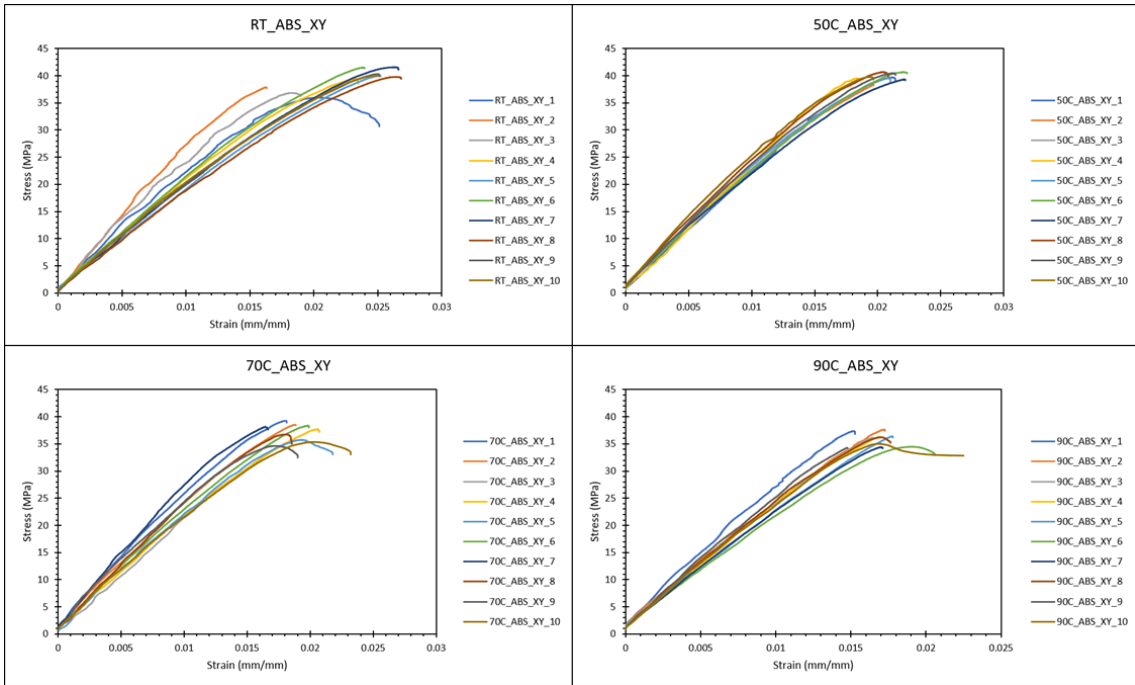


**Figure 41** Stress-Strain curves for ABS specimens printed in the XY orientation.

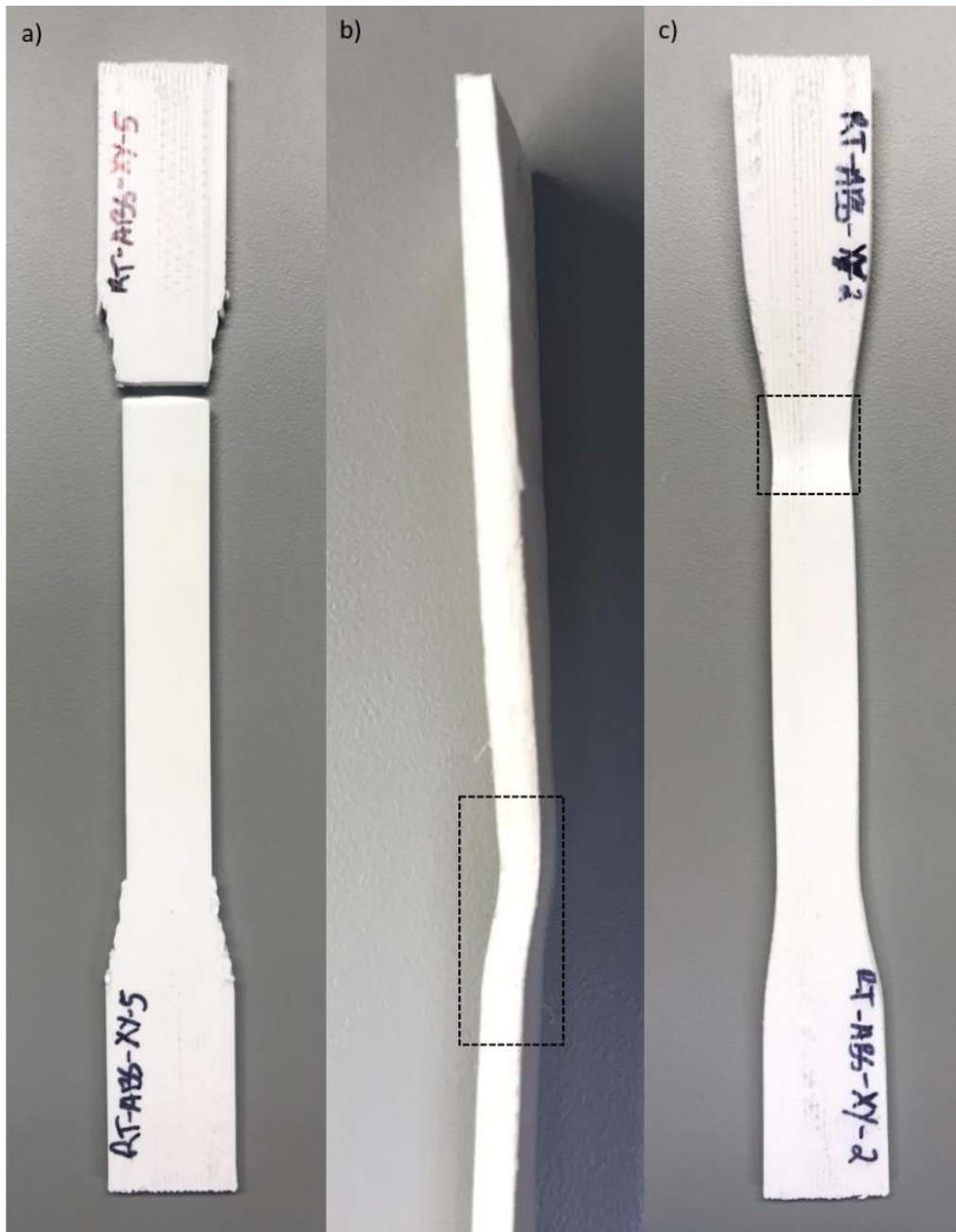


**Figure 42** a) typical break of the specimen set. b-c) Demonstrating failure to break but a bow below the fillet region in RT\_ABS\_XY\_2

The specimens tested at room temperature, approximately 25 °C, all broke at the intersection of the fillet region and gauge length, as shown in **Figure 42a**. Specimen RT\_ABS\_XY\_2 did not break but bowed slightly below the fillet region **Figure 42b-c**. This deformation did not affect the UTS or  $\sigma_y$  but this specimen had the largest E of the group.

A majority of the 50 °C specimens broke similarly to the room temperature specimens. However, two specimens broke higher up in the fillet region. Specimen 50C\_ABS\_XY\_8 broke in a Z type line displayed in **Figure 43**. Specimen 50C\_ABS\_XY\_9 broke higher in the grip section. Neither specimen showed an effect in the properties caused by these dissimilar failures.

Similar to the previous specimens most of the 70 °C specimens broke below the fillet region. Two specimens failed in a different manner, demonstrating similar failures as seen in the 50 °C specimens. Specimen 70C\_ABS\_XY\_2 failed in the grip akin to 50C\_ABS\_XY\_9, and specimen 70C\_ABS\_XY\_8 failed the same as 50C\_ABS\_XY\_8. No effect on the properties was observed due to the different failure locations.

The 90 °C specimens failed similar to the others with only one different failure type among the specimens. Specimen 90C\_ABS\_XY\_10 fractured in two locations, below the fillet region and in the gauge, but did not break through the entire gauge width. This specimen demonstrated a UTS and E consistent with the other specimens in this group but resulted in a lower  $\sigma_y$ . The double fracture allowed the specimen to maintain loading for an extended time, as seen in **Figure 41**. The failed specimen is displayed in **Figure 44**.



**Figure 43** a) Failure in Z shape pattern within the fillet region. b) Highlighted (black dashed line) Z shape failure pattern.



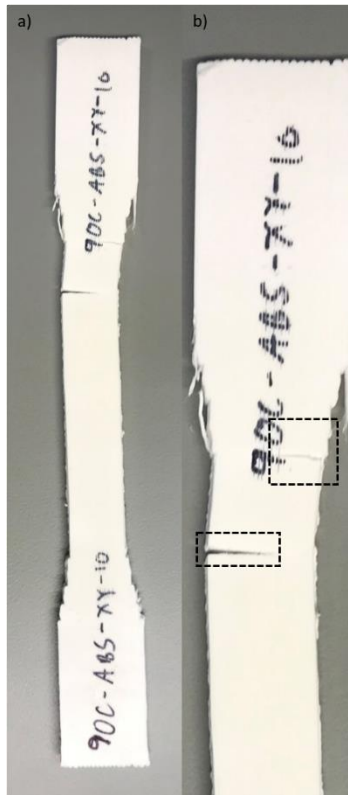


**Figure 44** a) 90C\_ABS\_XY-10 undergoing fracture that does not extend through the width of the specimen. b) Black dashed line boxes highlight the double fracture in specimen 90C\_ABS\_XY\_10.

## ABS\_YX

The averages and standard deviations for the test results of the ABS\_YX specimens are provided in **Table 14**, with the stress versus strain data displayed in **Figure 45**. These specimens were loaded perpendicular to the bead-to-bead interface and demonstrated an increase in the UTS relative to room temperature by 7.9% and 1.5% for 50 °C and 70 °C respectively. However, the 90 °C specimens had the lowest UTS and decreased from room temperature results by 6.0%. The E increased with temperature above 50 °C. The E of the 70 °C and 90 °C specimens increased by 2% and 8.5% respectively. The  $\sigma_y$  increased for the higher test temperatures. The 90 °C specimens had the lowest average and the 70 °C had the highest.

The improvement of the yield stress present in the YX specimen testing after exposure to high temperatures, particularly at 50 °C, is uncertain due to several contributing factors, including the inherent variability in FFF parts, yield stress calculation, and the heat treatment effects on the specimen. FFF parts demonstrate a high amount of variability in mechanical properties, and this variability was particularly evident in the baseline testing of the YX specimens at room temperature.

**Table 14** ABS\_YX average and standard deviation of properties.

| ABS_YX Specimen Properties |              |             |                  |
|----------------------------|--------------|-------------|------------------|
| Testing Temperature        | UTS (MPa)    | E (GPa)     | $\sigma_y$ (MPa) |
| Room Temp.                 | 27.18 ± 4.30 | 2.00 ± 0.45 | 19.96 ± 3.81     |
| 50°C                       | 28.24 ± 3.44 | 2.00 ± 0.21 | 20.34 ± 3.84     |
| 70°C                       | 27.58 ± 2.34 | 2.04 ± 0.33 | 21.19 ± 2.91     |
| 90°C                       | 25.54 ± 4.14 | 2.17 ± 0.46 | 19.19 ± 4.44     |

For this set of specimens, there were multiple specimens that exhibited significantly different stress-strain profiles. This substantial variability can cause large standard deviations in test results which create difficulties when identifying data trends. Compounding on the inherent variability for some specimens, the use of the 0.2% offset method to calculate yield stress introduced additional uncertainty into test results due to dips in the linear section of the stress-strain plots, adding difficulty in pinpointing the onset of yielding. Additionally, after the specimens are held at elevated temperature and then tested at room temperature, there is a potential for localized areas of improved interlayer adhesion induced by the heat treatment. Because of the reliance of the interlayer adhesion on strength for the YX specimens, this improved interbead adhesion would have a larger effect on these specimens than on XY specimens. It is unlikely that there is a significant effect in the adhesion at a 50 °C heat treatment, being a lower temperature relative to  $T_g$ , but the cumulative uncertainty introduced by all of these factors contributes to the high variability of the yield stress difference exhibited in YX and XY print configurations.

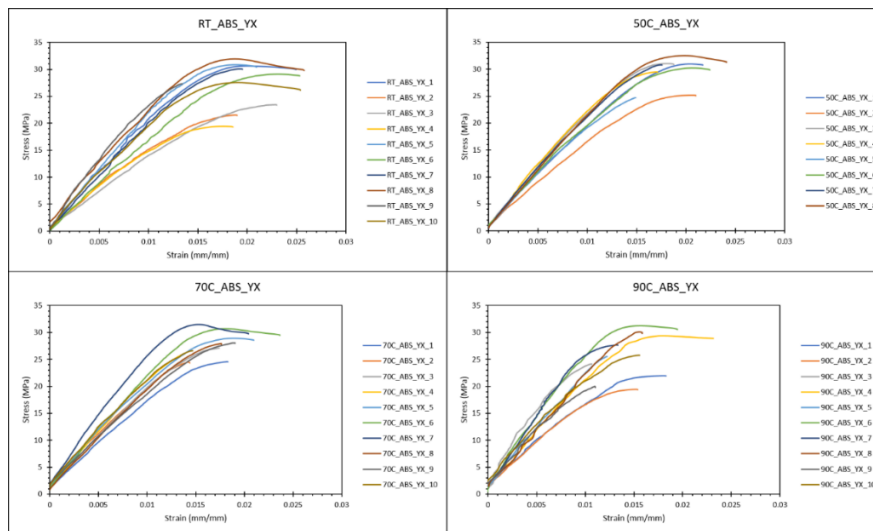


**Figure 45** Stress-Strain curves for ABS specimens printed in the YX orientation

The room temperature specimens failed consistently in the gauge length with the majority of the specimens failing within a 7 mm range along the specimen length. Two specimens broke outside of this range, specimen RT\_ABS\_YX\_3 and specimen RT\_ABS\_YX\_10. These specimens failed closer to the fillet region, but still within the gauge length. No discernible effects on the properties were observed from these failures. All of the specimens failed in a stepwise manner. A long failure presented itself between two layers with a jump across a layer towards the edge of the specimen, as shown in **Figure 46**.

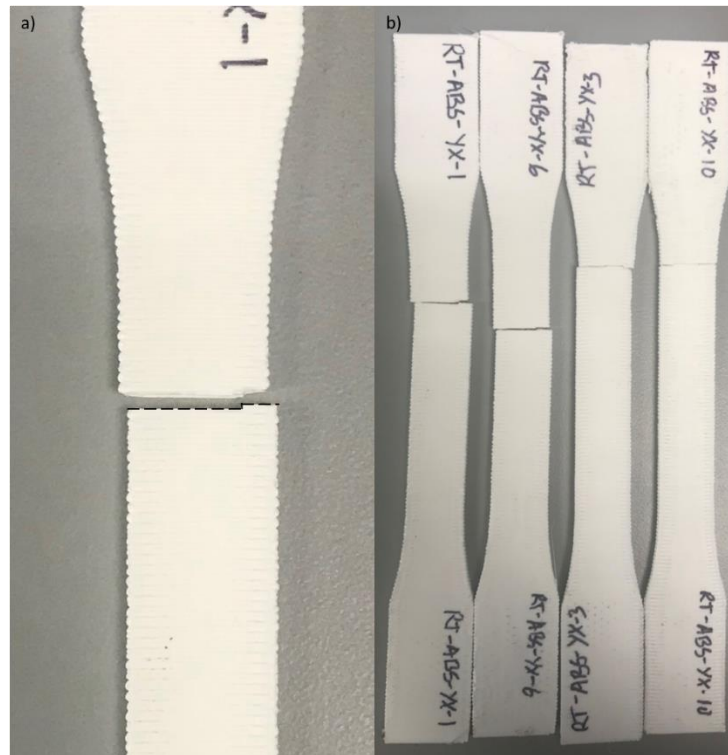


**Figure 46** a) Stepwise break pattern observed in specimens [dashed black line]. b) Left two specimens show typical range of breakage in the gauge, right two specimens were outliers.

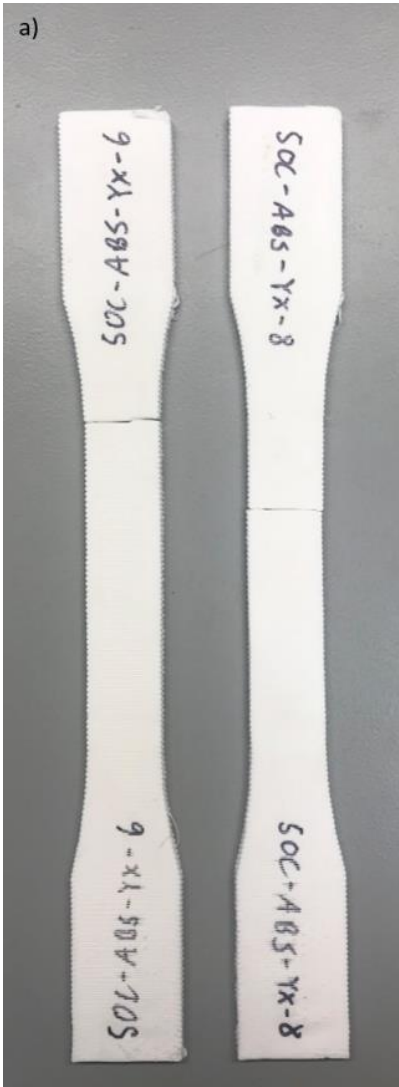


**Figure 47** a) *Specimens illustrating different break locations.*

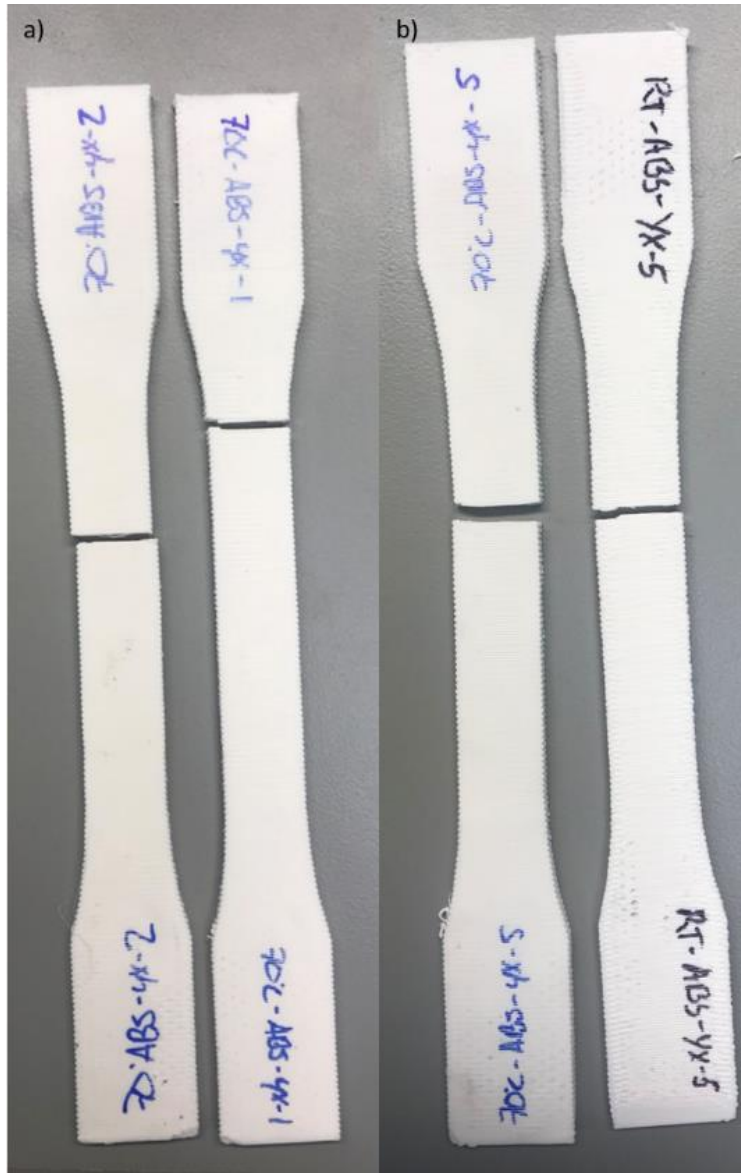


**Figure 48** a) Specimens illustrating different break locations. b) Specimens illustrating different step sizes between 70C and room temperature.

The 50 °C specimens failed with a larger variation in location within the gauge length and exhibited two distinct groups. They either failed within the center of the gauge or slightly higher. However, no effects on the properties were correlated with the failure location. Similar to the room temperature specimens, the failures observed were stepwise with a break between two layers and a small break across a layer near the edge of the cross-section. Specimen 50C\_ABS\_YX\_2 had the lowest E but displayed no observable defects.

The 70 °C specimens also displayed two failure locations, towards the upper quarter of the gauge or below the fillet region, shown in **Figure 47**. No effects on mechanical properties were observed with respect to the different break locations. This is illustrated in **Figure 45** where specimen 70C\_ABS\_YX\_1 and specimen 70C\_ABS\_YX\_8 had breaks below the fillet region but fall in at the lowest E and near the center respectively. The fracture path was similar to that observed in the room temperature and 50 °C specimens, but the final step across the layer was reduced in length as shown in **Figure 48**.

The 90 °C specimens all failed within a 13 mm region in the upper gauge. Regardless of the break location, no effect on the properties was distinguishable between the break locations. However, the data generated for this specimen set showed larger variation than the other ABS\_YX temperature sets, as shown in **Figure 45**. Specimen 90C\_ABS\_YX\_1 and specimen 90C\_ABS\_YX\_2 displayed the lowest E among the set, but not the lowest UTS or  $\sigma_y$ . Specimen 90C\_ABS\_YX\_9 also failed at a lower strain and stress values than the other specimens in the set.

## **CF-ABS\_XY**

The average and standard deviation of the properties for the CF-ABS\_XY specimens are displayed in **Table 15**, with the stress versus strain data provided in **Figure 49**. CF-ABS\_XY specimens showed an increase in the UTS with temperature. The UTS increased by 0.2%, 7.3%, and 14.9% at the 50 °C, 70 °C, and 90 °C temperatures respectively. This trend was not observed in the E or the  $\sigma_y$  however. The 50 °C specimens had a decrease in both the E and the  $\sigma_y$  by 7.9%. 70 °C and 90 °C conditioned specimens increased the E and the  $\sigma_y$  by 28% and 6.1% respectively.

The RT\_CF-ABS\_XY specimens were utilized to study the effect of sanding on the shoulders, as shown in **Figure 50**. Specimen RT\_CF-ABS\_XY\_1 was sanded down, specimen RT\_CF-ABS\_XY\_2 was left unfiled, and specimen RT\_CF-ABS\_XY\_3 was sanded to a lesser extent than that of specimen RT\_CF-ABS\_XY\_1, as seen in **Figure 50**. As illustrated in **Figure 49**, these three specimens exhibited different behavior than the rest of the data and failed prematurely. The UTS of these specimens demonstrated that sanding of the specimens resulted in no significant differences. The failure locations for all of the specimens regardless of surface preparation were below the fillet region. Specimen RT\_CF-ABS\_XY\_5 and RT\_CF-ABS\_XY\_8 behaved differently than the rest of the specimens and had the lowest UTS, E, and  $\sigma_y$  among the set. Specimen RT\_CF-ABS\_XY\_5 was not sanded and specimen RT\_CF-ABS\_XY\_8 was sanded. This comparison again shows that sanding did not influence the properties.



**Table 15** CF-ABS\_XY average and standard deviation of properties.

| CF-ABS_XY Specimen Properties |              |             |                  |
|-------------------------------|--------------|-------------|------------------|
| Testing Temperature (MPa)     | UTS (MPa)    | E (GPa)     | $\sigma_y$ (MPa) |
| Room Temp.                    | 39.93 ± 5.70 | 5.73 ± 1.77 | 11.46 ± 3.53     |
| 50°C                          | 39.84 ± 3.98 | 5.28 ± 0.68 | 10.55 ± 1.36     |
| 70°C                          | 37.03 ± 1.99 | 7.34 ± 1.10 | 14.67 ± 2.20     |
| 90°C                          | 34.00 ± 5.04 | 6.08 ± 2.07 | 12.16 ± 4.14     |

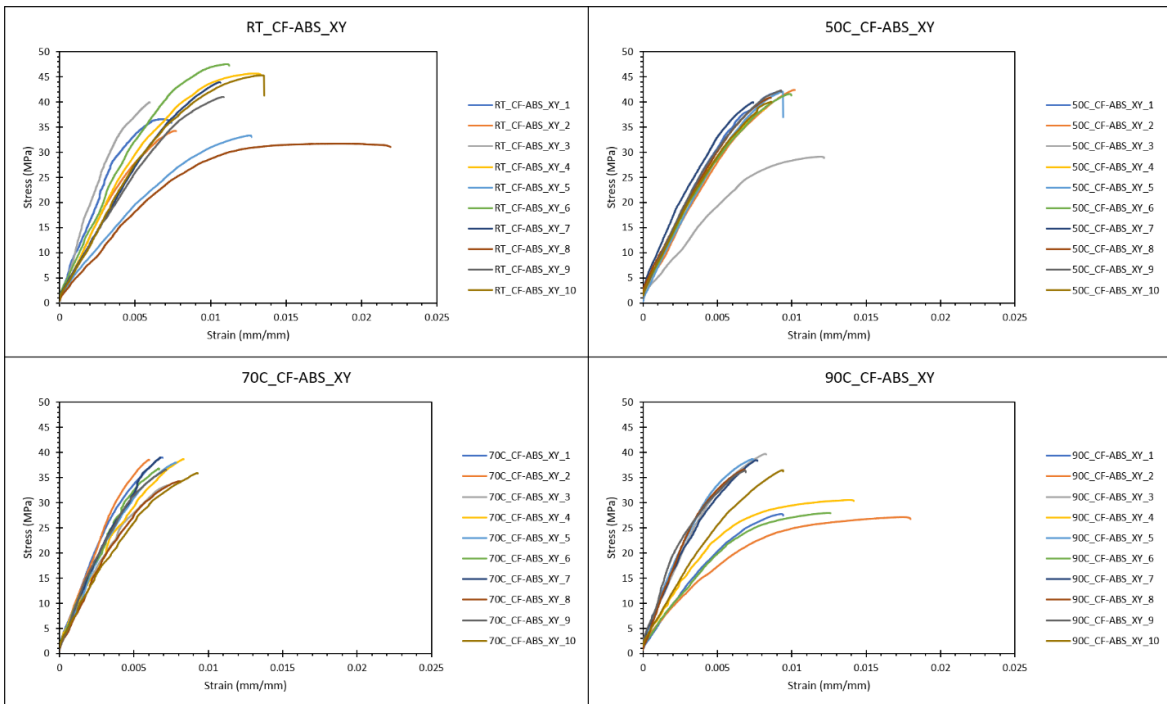


**Figure 49** Stress-Strain curves for CF-ABS specimens printed in the XY orientation.



**Figure 50** a) Specimens showing the filing, non-filing, and reduced filing. b) Outlier specimens in the test set.



**Figure 51** Typical break location of test set (left), outlier specimen (middle), gauge length break (right).

The 50C\_CF-ABS\_XY specimens broke below the fillet region similarly to the room temperature specimens, except for specimen 50C\_CF-ABS\_XY\_10 which failed in the gauge length. However, this specimen did not have different mechanical properties. The only outlier in the data set occurred with specimen 50C\_CF-ABS\_XY\_3 which resulted in a lower UTS, E, and  $\sigma_y$ , (**Figure 49**). **Figure 51** illustrates the normal failure location, the outlier specimen 50C\_CF-ABS\_XY\_3, and the gauge length failure in specimen 50C\_CF-ABS\_XY\_10.

The 70C\_CF-ABS\_XY specimens failed below the fillet region with no exceptions and showed a low standard deviation in the UTS. However, there was a large difference in the E and  $\sigma_y$  of the set. Specimen 70C\_CF-ABS\_XY\_10 showed a significant decrease in the E and  $\sigma_y$ .

The 90C\_CF-ABS\_XY specimens also broke below the fillet region. Unlike the 70C\_CF-ABS\_XY specimens, this set's data displayed two distinct groups, seen in **Figure 49**. Specimens 90C\_CF-ABS\_XY\_1, 90C\_CF-ABS\_XY\_2, 90C\_CF-ABS\_XY\_4, and 90C\_CF-ABS\_XY\_6 resulted in lower UTS, E, and  $\sigma_y$ . Specimen 90C\_CF-ABS\_XY\_1 displayed two breaking locations for different print layers, as shown in **Figure 52**.



**Figure 52** a-b) Multi-layered failure exhibited by specimen 90C\_CF-ABS\_XY\_1, dashed white lines illustrate layer separation.

## **CF-ABS\_YX**

The averages and standard deviations of the test results for CF-ABS\_YX specimens are provided in **Table 16**, with the stress versus strain plots displayed in **Figure 53**. CF-ABS\_YX specimens demonstrated the lowest UTS of the testing groups. A decrease in the E and  $\sigma_y$  was observed with an increase in temperature. The E decreased by 7.7%, 6.0%, and 2.6%, and the  $\sigma_y$  decreased by 19.9%, 6.8%, and 5.9% for 50 °C, 70 °C, and 90 °C respectively. This constant drop in properties with an increase of conditioning temperature was not observed with regard to the UTS where both the 50 °C and 90 °C decreased by 3.9% and the 70 °C specimens decreased by 7.5%.

The majority of the RT\_CF-ABS\_YX specimens failed in the center of the gauge length. Specimen RT\_CF-ABS\_YX\_2 and specimen RT\_CF-ABS\_YX\_4 failed higher in the gauge length, while specimen RT\_CF-ABS\_YX\_9 failed at the intersection of the fillet region and the gauge section. However, no effects on the properties could be related to the failure location.

The 50C\_CF-ABS\_YX specimens mainly failed in the upper section the gauge length, two specimens broke lower towards the center of the gauge length, specimen 50C\_CF-ABS\_YX\_1 and specimen 50C\_CF-ABS\_YX\_4. These two specimens, along with specimen 50C\_CF-ABS\_YX\_3, had the lowest  $\sigma_y$  of the set. However, only specimen 50C\_CF-AS\_YX\_1 displayed a lower E. The UTS of the specimens was not affected. This set also displayed a stepwise failure along the gauge width, with a small section where the break shifted over a layer. The different failure locations can be seen in **Figure 54a**), and the break pattern can be seen in **Figure 54b**).

**Table 16** CF-ABS\_YX average and standard deviation of properties.

| CF-ABS_YX Specimen Properties |              |             |                  |
|-------------------------------|--------------|-------------|------------------|
| Testing Temperature (MPa)     | UTS          | E (GPa)     | $\sigma_y$ (MPa) |
| Room Temp.                    | 24.09 ± 0.97 | 3.49 ± 0.64 | 22.37 ± 1.79     |
| 50°C                          | 23.17 ± 1.55 | 3.22 ± 0.59 | 17.92 ± 3.70     |
| 70°C                          | 22.29 ± 1.41 | 3.28 ± 0.33 | 20.86 ± 2.25     |
| 90°C                          | 23.14 ± 0.76 | 3.40 ± 0.57 | 21.04 ± 3.32     |

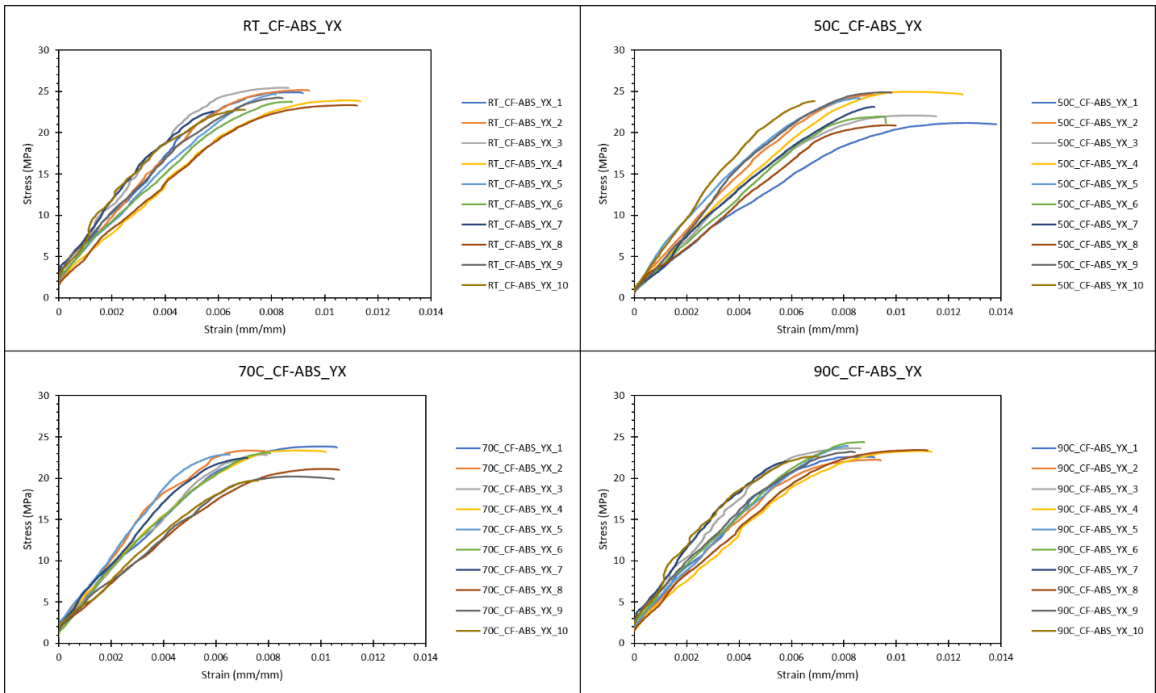


**Figure 53** Stress-Strain curves for CF-ABS specimens printed in the YX orientation.



**Figure 54** a) *Different break locations on specimens.* b) *typical break pattern.*



**Figure 55** *Different break locations on specimens.*



70C\_CF-ABS\_YX specimens had three distinct failure locations; below the fillet region, in the upper section of the gauge length, and towards the center of the gauge, as seen in **Figure 55**. However, no distinguishable differences in the properties were observed based on the failure locations. Specimen 70C\_CF-ABS\_YX\_10 showed the lowest UTS and  $\sigma_y$  of the test set. The specimens displayed a similar stepwise break along the gauge width.

The 90C\_CF-ABS\_YX specimens all failed in the upper section of the gauge length, with specimen 90C\_CF-ABS\_YX\_4 failing closest to the gauge center. Specimen 90C\_CF-ABS\_YX\_4 and specimen 90C\_CF-ABS\_YX\_8 displayed the lowest E of the test set and were 23.1% and 20.9% off from the average E. Specimen 90C\_CF-ABS\_YX\_1 had the lowest  $\sigma_y$  and was significantly lower than the average. The specimens for this test set also displayed the stepwise break pattern observed in the other test sets.

### ***Moisture Effects Test***

Previous studies on moisture effects of pure FFF ABS demonstrated significant effects on tensile strength.<sup>23,24</sup> Moisture laden composite test specimens, CF\_ABS, also demonstrated substantial effects including increased variability and a reduction in the overall ultimate tensile stress and the extension to break, compared to the specimens stored under ambient conditions. Saturated test specimens extracted in the YX direction were extremely weak with an average UTS of less than 5 MPa, compared to 10 MPa for ambient YX specimens, and failed at loads below the calibrated range of the load cell. The CF\_ABS\_XY specimens tested at ambient moisture conditions exhibited repeatability, while a pronounced increase in variability under wet conditions is seen in **Figure 56**. One test specimen failed outside the gauge length, CF\_ABS\_XY\_WET\_4, and the results for this specimen were considered invalid.

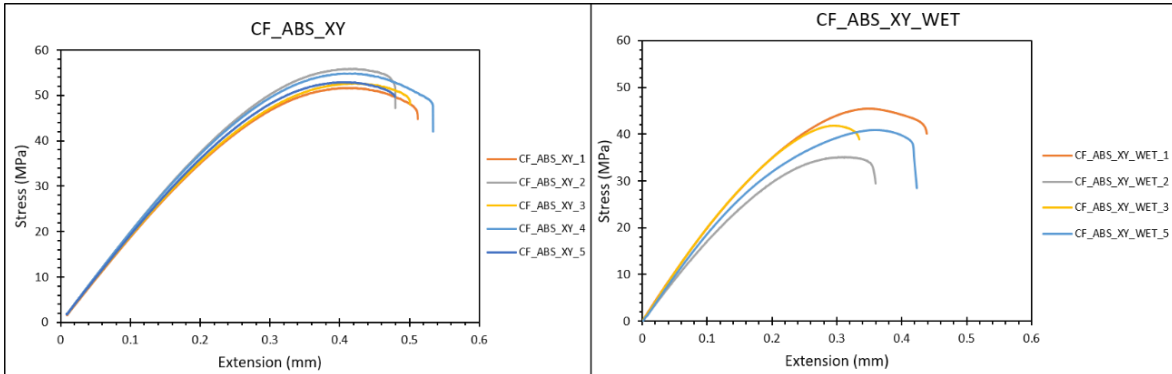


**Figure 56** *CF\_ABS\_XY* tested under ambient moisture conditions and soaked to capacity and tested.

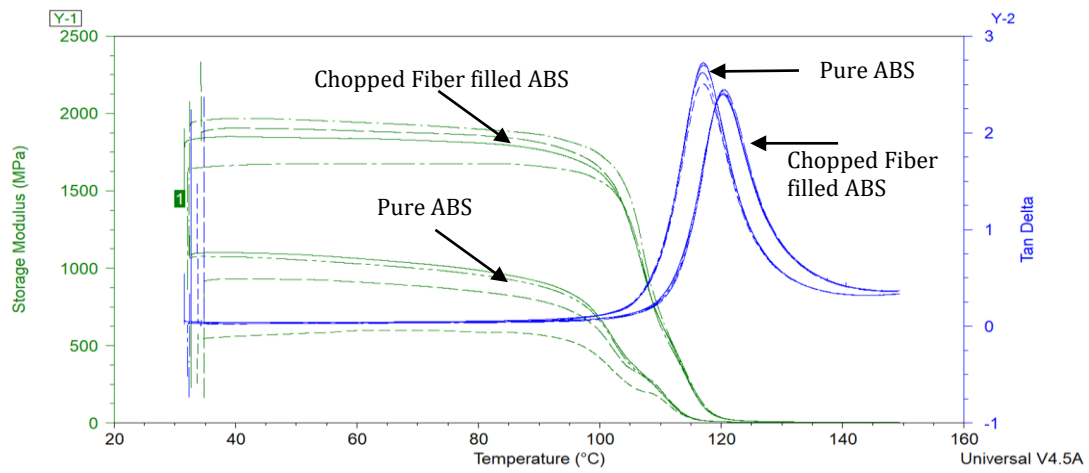


**Figure 57** *Dynamic Mechanical Analysis of ABS and chopped fiber filled ABS*

**Table 17** Mean and standard deviation of the  $T_g$  calculated three ways based on the storage modulus ( $E'$ ), the loss modulus ( $E''$ ), and the tan delta.

| DMA $T_g$ |                             |                              |                                  |
|-----------|-----------------------------|------------------------------|----------------------------------|
|           | $E'$ ( $^{\circ}\text{C}$ ) | $E''$ ( $^{\circ}\text{C}$ ) | Tan Delta ( $^{\circ}\text{C}$ ) |
| ABS<br>CF | $102.81 \pm 0.84$           | $114.29 \pm 0.20$            | $120.22 \pm 0.12$                |
| ABS       | $96.45 \pm 0.46$            | $110.86 \pm 0.25$            | $117.01 \pm 0.05$                |

## Discussion

### *Temperature Effects*

Overall, the test results show that increasing the conditioning temperature causes a small reduction in the UTS and a consistent reduction in the failure strain, with observable trends in the break location isolated to the print orientation and no correlation to the testing temperature. Variability was observed with increasing temperature in the appearance of the stress versus strain curves, where higher temperatures were less linear in nature due to the polymer softening. In order to further explore this behavior, DMA was performed to evaluate the  $T_g$  range for the onset of mechanical degradation and other physical phenomena.

In the DMA testing, the rapid decrease in the  $E'$  is the  $T_g$  used in guidelines outlined by Foley et. al. for use in naval applications of composites and is referred to as the DMA  $T_g$ .<sup>13</sup> The DMA  $T_g$ , is directly related to a drop in the elastic modulus, where the material becomes more compliant and is considered the onset of mechanical degradation. The consistent reporting of the  $T_g$  from the material supplier and in literature is around  $105\text{ }^{\circ}\text{C}$ , however the use of DMA  $T_g$  may be more critical in the evaluation of material allowables. In the case of the FFF DMA specimens, the DMA  $T_g$  was  $102.81\text{ }^{\circ}\text{C}$  for CF-ABS and was  $96.45\text{ }^{\circ}\text{C}$  for ABS,

much lower than the reported 105 °C for the bulk material property, shown in the comparison in **Figure 57**.

The  $T_g$  associated with each of the DMA  $T_g$  calculations is shown in **Table 17**. Here the mean and standard deviation are reported for a set of 4 specimens tested for each material. These values provide the onset of mechanical degradation, the temperature of the change in bulk segmental chain motion, and the mid-point of the glassy-to-rubbery transition. Beyond the DMA  $T_g$  the polymer begins to undergo the change from a glassy-state, through a leathery-state, and into a rubbery-state. This transition categorizes the response of the material to mechanical load and is strain rate dependent. Under the loading conditions used in the uniaxial tension testing, the relatively low strain rate, coupled with the elevated temperature, resulted in polymer chain motion related to viscous flow and eventual polymer fracture.

Ultimately the overarching trend for the higher temperature tensile tests follows a substantially decreasing strain to break, but only a small decrease in the ultimate tensile strength. This trend is consistent with the polymer dynamics described in the previous section. As the polymer heats up, the material undergoes a viscous flow type behavior that yields to polymer fracture. The UTS of the polymer doesn't decrease drastically due to the physical nature of the polymer chain structure, however as the temperature increases towards the  $T_g$ , the polymer chains can more easily slide past each other. When the polymer chains slide past each other there is less ability for the structure to hold load, and the load is more directly applied to individual polymer chains. The interfacial layers in the FFF structure derive strength from the physical crosslinking, or entangling, of the polymer chains. This structure at room temperature is locked into place and the friction and entanglement provides the load bearing nature. When the temperature is elevated, the polymer chains begin to slide and move, causing the failure at lower extensions and slightly lower ultimate tensile strength.

In the case of the 50 °C test temperature, there appears to be a slight increase in the strength potentially due to an annealing effect at this temperature. This effect causes a slight increase in the mobility of the polymer chains to promote better polymer entanglement, but without too high of a mobility to cause the polymer chains to be able to slide past each other more readily. Annealing is likely, but with the 50 °C test temperature the effects of any reduction in heat would have a larger impact on chain mobility than at higher temperatures. A fully enclosed test chamber with precision temperature control is needed to delineate the annealing effect in this temperature range, where existing variability from the FFF process may overshadow the temperature effect.

With the addition of carbon fiber, the overall trend of decreased strain to break is again evident, however due to the high thermal conductivity of the carbon fibers there is better layer adhesion,<sup>30</sup> corroborated in **Figure 58**. The increased layer adhesion may lead to a better entropic conformation which creates a higher likelihood of the polymer chains being able to then slide past each other. If the polymer chains are quenched into the deposited conformation, they generally behave in a more brittle fashion with increased strength and decreased elongation to break. If the polymer is fully annealed, then there is a decrease in the ultimate tensile strength but an increase in the toughness of the material with an increased elongation to break. If the polymer chains are partially annealed due to the carbon fiber content, then these are more likely to be able to slide past each other under increased environmental temperatures reducing the strength of the mechanical crosslinking and the strain to break. The addition of carbon fibers creates a more brittle material overall due to void content increases, as well as the initiation sites around the fibers.

The E" based  $T_g$  of 110 °C and 114 °C, for ABS and ABS/CF respectively, demonstrate the temperature in which the physical properties begin to change as it relates to the glass transition. This physical change is the onset of long-range segmental motion in the polymer chains, where parts of the polymer chains are

able to displace and rotate. In regard to mechanical testing, at this temperature and beyond, the polymer chains are able to move in such a way as to reduce the amount of load distributed to the entire specimen.

The response of the printed parts to temperatures exceeding DMA  $T_g$  indicated large relaxations in the material. Significant shape changes occurred in the specimens when heated to 110 °C and beyond. The shape changes observed, in **Figure 59**, could be a result of reaching and exceeding the annealing temperature associated with the material. In the case of FFF, shear stresses occur in the material during deposition where the cooler previous layer acts as a source of friction for the newly deposited layer. The specimens were printed in ambient air conditions and due to the rapid cooling, some of these shear stresses remain trapped in the material. In this case, annealing isn't the goal, however the term is used here to describe the process of the polymer chains relaxing based on previous stresses. The material shape change was predicated on the direction the material was deposited where the polymer chains contract along the deposition line. This contraction shortened the printed bead lengths and increased the bead widths, which increases the number of polymer chain conformations inside the part and increases the overall entropy of the deposited material. The shape changes and associated relaxation of the polymer chains provided interesting insight into the trapped stresses and strains imparted by the printing process and should be investigated further.

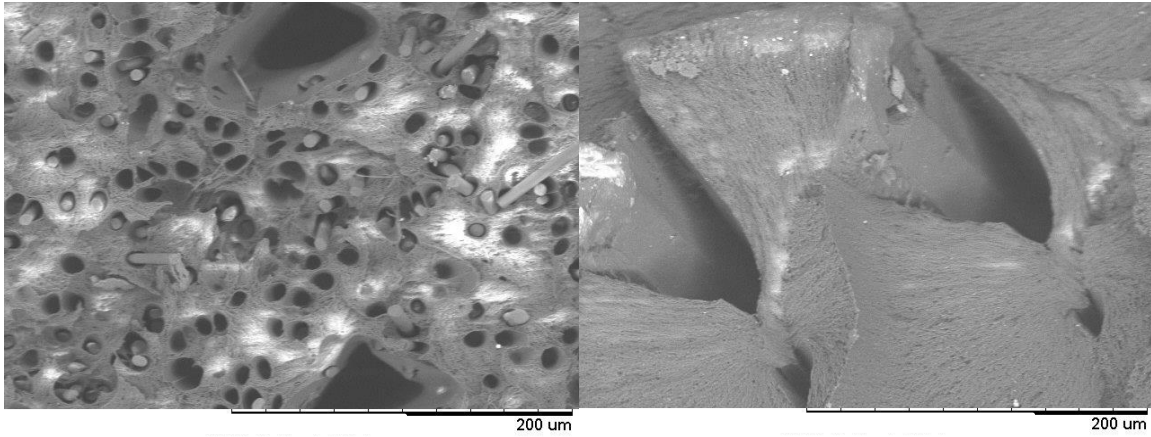


**Figure 58** *CF-ABS and ABS bead-to-bead interfaces show that carbon fiber reinforcement improves the interfacial mixing.*



**Figure 59** *Shape change associated with heating material beyond the  $T_g$  where the material expanded in the bead width and contracted in the bead length.*

## ***Moisture Effects***

ABS presents hygroscopic tendencies, where the material will absorb or adsorb water from the surrounding environment under ambient conditions. Due to the porosity inherent to the FFF process from the raster patterns, increased susceptibility to water effects was evaluated. TGA was performed after the mechanical testing to determine how much water content remained in the material after being stored in ambient conditions. Water can be absorbed into the polymeric structure but generally not in large quantities from the atmosphere alone, prompting the investigation to the amount of trapped water in the specimens due to submersion. TGA testing was performed to isolate the effects of this trapped water that can only be removed through heat or vacuum drying.

From the TGA data presented in **Figure 60**, no excess trapped water was present in the material. This conclusion can be discerned from figure 22 where there was no drop in the mass around the evaporation temperature of water. Due to the raster-based porosity being internal to the specimen, water uptake is limited to the bulk material itself, and any large raster pores would act as a two-way absorption and evaporation pathway. The test specimens were printed with 100% infill for consistent mechanical evaluation, however any part or test specimen printed without a 100% infill may provide different results for mechanical evaluation and residual water content.



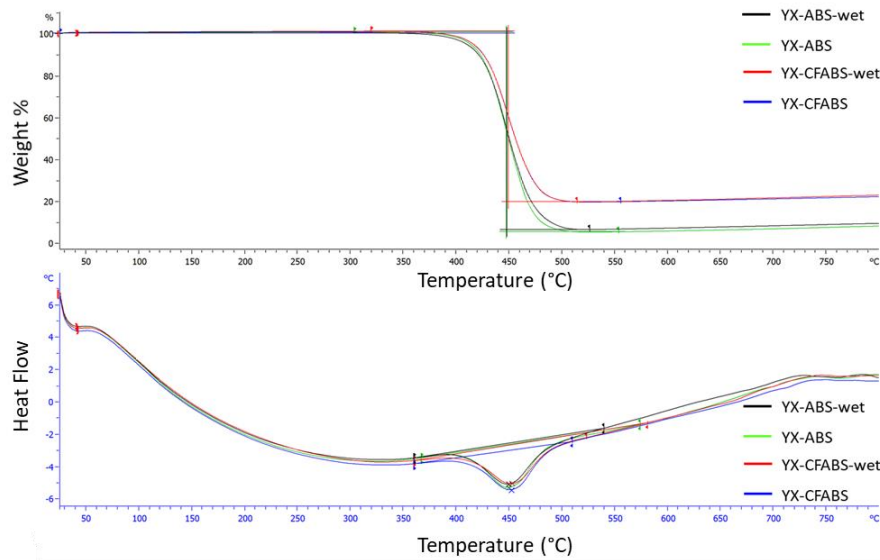


**Figure 60** TGA analysis of specimens subjected to moisture versus those under ambient atmosphere demonstrating negligible amounts of trapped water.

Despite the apparent availability of moisture to absorb into and evaporate out of the sample, moisture has a large impact on the variability and elongation to break of these specimens. Multiple orientations were tested but due to the variability associated with the small print type and the brittle nature of plaque printed specimens in the YX direction/configuration, these specimens were omitted. Differentiating moisture effects was not possible with YX specimens and subsequently moisture effects were only analyzed with XY specimens. Molecular degradation could be the cause of the increased variability and reduction of strength in the water-soaked test specimens. It is likely that, even though the water can be absorbed and then evaporated, water exposure rather than just water content causes decreased mechanical performance. Further evaluation of moisture effects is needed at a microstructural level in hygroscopic polymeric FFF parts.

## Conclusions

The effect of heat and moisture on the ultimate tensile strength of fiber reinforced and unreinforced ABS was evaluated within the scope of qualification of polymeric FFF materials. It was found that as the tensile specimens were conditioned at temperatures approaching the  $T_g$ , the polymer chain dynamics dictated a slight reduction in the ultimate tensile strength and a significant change in the elongation to break. This finding was consistent between both fiber reinforced and unreinforced polymer systems. In the fiber reinforced specimens, the interfacial bonding was increased due to the increased thermal conductivity provided by the carbon fibers. This provides a decrease in variability but also allows the polymer chains to move more freely past one another at temperature, further reducing the elongation to break. At temperatures of roughly 50% of the  $T_g$ , no significant changes in material response to load were observed, providing a potential boundary for the operating temperatures. Specimens subjected to moisture demonstrated an increase in variability and a reduction in tensile strength and elongation to break. However, no trapped water in the voids was found after subjecting the specimens to ambient conditions prior to analysis. Future use of deformation analysis techniques could provide more refined insights into the effects of heat and moisture on material behavior under load.<sup>31-40</sup>

## Acknowledgments

Financial support was provided by the Naval Education Engineering Consortium, grant N00174-16-C0033, under the direction of Dr. Maureen Foley at the Naval Surface Warfare Center Carderock Division.

## References

1. Cole, D. P., Riddick, J. C., Iftekhar Jaim, H. M., Strawhecker, K. E. & Zander, N. E. Interfacial mechanical behavior of 3D printed ABS. *J. Appl. Polym. Sci.* 133, 1–12 (2016).
2. Boschetto, A. & Bottini, L. Accuracy prediction in fused deposition modeling. 913–928 (2014). doi:10.1007/s00170-014-5886-4
3. Torrado, A. R. et al. Characterizing the effect of additives to ABS on the mechanical property anisotropy of specimens fabricated by material extrusion 3D printing. *Addit. Manuf.* 6, 16–29 (2015).
4. Zhu, Z., Dhokia, V. & Newman, S. T. Application of a hybrid process for high precision manufacture of difficult to machine prismatic parts. 1115–1132 (2014). doi:10.1007/s00170-014-6053-7
5. Brenken, B., Barocio, E., Favaloro, A., Kunc, V. & Pipes, R. B. Fused filament fabrication of fiber-reinforced polymers: A review. *Addit. Manuf.* 21, 1–16 (2018).
6. Uriondo, A., Esperon-Miguez, M. & Perinpanayagam, S. The present and future of additive manufacturing in the aerospace sector: A review of important aspects. *Proc. Inst. Mech. Eng. Part G J. Aerosp. Eng.* 229, 2132–2147 (2015).
7. Klippstein, H., Diaz De Cerio Sanchez, A., Hassanin, H., Zweiri, Y. & Seneviratne, L. Fused Deposition Modeling for Unmanned Aerial Vehicles (UAVs): A Review. *Adv. Eng. Mater.* 20, 1–17 (2018).
8. Schmid, M., Wollecke, F. & Levy, G. Long-term Durability of SLS Polymer Components under Automotive Application Environment. in ETH Zurich (2012). doi:10.3929/ETHZ-B-000225616
9. Rankin, T. M. et al. Three-dimensional printing surgical instruments: are we there yet? *J. Surg. Res.* 189, 193–197 (2014).
10. Dikshit, V. et al. Investigation of quasi-static indentation response of inkjet printed sandwich structures under various indenter geometries. *Materials (Basel)*. 10, (2017).

11. Dikshit, V. et al. Investigation of out of plane compressive strength of 3D printed sandwich composites. *IOP Conf. Ser. Mater. Sci. Eng.* 139, (2016).
12. Yap, Y. L. & Yeong, W. Y. Shape recovery effect of 3D printed polymeric honeycomb: *Virtual Phys. Prototyp.* 10, 91–99 (2015).
13. Foley, M. E. & Hart, D. C. Guidelines for Developing and Inserting Material Properties into the Code 65 Composite Material Database by. *Nav. Surf. Warf. Cent. Carderock Div.* (2011).
14. Zhong, W., Li, F., Zhang, Z., Song, L. & Li, Z. Short fiber reinforced composites for fused deposition modeling. *Mater. Sci. Eng. A301* 301, 125–130 (2001).
15. Weng, Z., Wang, J., Senthil, T. & Wu, L. Mechanical and thermal properties of ABS/montmorillonite nanocomposites for fused deposition modeling 3D printing. *Mater. Des.* 102, 276–283 (2016).
16. Li, N., Li, Y. & Liu, S. Rapid prototyping of continuous carbon fiber reinforced polylactic acid composites by 3D printing. *J. Mater. Process. Technol.* 238, 218–225 (2016).
17. Gray, R. W., Baird, D. G. & Helge Bøhn, J. Effects of processing conditions on short TLCP fiber reinforced FDM parts. *Rapid Prototyp. J.* 4, 14–25 (1998).
18. Kalsoom, U., Nesterenko, P. N. & Paull, B. Recent developments in 3D printable composite materials. *RSC Adv.* 6, 60355–60371 (2016).
19. Bellini, A. & Güçeri, S. Mechanical characterization of parts fabricated using fused deposition modeling. *Rapid Prototyp. J.* 9, 252–264 (2003).
20. Rodríguez, J. F., Thomas, J. P., Renaud, J. E., Thomas, J. P. & Renaud, J. E. Mechanical behavior of acrylonitrile butadiene styrene ( ABS ) fused deposition materials . Experimental investigation. *Rapid Prototyp. J.* 7, 148–158 (2001).
21. Turner, B. N. & Gold, S. A. A review of melt extrusion additive manufacturing processes: II. Materials, dimensional accuracy, and surface roughness. *Rapid Prototyp. J.* 21, 250–261 (2015).

22. Ning, F., Cong, W., Qiu, J., Wei, J. & Wang, S. Additive manufacturing of carbon fiber reinforced thermoplastic composites using fused deposition modeling. *Compos. Part B Eng.* 80, 369–378 (2015).
23. Halidi, S. N. A. M. & Abdullah, J. Moisture and humidity effects on the ABS used in Fused Deposition Modeling machine. *Adv. Mater. Res.* 576, 641–644 (2012).
24. Kim, E., Shin, Y. J. & Ahn, S. H. The effects of moisture and temperature on the mechanical properties of additive manufacturing components: Fused deposition modeling. *Rapid Prototyp. J.* 22, 887–894 (2016).
25. Dasari, A., Yu, Z. Z., Cai, G. P. & Mai, Y. W. Recent developments in the fire retardancy of polymeric materials. *Prog. Polym. Sci.* 38, 1357–1387 (2013).
26. Li, Y. & Shimizu, H. Improvement in toughness of poly(l-lactide) (PLLA) through reactive blending with acrylonitrile-butadiene-styrene copolymer (ABS): Morphology and properties. *Eur. Polym. J.* 45, 738–746 (2009).
27. Ferrell, W. H., Clement, J. & TerMaath, S. Uniaxial Tensile Testing Standardization for the Qualification of Fiber Reinforced Plastics for Fused Filament Fabrication. *Mech. Adv. Mater. Struct.* (2019).
28. ASTM Norma. Standard Test Method for Tensile Properties of Plastics. *Annu. B. ASTM Stand.* 1–15 (2004). doi:10.1520/D0638-14.1
29. D7028-07(2015), A. Standard Test Method for Glass Transition Temperature (DMA Tg) of Polymer Matrix Composites by Dynamic Mechanical Analysis (DMA). (2015). doi:10.1520/D7028-07R15
30. Love, L. J. et al. The importance of carbon fiber to polymer additive manufacturing. *J. Mater. Res.* 29, 1893–1898 (2014).
31. Xu, X., Bureick, J., Yang, H. & Neumann, I. TLS-based composite structure deformation analysis validated with laser tracker. *Compos. Struct.* 202, 60–65 (2018).

32. Yang, H., Xu, X., Xu, W. & Neumann, I. Terrestrial Laser Scanning-Based Deformation Analysis for Arch and Beam Structures. *IEEE Sensors* 17, 4605–4611 (2017).
33. Yang, H., Xu, X. & Neumann, I. Optimal finite element model with response surface methodology for concrete structures based on Terrestrial Laser Scanning technology. *Compos. Struct.* 183, 2–6 (2018).
34. Yang, H., Omidalizarandi, M., Xu, X. & Neumann, I. Terrestrial laser scanning technology for deformation monitoring and surface modeling of arch structures. *Compos. Struct.* 169, 173–179 (2017).
35. Yang, H., Xu, X., Kargoll, B. & Neumann, I. An automatic and intelligent optimal surface modeling method for composite tunnel structures. *Compos. Struct.* 208, 702–710 (2019).
36. Xu, X., Yang, H., Zhang, Y. & Neumann, I. Intelligent 3D data extraction method for deformation analysis of composite structures. *Compos. Struct.* 203, 254–258 (2018).
37. Xu, X., Yang, H. & Nuemann, I. A feature extraction method for deformation analysis of large-scale composite structures based on TLS measurement. *Compos. Struct.* 184, 591–596 (2018).
38. Yang, H. & Xu, X. Multi-sensor technology for B-spline modelling and deformation analysis of composite structures. *Compos. Struct.* 224, (2019).
39. Xu, X., Yang, H., Augello, R. & Carrera, E. Optimized free-form surface modeling of point clouds from laser-based measurement. *Mech. Adv. Mater. Struct.* (2019). doi:10.1080/15376494.2019.1688435
40. Xu, X., Augello, R. & Yang, H. The generation and validation of a CUF-based FEA model with laser-based experiments. *Mech. Adv. Mater. Struct.* (2019). doi:10.1080/15376494.2019.1697473

**CHAPTER IV**  
**NOVEL USE OF SEMI-CIRCULAR BEND SPECIMEN FOR**  
**FRACTURE OF BAAM POLYMERS**

## **Abstract**

Evaluate a novel geometry used in the rock and asphalt world as a fracture specimen in BAAM FFF testing. Due to the intricate connections between deposition pattern and mechanical performance, it is advantageous to have as few test specimen geometries as possible for studying processing-structure-fracture performance relationships in these BAAM parts. Currently multiple different geometries are being used with testing being performed on the parts as if they were a composite laminate or as if they were a homogeneous solid. This study seeks to elucidate the nature of the parts through interlayer and intrabead fracture and evaluate the semi-circular bend specimen for use in fracture mechanics of FFF polymers.

## **Introduction**

As additive manufacturing techniques such as fused filament fabrication (FFF) make the transition from prototyping to end user part manufacturing, there has been a natural progression of literature making pushes for the standardization of mechanical testing of these parts. Through the generation of new materials and the adaptations of tensile testing standards, increased understanding of the processing-structure-performance relationships have followed as it pertains to strength and stiffness. However, due to the highly customizable mesostructures present in FFF parts there has been increased attention paid to the fracture mechanics of these parts. For FFF to truly ascend to end part manufacturing and become a staple in manufacturing spaces across the world, characterization of the fracture toughness of FFF plastics must continue to progress.

Current testing of fracture toughness of FFF plastics has primarily focused on the interlaminar and intrabead fracture toughness. These refer to the bead-to-bead and layer-to-layer resistance to crack growth and the through-bead resistance to crack growth respectively. Hart et al performed mode I, or crack tip



opening, fracture toughness tests in a three-point bend configuration utilizing the single edge notch bend (SENB) specimen.<sup>1</sup> The interlaminar and intrabead fracture toughness and crack behavior was significantly different in the acrylonitrile-butadiene-styrene that Hart et. al. tested due to the reliance on interlaminar toughness on the diffusion between the deposited beads. Several researchers have employed the double cantilever beam (DCB) specimen, which is commonly used for composite laminate parts, for mode I fracture toughness of FFF parts and had good success in obtaining fracture properties of the interlaminar region.<sup>2-5</sup> However, Arbeiter et. al. found that in a fully optimized printing condition of FFF poly-lactic acid SENB specimens that there was an increase in the fracture toughness compared to injection molded parts.<sup>6</sup> This was due to the almost indistinguishable raster patterns signifying an almost fully homogeneous part. Arbeiter et. al. noted that this was purely in the SENB specimen and not in the compact tension (CT) specimen which did not have a perfectly symmetric printing pattern.

There is currently little information currently published with regards to fracture testing of FFF parts. The wide range of tests used raises concerns of variability in the reported fracture toughness, where there isn't a clear distinction between material property testing and engineered part testing. Due to the large variation in available printing parameters and also different strategies, including print design for repeatability<sup>7</sup> or print design for optimized mixing.<sup>6</sup> Furthermore, the comparison of behavior of the polymer material used in desktop printing and Big Area Additive Manufacturing (BAAM) printing is not well established and the different printing conditions may necessitate specific fracture standards for each. Nycz et. al. performed mode I fracture testing of BAAM printed carbon fiber reinforced acrylonitrile-butadiene-styrene (CF-ABS) using the DCB specimen to investigate the effects of preheating layers.<sup>5</sup> As it pertains to standardization for fracture toughness evaluation, the DCB specimen is only able to obtain the mode I interlayer fracture toughness necessitating multiple other specimens to test for mode II, or shear, fracture and intrabead fracture.

Through the use of a semi-circular-bend specimen (SCB) in a three-point bend test configuration, a single specimen geometry can be used to determine the multiple modes and multiple regions of fracture toughness present in FFF parts. The reduction of geometry specific testing provides unity in the manufacturing of parts and the testing of parts that will provide a consistent basis for varying the processing conditions and capturing isolated effects.

## **Materials and Methods**

### ***Materials***

Acrylonitrile-Butadiene-Styrene (ABS) base polymer with 20 weight % (wt. %) carbon fiber reinforcement was printed through the Big Area Additive Manufacturing (BAAM) system at Oak Ridge National Lab. The BAAM utilizes polymer pellets and a single screw extruder to melt and homogenize the polymer before the deposition. The polymer is deposited onto a heated ABS based plastic sheet that is adhered to the metal heating platform to ensure part stability during the printing process. Rectangular plaques with varying sizes and printing parameters were manufactured to provide a robust test platform to elucidate the material behavior and the fracture toughness. Smaller plaques that were 0.66 m x 0.254 m x 0.04524 m, length by height by width, were printed at 220C, 230C, and 240C with a 90 second layer time. Then larger plaques that were 1.5 m x 0.254 m x 0.0381 m, length by height by width, were printed all with the same extrusion temperature but with a 2-minute, 4-minute, and 6-minute layer time.

### ***Specimen Geometry***

The SCB specimen chosen was based on the asphalt mixture cracking resistance testing standard, ASTM D8044, **Figure 61**.<sup>8-11</sup> Due to the simple nature of

manufacturing multiple geometries were tested depending on the thickness of the printed plaques.

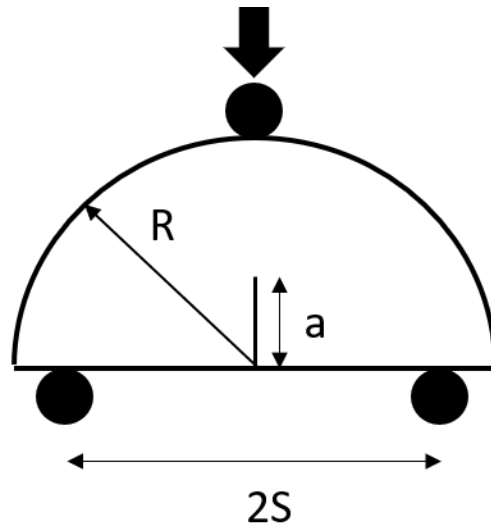


**Figure 61** SCB specimen geometry where B is width, R is radius, S is span, and a is the crack length<sup>12</sup>

In order to keep the specimens within the plane-strain criteria, the single edge notch bend (SENB) for mode I fracture toughness standard was referenced. Based on this standard, a width to thickness ratio of 1:1 up to 4:1 was considered plane strain. Based on this, a maximum thickness to width ratio of 2:1 was prepared to ensure plane-strain but minimize plastic deformation at the rollers due to compression.

For plaques printed with a 2-bead configuration, width roughly equaling 15.875 mm post printing, a specimen thickness of 33.02mm was used. This 2-bead width configuration was printed for both the 20 wt. % CF-ABS. For the 4-bead width configuration, roughly equaling 38.1 mm width, a specimen thickness of 76.2 mm was used to maintain this 2:1 ratio.

### ***Mechanical Testing***

Testing was performed on an MTS Cirterion 45 electromechanical load frame with a 10kN load cell and a 100kN load cell based on the specimen size. For the 33.02 mm radius specimens the 10kN load cell was used with a maximum load of 5kN achieved, and for the 76.2 mm radius specimens the 100kN load cell was used with a 20kN maximum load achieved. The 100kN load cell was also utilized for the SENB specimens. Testing was performed in the three-point bend configuration. Loading was applied at 0.5 mm/min.

Two orientations, **Figure 62**, were used to determine the interlayer and intrabead fracture toughness in mode I. For mode I fracture, the notch and starter crack were oriented perpendicular to the bottom of the specimen where the crack grew vertically towards the top roller. The starter crack was made with a razor blade within the notch made with a bandsaw. For interlayer  $G_{Ic}$  the layers were oriented vertically and for the intrabead  $G_{Ic}$  the layers were oriented perpendicular, **Figure 62**. The span was set to be 80% of the specimen diameter for mode I fracture to achieve the highest tensile stress at the crack tip, **Figure 61**.

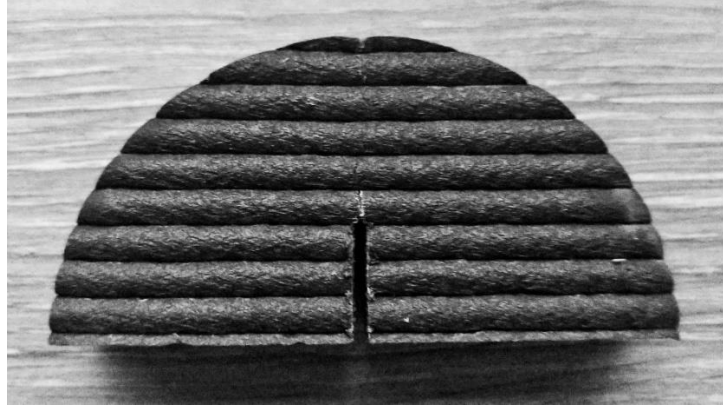


**Figure 62** Intrabead fracture SCB specimen orientation

This specimen also is capable of a mixed mode I/II testing configuration by tilting the notch at specified angles to achieve the particular loading case necessary. Multiple bead orientations were used to explore the interlayer and intralayer mixed mode fracture

### ***Fracture Theory***

Through the use of the SCB specimen the fracture toughness of the BAAM CF-ABS material was explored. For the evaluation of fracture properties in FFF materials, the variability in layer adhesion and location, as well as the development of plastic zones in the FFF parts create difficulty in consistent evaluation. In the BAAM CF-ABS material the fracture toughness was evaluated using both linear elastic fracture mechanics and elastic-plastic fracture mechanics.

#### *Linear elastic fracture*

For linear elastic materials, the critical mode I stress intensity factor  $K_{Ic}$  can be calculated using equation 1,

$$K_I = Y' \left( \frac{P\sqrt{\pi a}}{2RB} \right) \quad \text{eq 1.}$$

where P is the load, a, R, and B, are the crack length, radius, and the width, respectively. Y' is the normalized stress intensity factor for the SCB specimen and for the span to radius ratio of 0.8, which is used for mode I, can be written as:

$$Y' = 5.6 - 22.2\beta + 166.9\beta^2 - 576.2\beta^3 + 928.8\beta^4 - 505.9\beta^5 \quad \text{eq 2.}$$

where beta is the a/R ratio. Using the P maximum from the load displacement plots, the critical stress intensity factor  $K_{Ic}$  can be determined. From the  $K_{Ic}$  the critical strain energy release rate,  $G_{Ic}$  (units of J/m<sup>2</sup>) can be calculated, under the assumption of linear-elastic behavior and straight crack propagation. In the case of linear-elastic failure, the  $G_{Ic}$  can be related to the critical elastic-plastic strain energy release rate,  $J_{Ic}$  (units of J/m<sup>2</sup>) through

$$J_{Ic} = G_{Ic} = K_{Ic}^2 \left( \frac{1-\nu^2}{E} \right) \quad \text{eq 3.}$$

where E is the elastic modulus and  $\nu$  is the Poisson's ratio of the material. This relationship allows the comparison of the calculated critical stress intensity factors between ductile and brittle materials.

### *Elastic-plastic fracture*

Materials that exhibit ductility in the crack tip region cannot be analyzed using the linear elastic fracture framework. Two methods of calculating the  $J_{Ic}$  were evaluated with regards to the use of the SCB specimen on BAAM plastic specimens. The initial method was through the J calculations presented with testing of asphalt SCB specimens. This involved the comparison of the max load of SCB specimens with different initial notch depths. The linear regression of the plot of strain energy, or the area under the load displacement curve, versus initial notch depth is divided by the width of the specimens to provide  $J_c$  from:

$$J_c = - \left( \frac{1}{b} \right) \left( \frac{dU}{da} \right) \quad \text{eq 4.}$$

where  $U$  is the strain energy to failure,  $b$  is the sample width, and  $a$  is the notch depth.

The second method of calculating  $J_{Ic}$  was through the comparison and adaptation of the ASTM D6068 standard for determining J-R curves of plastic materials to the SCB test and the FFF material. Through the use of high speed and high-resolution cameras commonly used in digital image correlation (DIC), the crack advancement path and length were monitored in order to use the J-R curve method in the ASTM D6068 standard. In the test methodology from the ASTM D6068 standard, a specimen with an initial crack length  $a_0$  is loaded to introduce a crack propagation of length  $\Delta a$  with the resulting load displacement curve used to calculate the strain energy  $U$ . The associated  $J$  values are calculated according to

$$J = \frac{\eta U}{b(W-a_0)} \quad \text{eq 5.}$$

Where  $\eta$  is a geometric constant,  $b$  is sample width,  $W$  is sample height which is equal to  $R$  in the case of this adaptation. The geometric constant  $\eta$  used in this test was the same for the single edge notch bend specimen, value of 2, due to no current constant in the standard for the SCB specimen. This shape factor has been calculated for different specimens through the use of finite element analysis but was not explored in this study. The calculated values of  $J$  are plotted against the crack advancement  $\Delta a$  and fitting a power law in the form of

$$J^{fit}(\Delta a) = C_1 \Delta a^{C_2} \quad \text{eq 6.}$$

where  $C_1$  and  $C_2$  are the fitting parameters. On the same set of axes, an offset blunting line is plotted to account for the development of the plastic zone in front of the crack tip. This offset blunting line is created from

$$J^{blunt}(\Delta a) = 2\sigma_y(\Delta a - \epsilon) \quad \text{eq 7.}$$

where  $\sigma_y$  is the yield stress of the material and  $\varepsilon$  is the offset value. The offset value of 0.2 mm was applied based on the work done by Lu et. al.<sup>13</sup> The intersection of the blunting line with the J-R curve is the critical elastic-plastic strain energy release rate,  $J_{Ic}$ .

## Results

### ***Mode I Intrabeed Fracture***

The initial orientation tested was to test for intrabeed fracture, **Figure 62**. Due to cutting location, the notch ended at various points within the printed beads. The effects of where the notch ended in the bead was slightly tied to the overall behavior of the specimens under load in this configuration, **Figure 62**. In particular, sample 7, 10, 11, 14 and 15 demonstrate the notch ending at either the topmost or bottom-most section of the bead. In the associated area adjusted stress versus displacement curve, these specimens demonstrated a higher modulus and higher failure load than in the specimens with the notch ending in the middle of a bead. Despite sample 6-10 having a higher printing temperature than specimens 11-15, the overarching behavior of the specimens remained fairly similar.



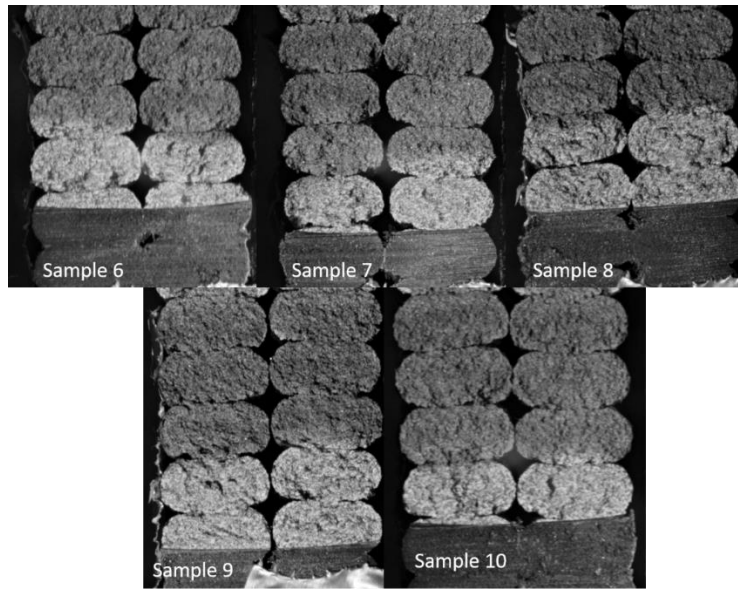


**Figure 63** Fracture surface of the SCB 33.02mm radius specimens printed at 230C.

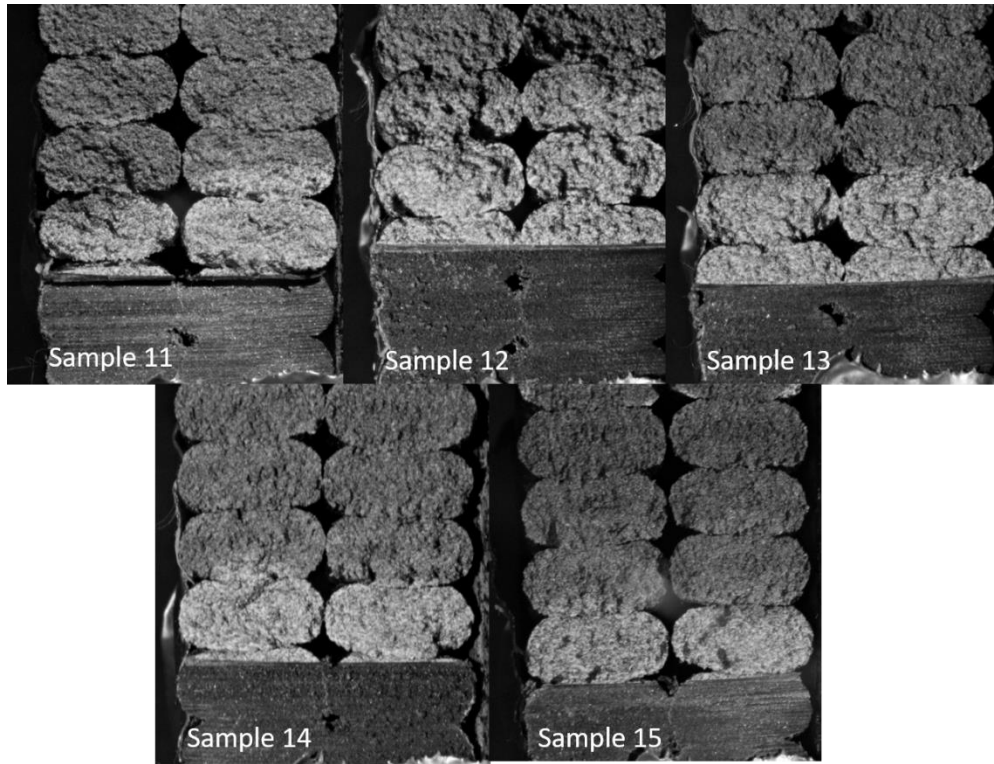


**Figure 64** Fracture surface of the SCB 33.02mm radius specimens printed at 220C. Due to cutting location, the notch ended at various points within the printed beads

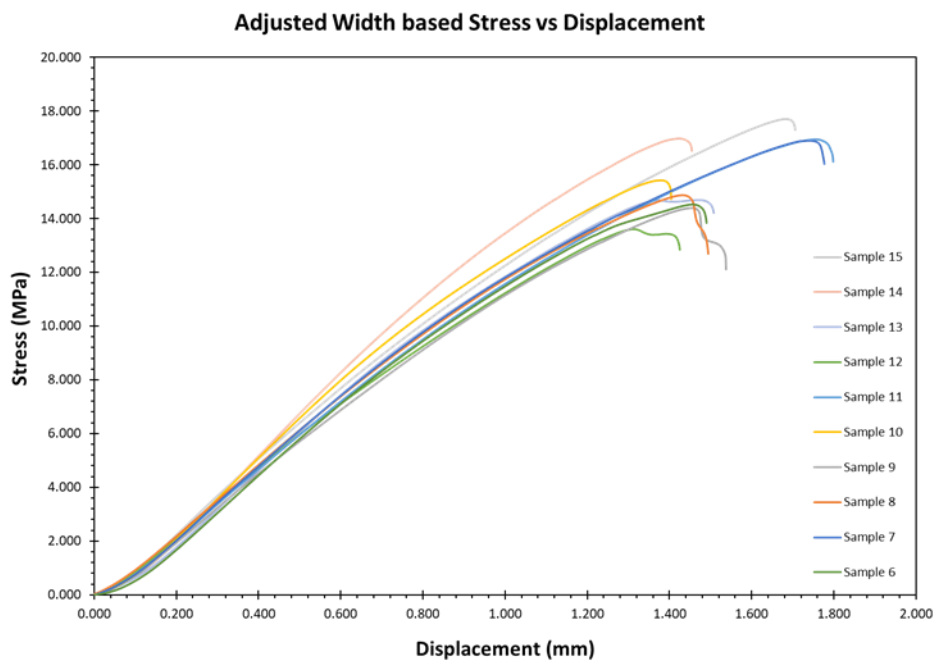
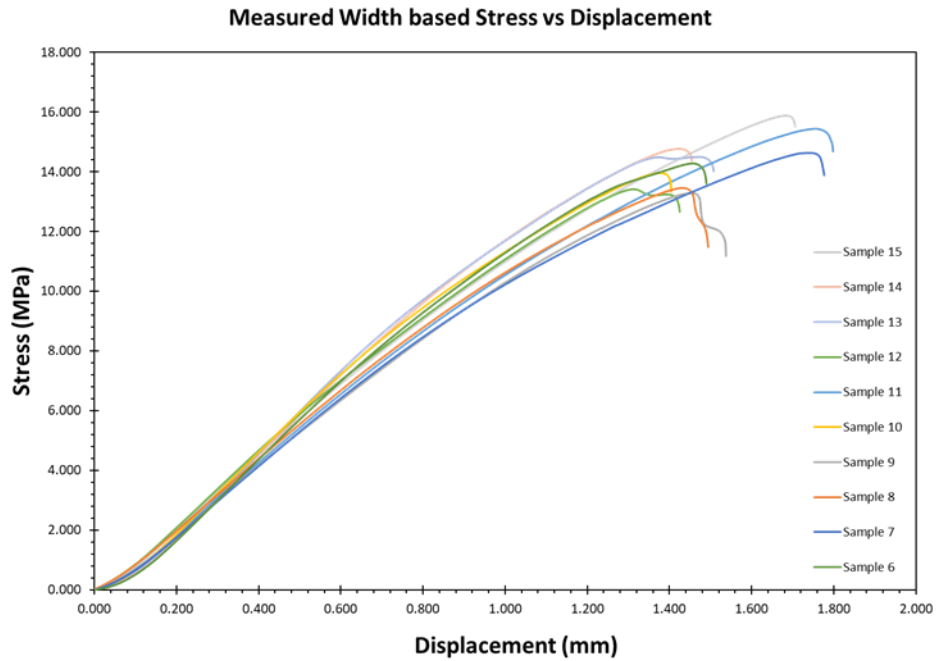


**Figure 65** Noticeable effects and variations occur when adjusting the width of the specimen based on the cross section of the figures above

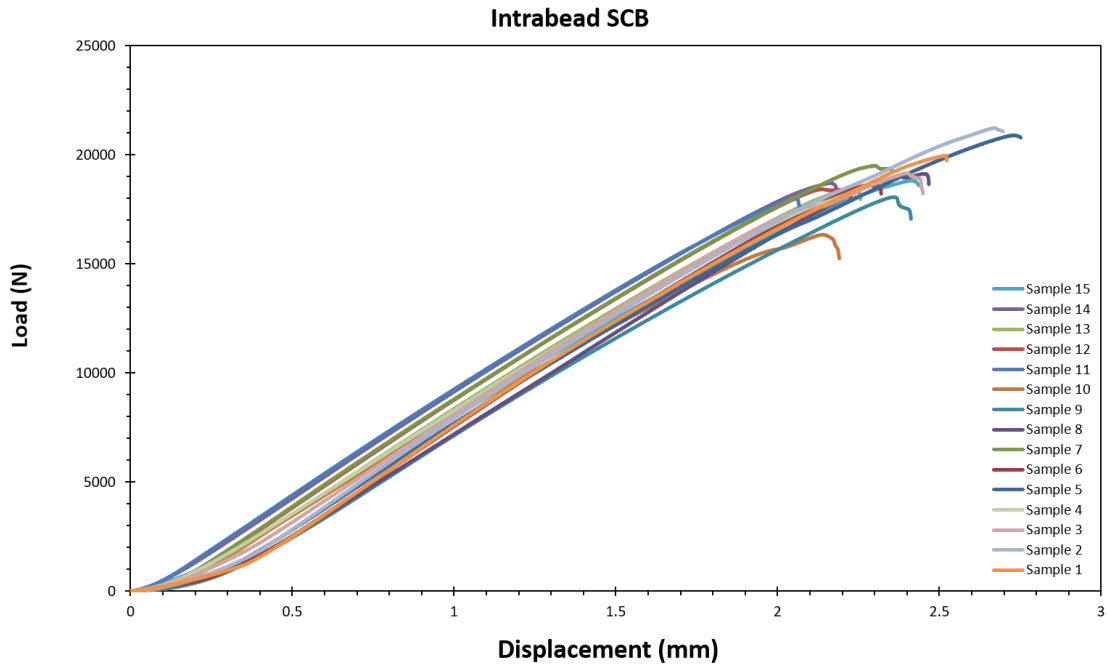


**Figure 66** load versus displacement for mode I fracture toughness intrabeard

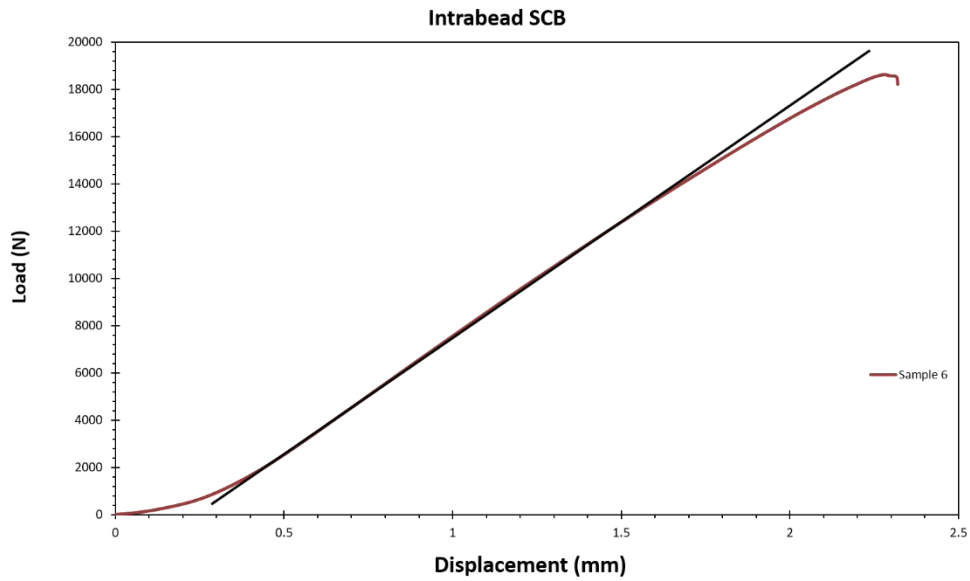


**Figure 67** Deviation from linearity example with straight line applied to load versus displacement curve

### SCB Specimens from 1.5m Plaque

In the larger plaque specimens for intrabead failure, the preliminary testing shows fairly little plasticity and very consistent failure, **Figure 66**. In these tests, the specimen width is 38.1mm and the thickness is 76.2mm. There was a significant decrease in the plasticity of the part and a reduction in the visual deformation near the rollers under loading. The load displacement behavior and sudden failure demonstrate brittle behavior with a small region of stable crack growth. The small deviation from linearity generally marked the region where the crack begins to form. To observe the deviation from linearity, a straight line was plotted over the data following the slope of the load versus displacement curves, **Figure 67**.

From the equations 1 and 2, the normalized SIF and then subsequently  $K_{Ic}$  and  $G_{Ic}$  were calculated. **Table 18** and **Table 19** outline the slight variation in the initial crack length and then the critical crack length and both of these values were used in the calculation of the  $G_{Ic}$ . This comparison provided a slight increase in the calculated  $G_{Ic}$  which is to be expected with a slightly longer crack length at failure.

**Table 18** Specimen geometry values and fracture toughness calculated, with standard deviation (STD), using the initial crack length a

|                                     | calculated using a |          |             |          |             |          |
|-------------------------------------|--------------------|----------|-------------|----------|-------------|----------|
|                                     | 6 min layer        | STD      | 4 min layer | STD      | 2 min layer | STD      |
| a (m)                               | 0.030              | 4.07E-04 | 0.030       | 1.66E-03 | 0.030       | 1.03E-03 |
| R (m)                               | 0.076              | 1.28E-04 | 0.076       | 2.15E-04 | 0.076       | 8.93E-05 |
| B (m)                               | 0.037              | 1.93E-04 | 0.037       | 2.40E-04 | 0.038       | 1.73E-04 |
| Y1                                  | 5.099              | 4.40E-02 | 5.130       | 1.78E-01 | 5.143       | 1.08E-01 |
| $\beta$                             | 0.394              | 6.00E-03 | 0.395       | 2.27E-02 | 0.399       | 1.39E-02 |
| P (N)                               | 20366              | 729      | 18323       | 1106     | 18465       | 289      |
| $K_{Ic}$<br>(Mpa*m <sup>1/2</sup> ) | 5.58               | 0.176    | 5.09        | 0.117    | 5.09        | 0.137    |
| $G_{Ic}$ (J/m <sup>2</sup> )        | 2292               | 145      | 1905        | 89       | 1903        | 102      |

**Table 19** Specimen geometry values and fracture toughness calculated, with standard deviation (STD), using the critical crack length  $a_c$ .

|                                     | calculated using $a_c$ |          |       |          |       |          |
|-------------------------------------|------------------------|----------|-------|----------|-------|----------|
|                                     | 6 min layer            | STD      | 4 min | STD      | 2 min | STD      |
| a (m)                               | 0.038                  | 1.38E-03 | 0.040 | 2.66E-03 | 0.040 | 1.18E-03 |
| R (m)                               | 0.076                  | 1.28E-04 | 0.076 | 2.15E-04 | 0.076 | 8.93E-05 |
| B (m)                               | 0.037                  | 1.93E-04 | 0.037 | 2.40E-04 | 0.038 | 1.73E-04 |
| Y1                                  | 5.099                  | 4.40E-02 | 5.130 | 1.78E-01 | 5.143 | 1.08E-01 |
| $\beta$                             | 0.394                  | 6.00E-03 | 0.395 | 2.27E-02 | 0.399 | 1.39E-02 |
| P (N)                               | 20366                  | 729      | 18323 | 1106     | 18465 | 289      |
| $K_{Ic}$<br>(Mpa*m <sup>1/2</sup> ) | 6.27                   | 0.169    | 5.90  | 0.138    | 5.82  | 0.143    |
| $G_{Ic}$ (J/m <sup>2</sup> )        | 2895                   | 156      | 2556  | 120      | 2492  | 122      |

From the initial analysis of the slight deviation from linearity, a comparison and testing of the J-integral method as compared to the  $G_{Ic}$  calculation and evaluation was performed. In order to calculate the J-integral method, several different methods were used in order to explore the applicability to this materials system. The initial analysis of the J-integral to determine  $J_{Ic}$  was to compare the load carrying capacity of the system at two different initial notch lengths. The comparison of the 0.3\*R and 0.4R, shown in **Figure 68**, greatly overestimated the  $J_{Ic}$  providing a value of 38.7 kJ/m<sup>2</sup> which was over ten times the values from the  $G_{Ic}$ . In perfectly linear elastic isotropic brittle materials, the  $J_{Ic}$  reduces to the  $G_{Ic}$ . Based on the load displacement, it is highly unlikely that the toughness is this different with the apparent semi-brittle nature. The specified use of maximum load, for the integration point for total strain energy, as compared to the load where the crack begins to propagate is a major source of error when comparing this with other methods.

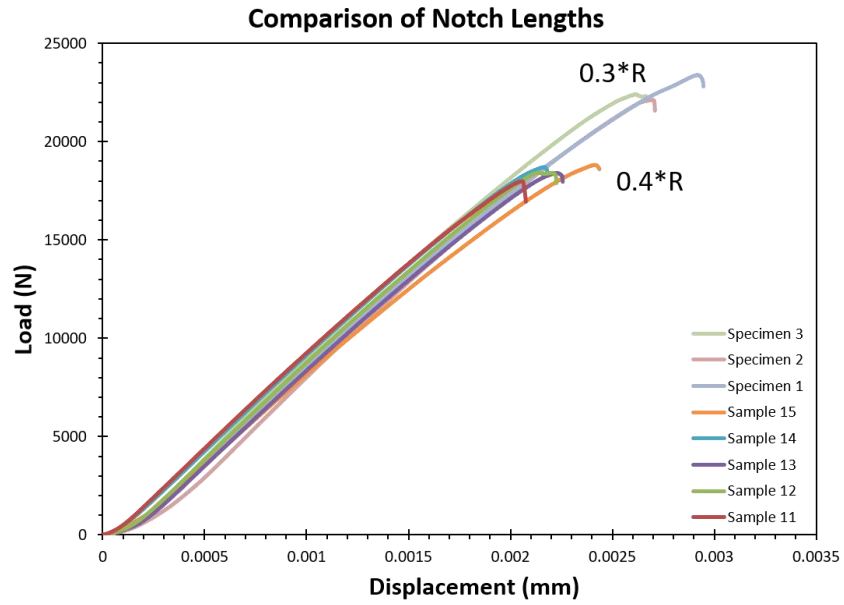


**Figure 68** comparison of the load carrying capacities of the 0.3\*R and 0.4\*R notch lengths.

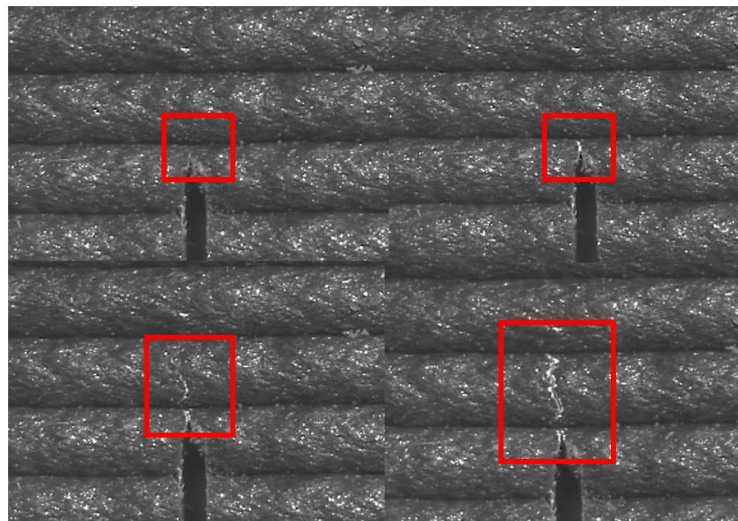


**Figure 69** DIC images of crack growth during specimen loading. From top left to bottom right, the crack growth can be seen in the red boxes.

Based on this, the creation of J-R curves, or the J versus resistance, as the crack propagates was created in order to better evaluate the  $J_{Ic}$ . Based on the shape and size of the SCB specimen, using sets of specimens and loading to certain displacements for crack growth created several challenges. To alleviate this, digital image correlation was used to track crack growth so a J-R curve could be created for a single specimen as it underwent load to failure, **Figure 69**. An example of the created J-R curve, provided in **Figure 70**, demonstrates the sensitivity of the method on the measurement of crack advancement throughout the test. Because of the DIC limitations, having only surface imaging of the crack, there is inherent error in these curve fits and subsequently the calculation of  $J_{Ic}$ . The benefit of this method though is the ability to measure the  $J_{Ic}$  for each specimen rather than relying on multiple different specimens being loaded to different points in order to obtain the  $J_{Ic}$ . In the evolution of the fracture testing for FFF, the ability to measure specimen to specimen variability becomes increasingly important for qualification purposes. Single test geometries and tests allow for better understanding of printing parameter effects on the tested fracture toughness values.



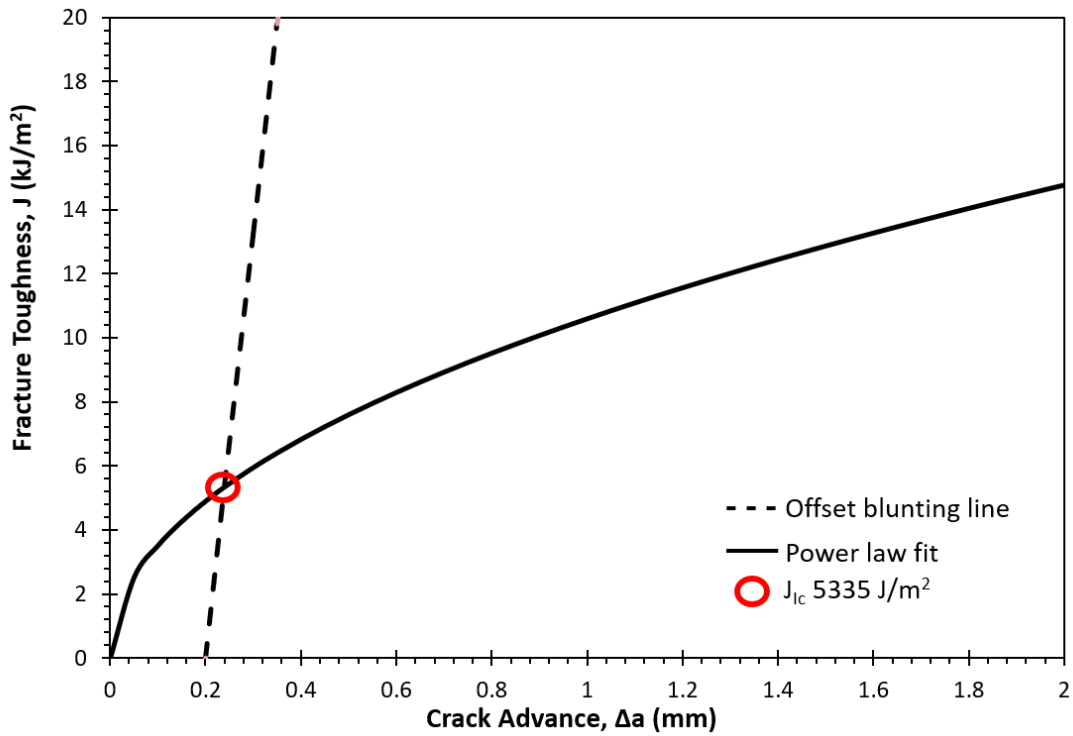
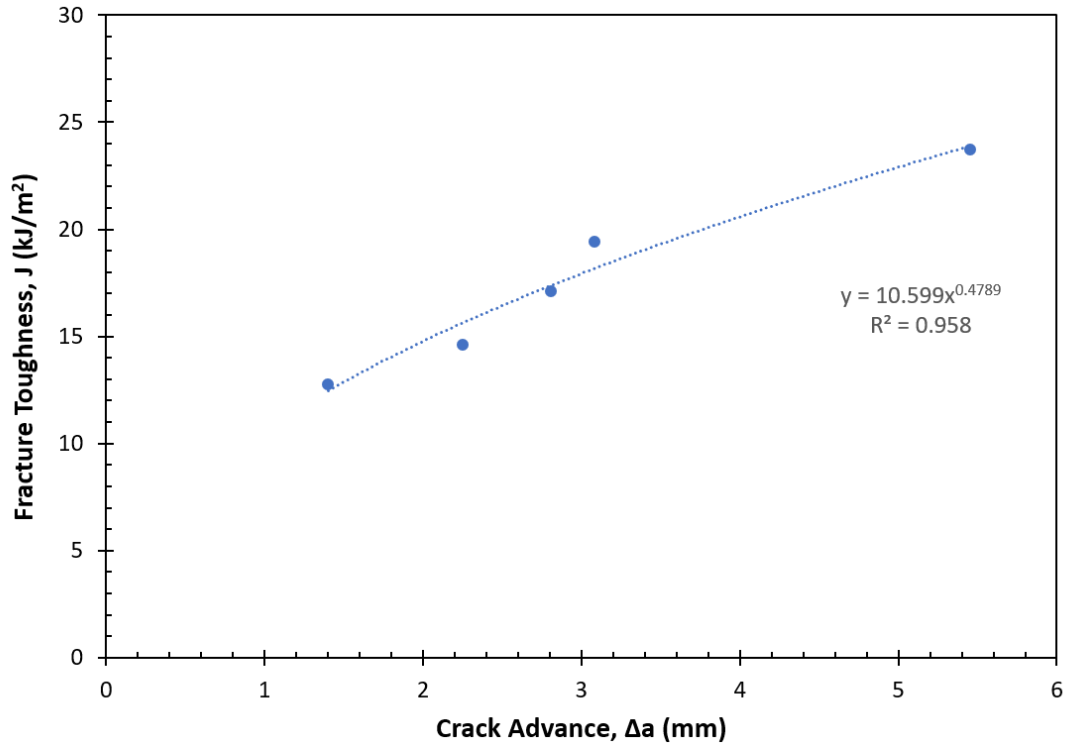


**Figure 70** J-R curve for intrabead SCB specimen 14, as an example.

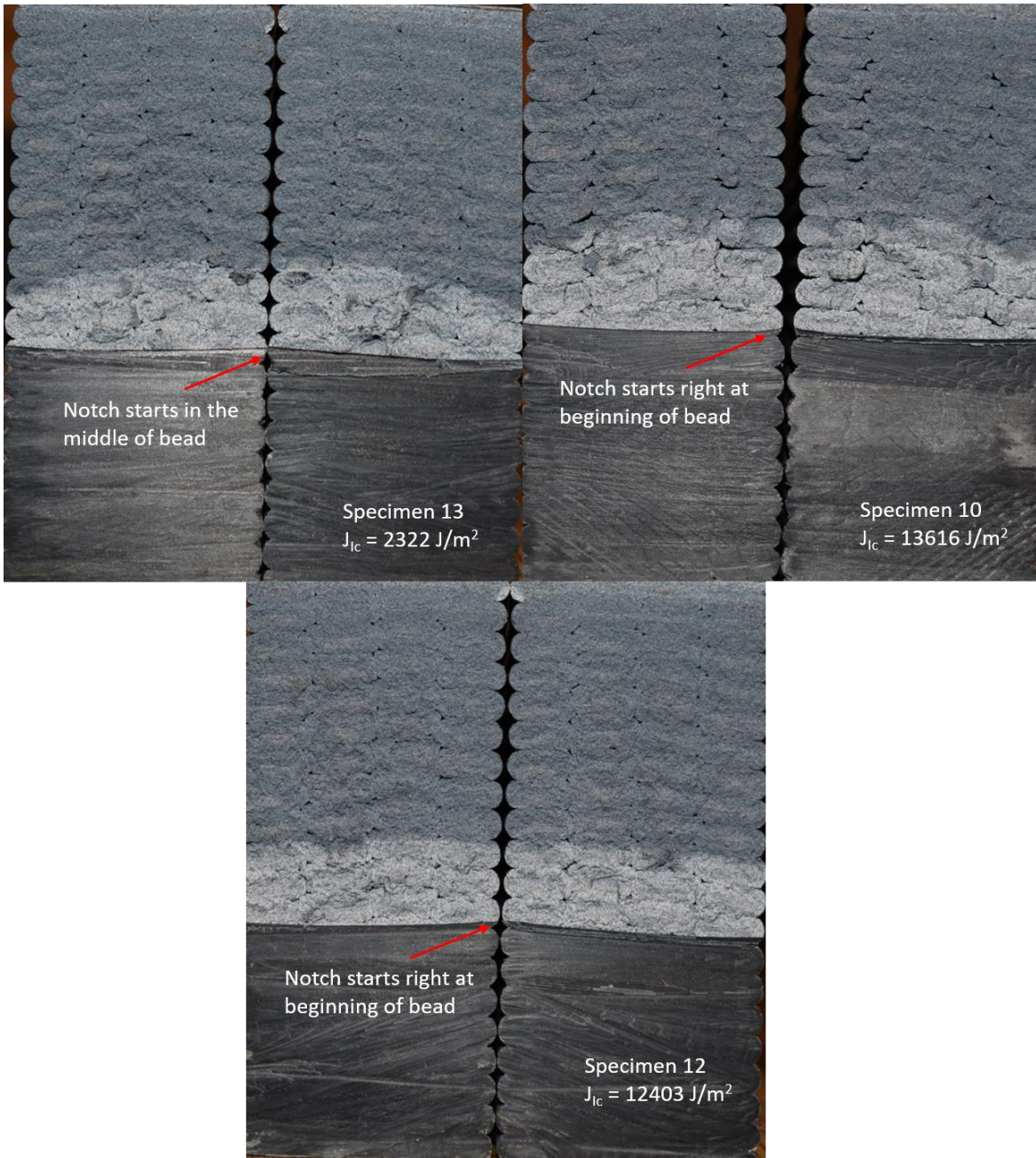


**Figure 71** Fracture toughness dependence on initial notch location

Due to the heavy reliance of the  $J_{Ic}$  on the crack advance measurements the individual calculation of the  $J_{Ic}$  of each specimen is shown on the fracture surface of several notable specimens. The fracture surfaces of the SCB specimens also show some reliance of the crack on the bead locations and the shape of the initial notch, **Figure 71**.

For the interlayer specimen tested, the load displacement curve is seen in **Figure 72**. Based on the calculated fracture toughness through the bead, the maximum load should be predicted if the nature of the specimen is homogeneous with systematic voids. However, if the interlayer properties are significantly different than in the intrabead properties then the laminate nature of the material can be confirmed with reasonable certainty. The overall behavior of the material is slightly more linear in nature but still shows a little bit of yielding before failure.

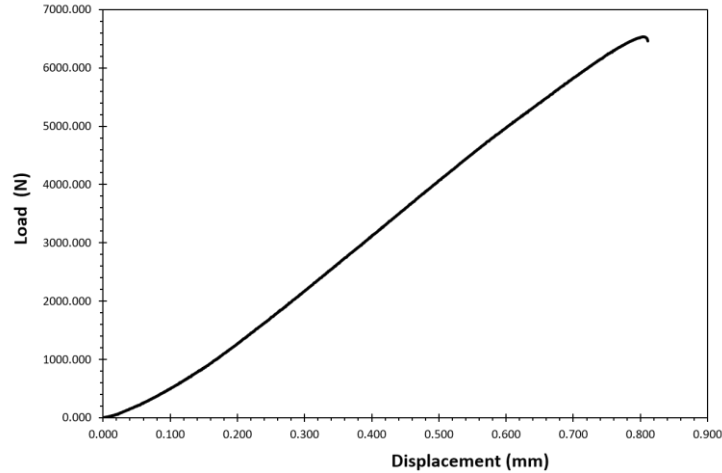


**Figure 72** Interlayer SCB specimen load displacement plot showing very minimal deviation from linearity.

## Discussion

### *Comparison of G and J*

In this particular testing method, the overall behavior was surprisingly linear despite being a plastic material. However, in the comparison of G and J there existed differences that lead to the conclusion that for precise analysis and predictive modeling, the J integral approach should be performed and done with caution. The overall average intrabead  $J_{Ic}$  of the CF-ABS BAAM specimens was calculated to be  $7564 \text{ J/m}^2$  which is within reason for the fiber reinforced ABS material where the pure ABS material demonstrated a  $J_{Ic}$  of  $3500\text{-}5500 \text{ J/m}^2$ . This is compared to the average  $G_{Ic}$  of  $2648 \text{ J/m}^2$  which is similar to the calculated toughness of hot press molded SENB tests of 15 wt% CF reinforced ABS, which was  $3090 \text{ J/m}^2$ . For the intrabead fracture toughness tests, the crack generally began to propagate at around 12kN to 14kN and the specimen sustained loads to on average 18kN-20kN. This is a large amount of non-linear load that could be accounted for in the material testing. With that in mind though, the current test set up explored in this work could not fully guarantee the load at which the crack began to propagate due to only characterizing surface crack growth. The full adherence of specimen testing to ASTM D6086 would be needed in order to more adequately qualify a material based on mode I fracture toughness through a deposited bead.

However, this test showed a self-contained and highly repeatable set up to determine the  $G_{Ic}$  with relative ease and accuracy that could be used for multiple orientations and expanded to mixed mode and pure mode II fracture. The cracks generally grew between 5-8mm, or roughly 10.9% to 17% of the ligament length, before sudden failure. This fairly brittle behavior demonstrates that it is not entirely unreasonable to categorize the fracture toughness by  $G_{Ic}$ .

### ***Layer Time effect on fracture***

The relative ease of measuring the  $G_{Ic}$  and the repeatable nature allowed for the comparison of three different layer times, 2 min, 4 min, and 6 min, with relatively low error. From these tests, **Table 18** and **Table 19**, the  $G_{Ic}$  shows slightly higher values for the 6 min layer time, roughly 16% higher. This behavior could be because of the slightly more pronounced raster voids in the material. These voids, while not appearing to cause significant impact on the intrabead failure, could be concentrating and arresting the stresses in front of the crack tip. As the pressures in front of the crack tip go from a large area to a smaller area, following the ellipse of the bead, and then back to a larger area, more load capacity could be held after the initial crack initiation. This is seen in specimens where the notch started at the beginning or end of a bead.

### ***Interlayer Fracture Toughness***

The interlayer  $G_{Ic}$  value using the layer to layer Z-axis modulus of 2.13 GPa, from the work by Duty et. al.,<sup>14</sup> was calculated to be 1515 J/m<sup>2</sup> with a Poisson's ratio of 0.35. However, for small scale evaluations of the CF-ABS material demonstrate a Poisson's ratio as low as 0.2 depending on orientation. Altering the calculation with this Poisson's ratio in mind produces a  $G_{Ic}$  value of 1657 J/m<sup>2</sup>, which while lower than the intrabead, is still very close to the calculated  $G_{Ic}$  of the intrabead properties. Both of these values are well within the range of the interlaminar fracture toughnesses explored by Nycz et. al. using a dual cantilever beam test to explore layer preheating. The values provided by Nycz et. al. show toughness values of 1560J/m<sup>2</sup> for layers roughly the temperature expected for plaques of this size.<sup>5</sup>

### ***Characterization of BAAM Parts***

The important conclusion from comparing the work by Nycz and the above testing, is that when adjusting for the known modulus differences along the deposited bead and across layers, the fracture toughness values are relatively

close. With the adjustment of processing conditions, the difference shrinks with the maximum interlaminar fracture toughness achieved as  $5410 \text{ J/m}^2$ .<sup>5</sup> Based on the fracture surfaces, **Figure 73**, and the results that show a shrinking of the difference in intrabead and interlayer  $G_{Ic}$ , the material could be categorized as a transversely isotropic material with distinct moduli and distinct material properties within the bead and at the interface. From **Figure 73**, the fracture surfaces demonstrate consistent crazing symptomatic of plastic deformation only in the middle of the beads, with a lack of this present at the interfaces of beads and layers. From this, there is a material difference within the beads and at the layers, however this could be a function of the processing conditions chosen for this particular set of tests. Further evaluation of more optimal printing conditions should be done in order to fully categorize the homogeneity of the parts.

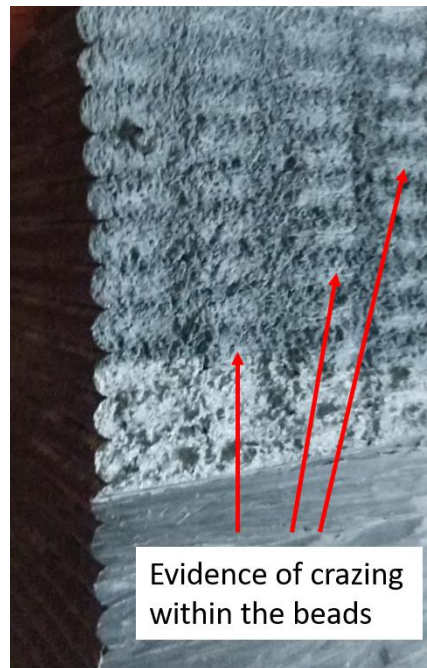


**Figure 73** Crazing within the beads but not at the interface demonstrates different material behavior and properties in the various locations

## **Conclusions**

The SCB test specimen has been shown to reasonably capture the  $G_{Ic}$  and  $J_{Ic}$  of both the interlayer and the intrabead properties of BAAM manufactured specimens. This self-consistent test provides the ability to obtain interlayer properties and intrabead properties with the same specimen geometries, reducing the variability of shape effects and manufacturing approaches that current methods introduce. The ease of manufacturing also allows for more specimens to be tested without the incredibly strict crack insertion requirements of current interlaminar fracture toughness tests. Expanding this test to be able to measure the mixed mode I/II and pure mode II requires only adjusting the crack angle and the span distance making this a really advantageous set up to systematically test the effect of processing conditions and deposition strategies on the fracture properties of the material. However, due to the size and shape of the specimens, the production of a J-R curve becomes slightly more difficult in order to achieve cryofracture to fully determine the location of the crack advancement per force applied. Ultimately the SCB specimen could provide a unified specimen to investigate the effects of multiple processing conditions and strategies to further define the processing-structure-performance relationships within BAAM manufactured plastics.

## **Acknowledgments**

Financial support was provided by the Naval Education Engineering Consortium, grant N00174-16-C0033, under the direction of Dr. Maureen Foley at the Naval Surface Warfare Center Carderock Division.

## References

1. Hart, K. R. & Wetzel, E. D. Fracture behavior of additively manufactured acrylonitrile butadiene styrene (ABS) materials. *Eng. Fract. Mech.* **177**, 1–13 (2017).
2. Spoerk, M. *et al.* Anisotropic properties of oriented short carbon fibre filled polypropylene parts fabricated by extrusion-based additive manufacturing. *Compos. Part A Appl. Sci. Manuf.* **113**, 95–104 (2018).
3. Young, D., Wetmore, N. & Czabaj, M. Interlayer fracture toughness of additively manufactured unreinforced and carbon-fiber-reinforced acrylonitrile butadiene styrene. *Addit. Manuf.* **22**, 508–515 (2018).
4. Aliheidari, N., Tripuraneni, R., Ameli, A. & Nadimpalli, S. Fracture resistance measurement of fused deposition modeling 3D printed polymers. *Polym. Test.* **60**, 94–101 (2017).
5. Nycz, A. *et al.* Controlling substrate temperature with infrared heating to improve mechanical properties of large-scale printed parts. *Addit. Manuf.* **33**, 101068 (2020).
6. Arbeiter, F., Spoerk, M., Wiener, J., Gosch, A. & Pinter, G. Fracture mechanical characterization and lifetime estimation of near-homogeneous components produced by fused filament fabrication. *Polym. Test.* **66**, 105–113 (2018).
7. McLouth, T. D., Severino, J. V., Adams, P. M., Patel, D. N. & Zaldivar, R. J. The impact of print orientation and raster pattern on fracture toughness in additively manufactured ABS. *Addit. Manuf.* **18**, 103–109 (2017).
8. Ayatollahi, M. R. & Aliha, M. R. M. Wide range data for crack tip parameters in two disc-type specimens under mixed mode loading. *Comput. Mater. Sci.* **38**, 660–670 (2007).
9. Nejati, M., Aminzadeh, A., Saar, M. O. & Driesner, T. Modified semi-circular bend test to determine the fracture toughness of anisotropic rocks. *Eng. Fract. Mech.* **213**, 153–171 (2019).
10. Ayatollahi, M. R. & Aliha, M. R. M. On determination of mode II fracture toughness



using semi-circular bend specimen. *Int. J. Solids Struct.* **43**, 5217–5227 (2006).

11. Ayatollahi, M. R., Aliha, M. R. M. & Hassani, M. M. Mixed mode brittle fracture in PMMA - An experimental study using SCB specimens. *Mater. Sci. Eng. A* **417**, 348–356 (2006).
12. Kuruppu, M. D. & Chong, K. P. Fracture toughness testing of brittle materials using semi-circular bend (SCB) specimen. *Eng. Fract. Mech.* **91**, 133–150 (2012).
13. Lu, M., Lee, C. & Chang, F. by J-Integral Methods. **35**, 1433–1439 (1995).
14. Duty, C. E. *et al.* Structure and mechanical behavior of Big Area Additive Manufacturing (BAAM) materials. *Rapid Prototyp. J.* **23**, 181–189 (2017).

## **CHAPTER V CONCLUDING REMARKS AND FUTURE WORK**

This dissertation presented the study of the mechanics of fused filament fabricated polymer structures with the goal of elucidating processing-structure-performance relationships. The ultimate goal of qualification of FFF materials is advanced through further evaluation of the current state of the art, the processing-structure-performance relationships in uniaxial tension testing, the effects of environmental conditioning on performance, and the novel use of a fracture test that allows more accurate comparison of processing conditions on the fracture toughness.

### **Chapter Reviews**

In Chapter 1, the current state of the art in evaluation of polymer physics at the molecular level is provided to demonstrate the immense problem of predicting polymer strength at the interface. It is not enough to measure the temperature and attempt to correlate that the strength of adhesion, where many other factors are necessary in evaluation of the polymer chain dynamics at those interfaces. Current work in fracture mechanics of polymer AM provides several testing methods but still suffers from the printer variability in comparison of the fracture toughness. Additionally, there is no consensus on the classification of the material as the very mesostructure depends highly on the printing conditions, teetering between laminate and homogeneous.

In Chapter 2, the evaluation of the ASTM D638 standard for tensile testing of polymer materials is evaluated and further classification and testing recommendations are made. Based on the three axis building patterns and the

unique combinations of possibilities, it is recommended that a more robust naming methodology should be adapted. Based on the material properties changing for the same visual part based on the orientations it was printed in, there is a large variability in the deposition pattern effect beyond just the bead orientations with respect to load. Additionally, the size and shape effects of the ASTM D638 type dog bone specimens were initially categorized where the same printing parameters were used but a large change in ultimate tensile strength was observed. Beyond the shape and size of the specimen, the printing parameters had an incredible effect on the ultimate tensile strength and stiffness of the material where overall polymer temperature plays a large role in strength and also the brittle to ductile nature of part failure. Higher printing and localized temperature created a more ductile test specimen as compared to lower temperatures, even reducing the ultimate tensile strength. This was due to a more favorable entropic configuration in the material that allowed for better polymer chain motion during load, increasing the elongation to break. And finally, the effects of scaling up printing to handle larger outputs creates uncertainty in part comparison to directly and singularly printed specimens. By printing specimens in plaques or printing numerous of the same print on the print surface at the same time created vastly different mechanical properties compared to those that were printed individually on the bed. Due to the heat transfer and layer times associated with printing plaques or multiple specimens on the bed, there becomes a different local area temperature that alters the polymer chain dynamics. This should be considered

when developing future standards for strength and stiffness evaluation in FFF polymer systems.

In chapter 3, the effect of heat and moisture on the ultimate tensile strength of both fiber reinforced and unreinforced ABS was evaluated. As the test specimens conditioning protocol approached  $T_g$ , the polymer chains became more mobile and dictated a significant change in elongation to break. Additionally, there was a reduction in the overall tensile strength of the material which is to be expected when temperatures exceed roughly 60% of  $T_g$ . In both the reinforced and unreinforced systems, the polymer matrix dictated the response to load where changes in the response were similar in both systems. In temperatures less than 50% of  $T_g$  there was no reduction in the ultimate tensile strength, providing an upper bound for operating use. Additional work studying creep behavior would be needed to further qualify the material for use at temperature. When specimens were subjected to moisture, an increase in variability was seen with a reduction in tensile strength, however no trapped water was found after subjecting the specimens to ambient conditions.

In Chapter 4, the SCB specimen was demonstrated to be a capable testing method for the evaluation of the fracture toughness of BAAM parts. Currently the testing methods used for the evaluation of fracture toughness of AM parts is highly variable, introducing uncertainty in the obtained values from test to test. The SCB specimen provides a singular specimen geometry capable of testing multiple different fracture modes and orientations of the material, limiting the geometric

impact on the obtained values. While this test method had downfalls in the initial use, the method provides a platform to compare the processing-structure-performance relationships in BAAM materials in a relatively easy to manufacture and repeatable test set up. Additionally, the initial testing results demonstrate a fairly similar fracture toughness between layers and through the bead when the modulus was accounted for. This provides evidence of a transversely isotropic material that possesses some material differences at the layer interfaces. These material differences are predicated on the processing conditions. The sliding scale from fully laminate to homogeneous with systematic voids appears to be processing parameters based, where fully optimized printing parameters could create a near-homogeneous part demonstrating orientation independent fracture toughness. The SCB specimen provides a framework for fracture evaluation to further define the orientation dependence and further classify the material for future qualification.

### **Statement of Impact**

Processing structure performance relationships within fused filament fabrication are still being explored due to the complicated polymer dynamics at the interface. The highly adaptable framework where so many options can be changed and altered provide the perfect playground for scientists to explore interactions and physics. However, with the current testing standards, determining what is really causing the effects is immensely difficult. Based on the work presented, utilizing the wildly controllable printing parameters to really explore polymer dynamics and

advanced computational modeling is in reach. Additionally, for a technology as disruptive as AM has been, advancement cannot be held back by our traditional approach to testing standards that plagued the composites world. Reaching for abstract connections from disparate material systems has proven a way to isolate the material processing effects with a single reductionist specimen approach. When studying rock fracture, nobody is there to watch these rocks form and take notes of the processing. In FFF, there is the ability to take a simple test specimen, take notes during the manufacturing, and then compare the results. In order to really insert these polymer FFF machines into the manufacturing landscape identification and control of the controllables must be established. This SCB specimen may not be the desired specimen to qualify the materials statistically and outright, however it does provide scientists and engineers a simple to manufacture design that is capable of exploring the processing parameters without introducing shape and printing changes. This marks a significant step forward towards the goal of qualification of these parts in order for them to be used across many industries to improve the agility and adaptability of on-demand part manufacturing.

## **Future Work**

For AM, specifically FFF, to leave the world of rapid prototyping and enter the manufacturing landscape as a desirable method to produce end-user parts, testing standards specific to polymer AM must be developed. Whether that is through the adaptation of current testing standards or the full-on creation of unique standards is still to be determined. However, due to the high variability of the

manufacturing process, future work needs to evaluate the most simple and repeatable testing set ups and specimens possible to fully compare and quantify this variability. Additionally, this would provide the backbone for an integrated computational materials engineering (ICME) approach to materials qualification where multiscale physics-based modeling could be used to predict the polymer chain dynamics at the interface and then adequately capture that materials response to load. In materials science the push for tying processing-structure-performance relationships together is ever increasing and in the FFF landscape, advanced computational models will provide the foundation for uncertainty quantification in the future. Additionally, future work should be done in optimizing the printing conditions for during print changes based on temperature and the rheological properties to reduce the trapped strains in the materials. By keeping the material shear rates within the linear viscoelastic region, more long-range diffusion of the polymer chains could be achieved. The future of FFF includes embedded sensors, mid-print changes and optimizations, and expanded material systems, however the first major hurdle for FFF is the reduction of testing protocols to fully provide the material properties and not just the properties of the engineered part.

## APPENDIX

### List of Publications

1. **W. H. Ferrell**, S. TerMaath, *Fracture behavior of fused filament fabricated polymers: a review*, Additive Manufacturing, (submitted 2020)
2. **W. H. Ferrell**, C. M. Arndt, S. TerMaath, *Tensile strength dependence of FFF fiber reinforced ABS on environmental conditioning*, Mechanics of Advanced Materials and Structures, vol 0, issue 0, pg 1-14 (Feb. 2020)
3. **W. H. Ferrell**, J. Clement, S. TerMaath, *Uniaxial tensile testing standardization for the qualification of fiber reinforced plastics for fused filament fabrication*, Mechanics of Advanced Materials and Structures, vol 0, issue 0, pg 1-20 (Sept. 2019)
4. **W. H. Ferrell**, D. Kushner, M. Hickner, *Investigation of polymer–solvent interactions in poly (styrene sulfonate) thin films*, Journal of Polymer Science Part B: Polymer Physics, vol. 55, issue 18, pg 1365-1372 (Sept. 2017)



## VITA

William Howard Ferrell IV was born in 1994 in Jacksonville, NC to William H. Ferrell III and Esther L. Ferrell. He was raised around the world, calling several states and countries home along the way, with his sister Nikki. He graduated from The Pennsylvania State University in 2016 with a B.S. in Materials Science and Engineering and minors in Engineering Leadership Development and Polymer Science. During his undergraduate studies, Will worked with Dr. Michael Hickner and Dr. Douglas Kushner on ultra-thin film polymer swelling investigations through spectroscopic ellipsometry. Will pursued his Ph.D. in Materials Science and Engineering at The University of Tennessee, mentored by Dr. Stephanie TerMaath. During this time, he acquired his M.S. in Materials Science and Engineering with the Interdisciplinary Graduate Minor in Computational Sciences. Will graduated from the University of Tennessee with his Ph.D. in August of 2020. Will's research interests during his graduate studies focused on polymer and composite material structural mechanics and manufacturing.